Preparation and Characterization of Hierarchical Patterned Adhesives

Dissertation

zur Erlangung des Grades

des Doktors der Naturwissenschaften

der Naturwissenschaftlich-Technischen Fakultät III

Chemie, Pharmazie, Bio- und Werkstoffwissenschaften

der Universität des Saarlandes

von

Christina T. Bauer

Angefertigt am INM – Leibniz-Institut für Neue Materialien

Programmbereich Funktionelle Mikrostrukturen

Saarbrücken

2015

Tag des Kolloquiums: 15.01.2016

Dekan:	Prof. Dr. Dirk Bähre
Berichterstatter:	Prof. Dr. Eduard Arzt
	Prof. Dr. Frank Mücklich
Vorsitz:	Prof. Dr. Wulff Possart
Akad. Mitarbeiter:	Dr. Frank Aubertin

Contents

Danksagung

Zuallererst möchte ich mich bei Prof. Dr. Eduard Arzt, meinem wissenschaftlichen Betreuer, indessen Arbeitsgruppe ich meine Arbeit anfertigen durfte, recht herzlich bedanken. Es hat mir viel Freude bereitet ein Teil ihrer 'Forschertruppe' zu sein. Vielen Dank für ihren Einsatz und ihr Interesse am Gelingen meiner Arbeit und dem sehr fairen und respektvollen Umgang miteinander.

Prof. Dr. Frank Mücklich gilt mein Dank für die freundliche Übernahme des Zweitberichterstatters.

Prof. Dr. Wulff Possart danke ich für die Betreuuung im Rahmen des wissenschaftlichen Begleiters.

Auch eine sehr wichtige Person während meiner Arbeit war Dr. Elmar Kroner. Er hat in zahlreichen Diskussionen meine Arbeit vorangebracht und gab mir immer neue Motivation und Impulse zum Weiterforschen. Vielen Dank!

Dr. Tobias Kraus will ich für das 'Anlandholen' des Projektes SPP 1420 von der Deutschen Forschungsgemeinschaft danken. Er gab mir durch die erfolgreiche Antragstellung zusammen mit Prof. Dr. Eduard Arzt die Möglichkeit in einem solch spannenden Themenbereich zu promovieren und sicherte mir damit auch meine Finanzierungsgrundlage. In Projekttreffen diskutierten wir meine Ergebnisse und er gab wichtige wissenschaftliche Impulse für meine Arbeit.

Dr. Daniel Brodoceanu möchte ich sehr für die Zusammenarbeit innerhalb des Projektes SPP 1420 danken. Er diskutierte gerne mit mir über meine Arbeit und war stets zur Stelle wenn ich Hilfe benötigte.

Danken möchte ich auch Herrn Prof. Dr. Norman Fleck, der durch seinen großen Erfahrungsschatz neue Aspekte für meine Arbeit lieferte und durch die theoretischen Berechnungen stets neue Anregungen gab.

Dr. Nathalie Guimard und Dr. René Hensel danke ich für die nützlichen Vorschläge und Anregungen zu meiner Arbeit.

Joachim Blau danke ich für die technische Unterstützung am Adhäsionsmessgerät.

Dr. Philip Born möchte ich für die Diskussionen über das Partikelätzen danken.

Anne Wonn möchte ich für die gute Zusammenarbeit danken und für die Unterstützung als wissenschaftliche Hilfskraft.

Bedanken möchte ich mich auch bei allen Zimmerkollegen, die Abwechslung in den Forschungsalltag brachten. Hierbei möchte ich besonders Anika Kleemann, aber auch Viktoriia Barreau erwähnen, die manche Pause lustig gestalteten.

Der Metallwerkstatt des INM möchte ich für die tolle Zusammenarbeit danken.

Für inspirierende Diskussionen möchte ich mich bei all den Kollegen bedanken, die in gewissem Maße zu meiner Arbeit beigetragen haben.

Und ein großes Dankeschön geht an meine Eltern, meinen Mann und Sohnemann, die mich bei dem ‘Abenteuer Promotion’ stets unterstützt haben!

Abbreviations and symbols

AFM	Atomic Force Microscope
AR	Aspect Ratio
CAPA	Convective Assisted Particle Assembly
DFG	Deutsche Forschungsgemeinschaft
DMT	Derjaguin-Muller-Toporov
JKR	Johnson-Kendall-Roberts
MAD	Macroscopic Adhesion Measurement Device
PAA	Porous Anodic Alumina
PDMS	Polydimethylsiloxane
RF	Radio Frequency
RIE	Reactive Ion Etching
PMMA	Polymethylmethacrylate
RSm	Average Groove Spacing
RSS	Residual Sum of Square
RMS	Root Mean Square
SEM	Scanning Electron Microscopy
SPP	Schwerpunktprogramm (priority program)
PS	Polystyrene

B	bridges
H	hexagonal order
HB	hexagonal order and bridges

HL1	one hierarchical level
HL2	two hierarchical levels
HL3	three hierarchical levels
XX	neither hexagonal order nor bridges

ds	drop-like structure
gs	golfball structure
hp	hexagonal pillar array
hs	hole structure
ls	layer-like structure
m	mushroom
ms	mushroom shaped structure
ps	particle-like structure
sp	single pillar
ts	tunnel structure

A	cross-sectional area (m^2)
A_0	initial cross-sectional area (m^2)
a	contact radius (m)
α	angle (°)
$\alpha(t)$	time-dependent linear increasing angle (°)
B	thickness of backing layer (m)
β	radius of curvature of asperity (m)
$1/\Delta c$	adhesion parameter (–)
reduced χ^2	quality of a fit (–)
D	diameter (m)
ΔV	volume change (m^3)
D_0	initial particle diameter (m)
D_{crit}	critical particle diameter at which order is lost (m)
$D(t)$	time dependent particle diameter (m)
d	distance (m)

δ	deformation (m)
δ_b	bending deformation (m)
δ_c	compressive deformation (m)
$\delta_\perp$	net displacement (m)
df	standard deviation (m)
E	Young's modulus (Nm^{-2})
E^*	reduced Young's modulus (Nm^{-2})
ϵ	tensile strain (–)
F	force (N)
F_C	pull-off force (N)
F_{cap}	capillary force (N)
F_L	Laplace force (N)
F_{max}	maximum pull-off force (N)
F_n	normal force (N)
F_S	surface tension force (N)
φ	filling angle (°)
Γ	surface tension (Nm^{-1})
γ	work of adhesion (Nm^{-1})
γ_{12}	interfacial energy (Nm^{-1})
H^*	Hamaker constant (Nm)
H	height (m)
h	height of substrate (m)
h^*	Planck's constant (Nms)
η	polarizability ($\mathrm{Å}^2\mathrm{s}^4\mathrm{kg}^{-1}$)
I	area moment of inertia (m^4)
K	reduced stiffness (Nm^{-1})
k	stiffness (Nm^{-1})
k_B	Boltzmann's constant (NmK^{-1})
k_1	etch rate of the linear model (ms^{-1})
k_2	etch rate of the spherical cap model (ms^{-1})
k_3	etch rate of the constant volume-loss model ($\mathrm{m}^3\mathrm{s}^{-1}$)

$\|k\|$	absolute value of the etch rate, dependent on the model (ms^{-1}) or (m^3s^{-1})
κ	mean curvature of meniscus (°)
L	length (m)
$l(t)$	time-dependent diameter of the area of a spherical segment (m)
λ	wavelength (m)
M	bending moment (Nm)
m	pre-factor depending on clamping condition (–)
μ_d	dipole moment (Cm)
μ_T	Tabor parameter (–)
n	number of contacts (–)
ν	deflection (m)
P	preload (N)
P_B	buckling preload (N)
P_E	Euler buckling load (N)
p_a	ambient pressure (Nm^{-2})
p_0	saturated vapor pressure (Nm^{-2})
R	radius (m)
R_{gas}	ideal gas constant ($Jmol^{-1}K^{-1}$)
R_{rel}	relative radius (m)
r	distance (m)
ρ	tip radius (m)
S	center-to-center spacing (m)
σ	tensile stress (Nm^{-2})
T	temperature (K)
T_g	glass transition temperature (K)
t	etching time (s)
θ	contact angle (°)
Θ	average groove spacing of roughness (m)
U_{Debye}	Debye-interaction ($Å^2s^4kg^{-1}m^{-5}$)
U_{el}	elastic potential energy (Nm)
U_{Keesom}	Keesom-interaction ($C^4N^{-1}m^{-1}$)

U_{London}	London-dispersion ($Å^4s^9kg^{-2}N^2m^{-6}$)
U_{VdW}	Van der Waals potential (Nm)
υ	Poisson's ratio (–)
V	volume (m^3)
$\bar{V}$	molar volume (m^3mol^{-1})
W	width (m)
w	mass fraction (–)
y_i	experimental data (m)
$\hat{y}_i$	theoretical data (m)
ψ	root-mean-square roughness (m)
z_0	interatomic equilibrium distance (m)

Abstract

The remarkable adherence of geckos is attributed to the hierarchical structure on their feet pads. Although significant progress has been made, inspired by nature, in fabrication of dry adhesive materials on smooth surfaces, materials with similar adherence against rough surfaces are yet to be found. To better understand the effect of hierarchy on adherence we fabricated macroscopic models made of polydimethylsiloxane with different levels of hierarchy that were brought into contact with glass and with variously rough aluminum substrates. It was shown that adhesion decreases with higher micro- and macroroughness of the substrate. Further no benefits were found for the introduction of hierarchy levels. Another approach to fabricate biomimetic patterns was to exploit polystyrene (PS) µm-particles self-assembled into monolayers on a silicon surface. By treating them with oxygen plasma, nonclose-packed particle arrays with defined spacing were generated. The size and shape evolution of the PS particle layers during etching was analyzed and compared with different etch models. The etch mechanism is more complex than reported in the literature. The resulting patterns were used to fabricate silicon master templates that yield the finest hierarchical level via replica molding. Adhesion measurements were carried out to assess the performance of the softmoldings based on PS particle arrays. The results may help to design new adhesive structures.

Zusammenfassung

Die Adhäsionsfähigkeit von Geckos ist auf die hierarchische Struktur an ihren Zehen zurückzuführen. Hiervon inspiriert versuchen viele Wissenschaftler trockene Adhäsionssysteme herzustellen. Fortschritte auf glatten Oberflächen konnten bereits verzeichnet werden, jedoch fehlen Strukturen, die ähnlich stark auch auf rauen Oberflächen haften. Um die Funktion der Hierarchie besser zu verstehen, stellten wir ein makroskopisches Modell aus Polydimethylsiloxan (PDMS) mit unterschiedlichen Hierarchieebenen her, das mit Glas und verschieden rauen Aluminiumsubstraten in Kontakt gebracht wurde. Es wurde gezeigt, dass die Adäsion mit höherer Mikro- sowie Makrosubstratrauigkeit abfällt, sowie die Einführung von Hierarchieebenen keinen Nutzen bringt. Für die Herstellung von bioinspirierten Strukturen in kleinerem Maßstab wurden monodisperse Polystyrolpartikel als Monolagen auf Siliziumoberflächen mittels konvektiver Anordnung abgeschieden. Durch Plasmabehandlung wurden Partikelanordnungen mit definiertem Abstand hergestellt. Die Größen- und Formentwicklung der Partikel wurde in Abhängigkeit des Ätzprozesses untersucht. Der zugrundeliegende Ätzmechanismus ist komplexer als bislang angenommen. Die resultierenden Partikelanordnungen könnten dazu dienen, Gießformen für die feinste Hierarchieebene herzustellen. Des Weiteren wurden Partikelmonolagen mit PDMS abgeformt und die Adhäsionsfähigkeit des Replikats gemessen. Die Ergebnisse könnten dazu beitragen adhäsive Strukturen zu verbessern.

1 Introduction

To survive in nature, all organisms of the world have to develop a special strategy to live in their habitat. One of the tools for survival is the physiology of the respective species which has developed during the evolutionary adaption process. Mussels, which live in the rough sea, developed mechanisms to attach irreversible to the rocks, so they cannot be removed by the harsh environment. Tree and torrent frogs, which live in wet or even flooded environment, have a complex hierarchical structure on their toe pads which resembles little suction heads. In combination with a secretion which prevent them also from drying, they are able to adhere on different surfaces without falling. Another class of adhesion systems is 'dry' adhesion.

Animals such as some species of insects, spiders and lizards can adhere without any liquids on nearly every kind of surface. Some of them have developed hierarchical flexible hairy systems, which are able to adapt to rough surfaces. Modern microscopy techniques such as Scanning Electron Microscopy (SEM) or Atomic Force Microscopy (AFM) have enabled the investigation of small features of different adhesion systems and to solve the mystery of the adhesion structures. The understanding of natural structures, the following abstraction and finally the translation into a new structure is getting a very wide topic so it takes little wonder that there exist many words for that (biomimicry, biomimetics, bio-inspiration, biognosis or bionical creativity engineering).

Over the last years, one animal species has received special attention: the gecko. It is the largest known animal that can climb on a vertical rough substrate by means of a very fine hairy adhesion structure. Many theories were developed and concepts like 'contact splitting' were proposed [1]. But there are also many questions and parameters, which are insufficiently understood for example, the effect of roughness on adhesion. It is surprising that the hierarchical structures of geckos are imitated by some scientists without knowledge

of fundamental physics behind this kind of hierarchical system. To bridge this gap and to better understand the role of hierarchy in adhesion, a macroscopic model is a first start. In this thesis, we will investigate how a hierarchical hairy adhesive behaves against flat and rough substrates and which parameters influence the performance. The advantage of a macroscopic model is that the behavior of the system can be easily observed and the interaction between the hierarchical model and the substrate can be better analyzed.

While a fundamental understanding of the deformation of hierarchical structures is crucial, such structures also require advanced fabrication methods, which cover orders of magnitude in resolution. While large structures may be achieved by mechanical milling and microstructures are accessible via e. g. photolithography, sub-micrometer structures are difficult to achieve. So we developed a new method based on a combination of particle assembly and etching to fabricate finer structured biomimetic materials. We deposit particles on a substrate to form a close-packed monolayer. Then the particles can serve as an etching mask or can also be directly molded with a polymer.

This thesis is organized as follows: In Chapter 2, the contact mechanics will be presented and a literature overview about hierarchical structures, adhesion, a spring model, fabrication of bioinspired adhesion systems and elastic buckling of pillars, colloidal lithography and particle based soft molding is given. Chapter 3 gives an overview about the instruments and methods used. In Chapter 4 buckling and adhesion mechanisms on wavy substrates of hierarchical macroscopic fibrillar adhesives are investigated and discussed. Chapter 5 presents investigations and discussion of size and shape evolution of polystyrene particle during etching and of particle based softmolding. Chapter 6 is a short summary of this thesis and gives an outlook.

Chapter 4 was accepted for publication: C. T. Bauer, E. Kroner, N. A. Fleck, and E. Arzt, Hierarchical macroscopic fibrillar adhesives: In-situ study of buckling and adhesion mechanisms on wavy substrates, *Bioinspiration Biomimetics*, 2015 [2]. Parts of Chapter 5 were published as a full paper: C. T. Bauer, A. Wonn, D. Brodoceanu, P. Born, E. Kroner, and T. Kraus, Size and shape evolution of PS particle layers during etching, *Bioinspired, Biomimetic and Nanomaterials*, 2:130-140, 2013 [3].

This thesis was funded by SPP 1420 of DFG and started officially in July 2011. It was running for four years. The SPP project has the title as on 'Biomimetic Materials Research: Functionality by Hierarchical Structuring of Materials'.

2 Theoretical background

In this chapter the principles of contact mechanics will be introduced, followed by an insight into hierarchical structures in nature, especially into the adhesive structure of a gecko. In further parts adhesion measurement techniques will be presented. Further, a spring model and the theory of elastic buckling of pillars will be explained. In a further section a review of bioinspired adhesion systems will be given. Moreover an insight into colloidal lithography and particle-based softmolding is given. At the end of this chapter, the state of the art will be discussed and the aim of the thesis will be clarified.

2.1 Contact mechanics

Contact mechanics is an important part in the field of mechanical engineering to design safe and energy-efficient technical systems. It is a part of classical mechanics and deals with surface and geometrical considerations. At the end of the 19th century Heinrich R. Hertz was the first to relate surface geometry to elastic deformation behavior of a material.

2.1.1 The Hertz theory

In 1881, Hertz studied two elastic spheres (with radii R_1 and R_2) in frictionless contact which are compressed by a preload P (see Figure 2.1). He described the stress distribution, the contact radius a and the penetration depth δ. His theory assumes that the contact radius a is small in comparison to the radii of the contacting spheres [4].

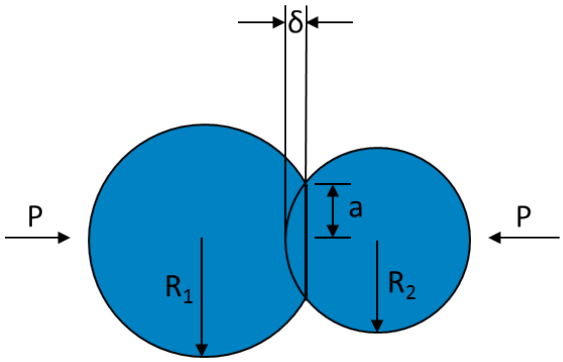

Figure 2.1: *Schematic of a contact experiment based on the Hertz theory.*

The resulting contact radius a can be predicted as:

$$a^3 = \frac{PR_{rel}}{K} \tag{2.1}$$

where R_{rel} describes the relative radius and K the reduced stiffness, which are defined as:

$$\frac{1}{R_{rel}} = \frac{1}{R_1} + \frac{1}{R_2} \tag{2.2}$$

$$\frac{1}{K} = \frac{3}{4}\left(\frac{1-{\upsilon_1}^2}{E_1} + \frac{1-{\upsilon_2}^2}{E_2}\right) = \frac{3}{4}\frac{1}{E^*} \tag{2.3}$$

with E_1, υ_1, E_2 and υ_2 being the Young's moduli and Poisson's ratios for sphere 1 and 2. E^* is called the reduced Young's modulus. Over the years the theory was extended for other substrate shapes like flat punches and cylinders [5]. Many theories were postulated, based on the Hertz theory, to describe more specialized contacts.

2.1.2 The Johnson-Kendall-Roberts theory

A limitation of the Hertzian theory is that attractive forces are neglected. Johnson, Kendall and Roberts published a paper on surface energy and contact of elastic solids in 1971 [6]. The theory is now called the Johnson-Kendall-Roberts theory, known as JKR. They closed the gap between the theoretical description and experimental observations on very soft materials [7, 8]. Attractive Van der Waals interactions inside the contact area are taken into account. The JKR theory balances elastic, potential and surface energy. The surface energy causes a larger contact area than in the Hertzian case, which is described by the contact radius a and under fixed load P conditions as:

$$a^3 = \frac{PR_{rel}}{K}\left[1 + \frac{3\pi\gamma R_{rel}}{P} + \sqrt{2\frac{3\pi\gamma R_{rel}}{P} + \left(\frac{3\pi\gamma R_{rel}}{P}\right)^2}\right] \tag{2.4}$$

where γ describes the work of adhesion which is defined as:

$$\gamma = \gamma_1 + \gamma_2 - \gamma_{12} \tag{2.5}$$

with γ_1 and γ_2 as the respective surface energies and γ_{12} as the interfacial energy for materials in contact. It can be concluded that the JKR term (see Equation 2.4) is a sum of Hertzian term and an additional term. For $\gamma = 0$, Equation 2.4 reduces to the Hertz theory (Equation 2.1). To separate the spheres, a force is needed, which is called pull-off force F_C and is given by:

$$F_C = -\frac{3}{2}\pi\gamma R_{rel} \tag{2.6}$$

The Johnson-Kendall-Roberts (JKR) theory is only valid for soft materials with high attractive forces.

2.1.3 The Derjaguin-Muller-Toporov theory

For hard materials and lower attractive interactions, a complementary theory is needed. In 1975 Derjaguin, Muller and Toporov treated the case of a contact between hard surfaces with low adhesion energy [9]. They assume only Van der Waals interactions outside the contact area and that the forces inside can be neglected because of the small contact area. The theory is called DMT theory and the assumptions resulted in the following relationship between contact radius a and pull-off force F_C:

$$a^3 = \frac{R_{rel}P}{K} + \frac{2\pi\gamma {R_{rel}}^2}{K} \tag{2.7}$$

$$F_C = -2\pi\gamma R_{rel} \tag{2.8}$$

It can be concluded that the contact area consists of a Hertzian term and a DMT addition. This expression is, apart from the pre-factor, identical to the JKR expression (see Equation 2.6).

2.1.4 JKR-DMT transition

In 1977, David Tabor defined a non-dimensional parameter to describe the continuous transition for materials with intermediate values of Young's modulus E and adhesion energies [10]. The Tabor parameter μ_T is defined as:

$$\mu_T = \left(\frac{R_{rel}\gamma^2}{{E^*}^2 {z_0}^3}\right)^{1/3} \tag{2.9}$$

where z_0 describes the interatomic equilibrium distance. The DMT theory is valid for $\mu_T < 0.1$ and the JKR theory for $\mu_T > 5$ [11]. In the intervall of 0.1 and 5 the transition between these

two theories occurs. In this work only soft surfaces were treated (Tabor parameter above 5) so that only the JKR theory will play a role. For example a sinusoidal aluminum substrate with $R_{Al} = 0.2\,\text{mm}$, $\nu_{Al} = 0.334$ and $E_{Al} = 70\,\text{GPa}$ and a flat silicon with $R_{PDMS} = \infty$ (flat), $\nu_{PDMS} = 0.5$ and $E_{PDMS} = 2.7\,\text{MPa}$ gives a Tabor parameter of $\mu_T = 353$, if $\gamma = 0.02\ \text{J/m}^2$ and $z_0 = 0.4\,\text{nm}$.

2.1.5 Comparison of Hertz, JKR and DMT theories

Figure 2.2 shows the difference between Hertz, JKR and DMT theories. The Hertz theory assumes that there act no attractive forces. The JKR theory considers only the effects of pressure and adhesion forces inside the contact area while the DMT theory shows Hertzian behavior, but also additional attractive forces outside the contact area.

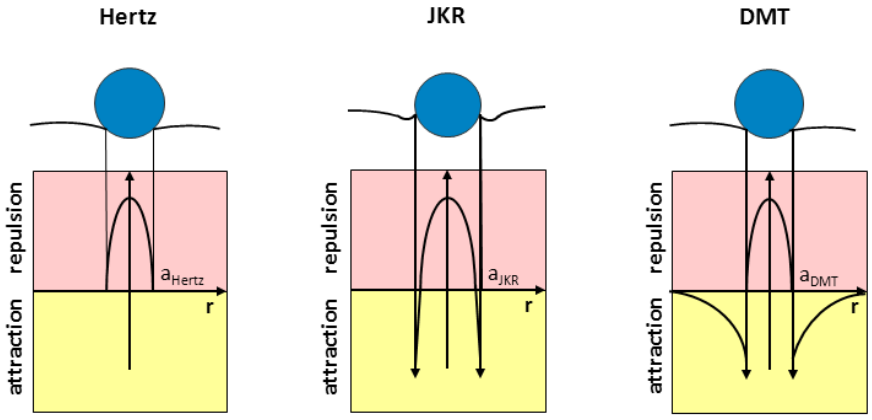

Figure 2.2: *Comparison between Hertz, JKR and DMT theories, adapted from [12].*

2.1.6 Contact splitting principle

One of the consequences of the JKR theory was the prediction of a finite pull-off force (see Equation 2.6). The pull-off force is proportional to a linear dimension of contact. For a fly, which weighs 80 mg and has a radius of the complete surface of the attachment organ of 100 µm, an adhesion energy of $1\ \text{J/m}^2$ is required [13]. So one thing has become clear, this high energy cannot be achieved by Van der Waals forces because these forces are weaker (in range from 50 to $10\,\text{mJ/m}^2$) [13]. Arzt et al. [1, 13] introduced the principle of contact splitting. It

is based on splitting up the contact into n sub-contacts with each radius R^* (see Figure 2.3). By splitting the contact, the pull-off force is increased to:

$$F'_C = \sqrt{n} F_C \tag{2.10}$$

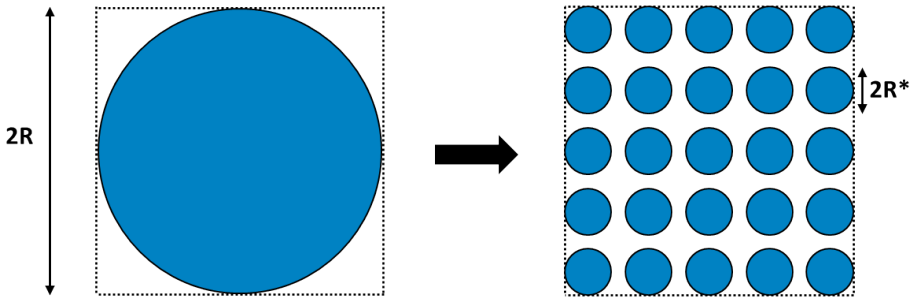

Figure 2.3: *Schematic of contact splitting: One contact is split into several smaller contacts, while the projected contact area stays constant, adapted from [14].*

In general it can be observed that the number of fibrils plays a big role for the pull-off force. The heavier an animal, the larger is the density of them (Figure 2.4).

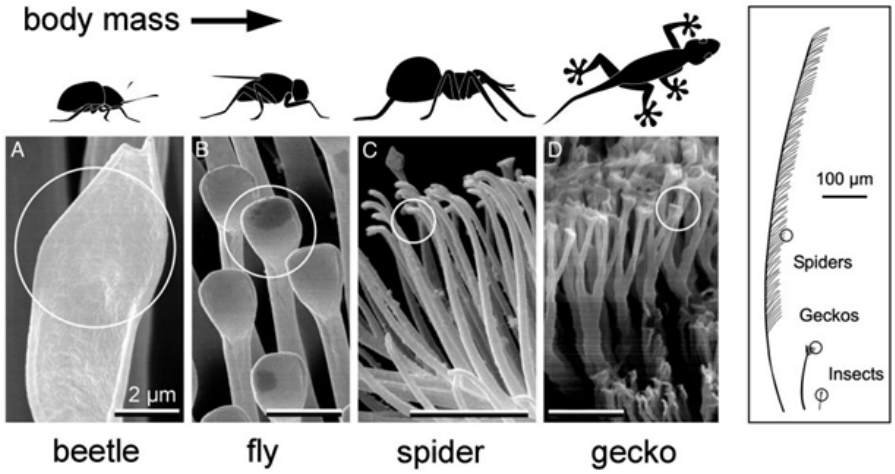

Figure 2.4: *Terminal element dimensions of an animal are inversely correlated with the body weight. They decrease with increasing body weight [13].*

For dimensionality reasons, the area of foot-to-substrate contact increases less than the weight of an animal. This problem is solved by enhancement of the setal density (Figure 2.5). The graph groups dry adhesives and liquid-mediated. Liquid-mediated adhesion systems have a

nanometer-thin film of a fluid which increases the contact area on rough surfaces. The special rheology of the adhesive film combines capillary adhesion and sliding prevention [15].

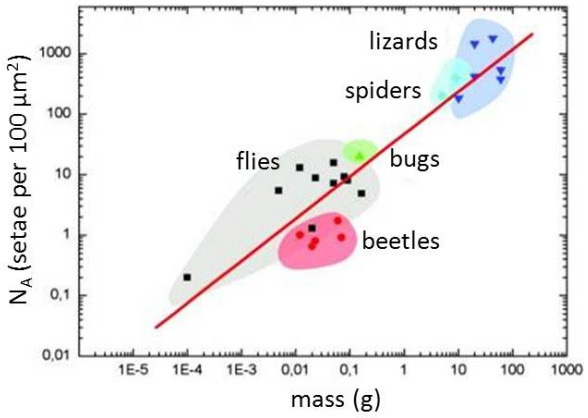

Figure 2.5: *Terminal element density of an animal is correlated with the body weight. It increases with increasing body weight [13].*

2.2 Hierarchical structures

Hierarchical assemblies often appear in nature, for example in many plants and animals. When we look at a structure with increasing magnification, new units can always be discovered. The network of hierarchical assemblies is more than just the sum of its parts. Every hierarchical level is important for the structure and, finally, for the whole system. For example, teeth or mussel shells are only so robust because of their unique hierarchical assembly.

One aim of materials research is to take advantage of long-tried materials, which exist in the long run of evolution and natural selection, and to use these principles of bio-inspired designs for engineering applications. An interesting example is the adhesive structure on the toe pads of geckos.

Geckos are the heaviest known living animals that can climb on a rough vertical or overhanging surface with their adhesive pads. They have a weight of up to 300 g. So their adhesive system must be more efficient than the one of lighter animals. The gecko relies on a good adhesion system, otherwise it could not survive in their natural habitat. Their adhesion apparatus is a very specialized system which works without any liquids (called dry adhesion system). It consists of lamellae, which contain slanted setae, branching into finer spatulae (see Figure 2.6).

The upper level of setae has a length of 30–130 µm and a diameter of 5–10 µm, and their density is about 14 000 /mm^2. In the middle level, the branches have a length of 20–30 µm and a diameter of 1–2 µm. Each of this branches exhibits 100–1000 lower level structures called spatula with a length of 2–5 µm and a diameter of 0.1–0.2 µm. The tips of the spatulae have a length of about 0.5 µm, a width of 0.2–0.3 µm and a thickness of around 0.01 µm (shown in Figure 2.7). Geckos can adhere to rough substrates but adhesion is much weaker compared to flat surfaces [16], however it suffices for rapid movement on the surface. The interaction forces between the spatulae and the surface are basically Van der Waals interactions (see Chapter 2.3.1), which act over a short range (atomic scale). Even though the energy content of a Van der Waals interaction is quite low, it plays an important role when many contacts exist, and the forces add up to a considerably large value. Therefore it is important that the spatulae of a gecko toe are small enough to interact also with a very rough surface.

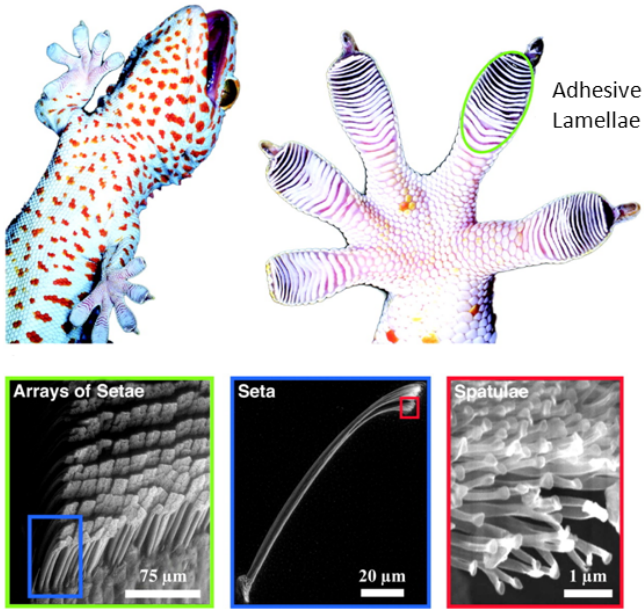

Figure 2.6: *Hierarchical structure of the gecko toe and scanning electron microscope pictures of each hierarchy level [17].*

In nature not only the high adhesion ability is important for the gecko locomotion but also the ability of rapid switching from attached to detached state and vice versa. Both legs and toes of the gecko are involved in coordinated locomotion. For the detachment process the gecko peels back its toes to a large angle as shown in Figure 2.8.

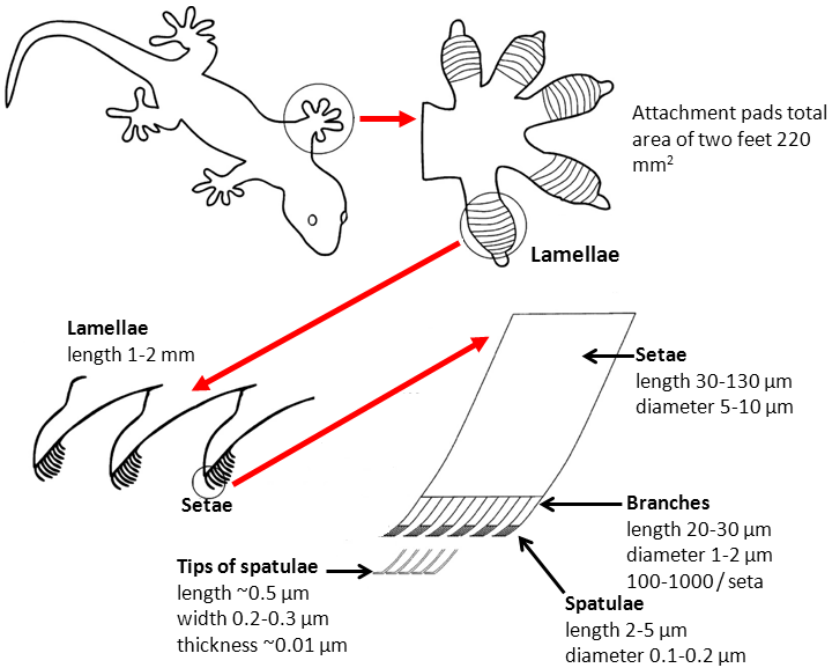

Figure 2.7: *Schematic assembly of a gecko structure with dimensions of each hierarchy level [18].*

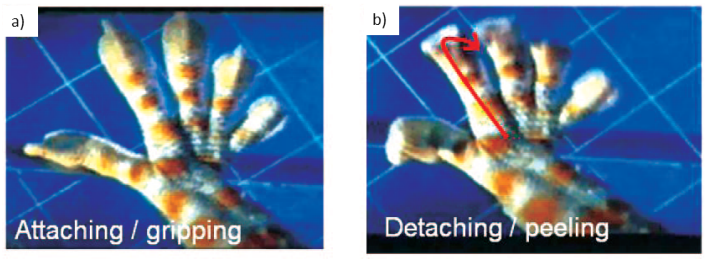

Figure 2.8: *Gecko toes during a) attaching/gripping and b) detaching/peeeling process [19].*

Owing to remarkable adhesive properties (and also to the peeling ability) of the gecko toes, it has been the goal of scientists to produce artificial structures with similar properties. Applications could lie in the medical field, for example, for eardrum operations or in automotive, packaging and sporting goods industries.

2.3 Adhesion

In an adhesion process, attractive forces exceed the repulsive forces. Attractive forces are, for example, Van der Waals forces and capillary forces. They will be explained in the next sections. Repulsive forces are for example electrostatic repulsion or on an atomic scale, caused

by the overlap of electron orbitals. Adhesion can also be decreased by stored elastic energy which causes a restoring force. Elastic potential energy is transferred to kinetic energy and is lost for the adhesion process. The forces depend on the material and the environmental conditions. For high adhesion the repulsive forces should be decreased. This can be achieved by decreasing the stored elastic energy. To this end several possibilities exist. The material can be structured for example with pillars, considering the contact splitting principle (see Section 2.1.6). With this method the number of contact points can also increase the ability to adapt to rough surfaces. The aspect ratio (height/diameter) of the pillars plays also an important role for adhesion. The greater the aspect ratio, the smaller the stored elastic energy. However, with increasing aspect ratio there is a higher risk that the pillars bond to each other. In the bound state the pillars cannot adhere well to a surface and adhesion decreases. Therefore the aspect ratio should not be too high. The critical height of the pillars is determined by the Young's modulus E, defined as ratio of tensile stress σ to tensile strain ϵ.

The reduced Young's modulus E^* is defined as:

$$E^* = \frac{E}{1-\nu^2} \tag{2.11}$$

where ν describes the Poisson's ratio.

The elastic potential energy U_{el} which is stored in a material is given by following equation:

$$U_{el} = \frac{\sigma \epsilon V}{2} = E\frac{\epsilon^2}{2}V \tag{2.12}$$

The equation shows that a higher Young's modulus E and higher volume V at constant tensile strain ϵ, leads to a higher elastically stored energy U_{el}; this appears to be detrimental to adhesion, but can prevent the condensation of pillar structures (this can follow to a reduction in adhesion [20]). Therefore an optimum has to be found for the volume and the Young's modulus of a structure, to achieve a high adhesion force.

2.3.1 Van der Waals interactions

In general, Van der Waals interactions are short-range interactions between two bodies which are electrically neutral. The interactions result from the charge distribution in the solid and can be grouped as follows [21]:

- Keesom-interaction: interaction between two permanent dipoles:

$$U_{Keesom} = -\frac{{\mu_d}^4}{k_B T r^6} \tag{2.13}$$

- Debye-interaction: interaction between two induced dipoles:

$$U_{Debye} = -\frac{\eta {\mu_d}^2}{r^6} \tag{2.14}$$

- London-dispersion: interaction between uncharged, unpolarised atoms and molecules, caused by fluctuating dipole moments:

$$U_{London} = -\frac{3}{4}\eta^2 h^* \frac{f}{r^6} \tag{2.15}$$

where r is the distance of two bodies, η the polarizability, μ_d the dipole moment, h^* the Planck's constant, f is the dispersion energy, k_B the Boltzmann's constant and T the temperature.

The Van der Waals potential results in [21]:

$$U_{VdW} = U_{Kessom} + U_{Debye} + U_{London} \tag{2.16}$$

The interaction potential decreases with radius to the power 6. That means that this kind of interaction plays an important role for short distances, while for long distances it can be neglected. The energy content of a Van der Waals interaction is quite low. But in a solid, the Van der Waals interactions of all pairs of atoms can add up to a large value.

The work of adhesion γ, which describes the separation energy of two surfaces from distance d to infinity, is given by the following equation [22]:

$$\gamma = -\frac{H^*}{12\pi d^2} \tag{2.17}$$

H^* is the Hamaker constant [23] that allows for determining the interaction coefficient between two particles on which a Van der Waals interaction acts. For β-keratin it is assumed to be 10^{-19} J [24].

2.3.2 Capillary forces

Capillary forces occur because of surface tension of liquids and interface tension of liquids with a solid. A schematic of the capillary effect is shown in Figure 2.9. It can be separated into two parts: the Laplace force F_L and the surface tension force F_S. The total capillary force, F_{cap}, is the sum of the two components [25]:

$$F_{cap} = F_L + F_S \tag{2.18}$$

The Laplace force F_L is given as [27]:

$$F_L = \pi\kappa\Gamma R^2 sin^2\varphi \tag{2.19}$$

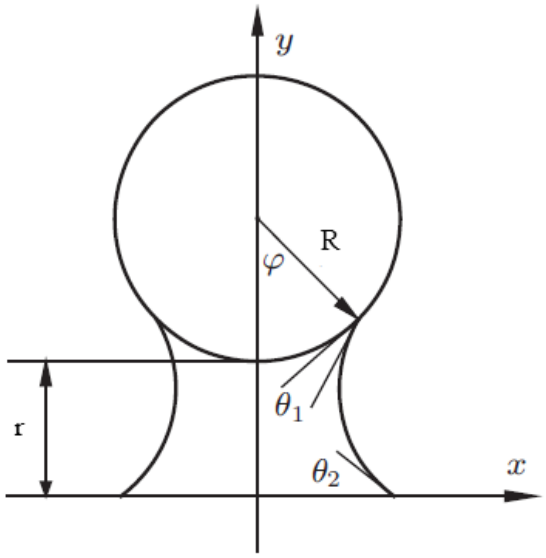

Figure 2.9: *Schematic of the capillary effect between a sphere and a substrate with a liquid volume; R is the sphere radius, θ_1 and θ_2 are the contact angles on sphere and plane, r is the distance between object to the radius and φ is the filling angle of the meniscus [26].*

where κ is the mean curvature of the meniscus, Γ is the surface tension of the liquid, R the tip radius and φ the filling angle.

From the so-called Kelvin equation [25] the mean curvature of the meniscus, κ, can be determined as:

$$\kappa = \frac{R_{gas}T}{\bar{V}\Gamma} ln\left(\frac{p_a}{p_0}\right) \tag{2.20}$$

where R_{gas} is the ideal gas constant, $\bar{V}$ is the molar volume, p_0 the saturated vapor pressure of the liquid at temperature T and the ambient pressure p_a acting outside the curved surface. The ratio of p_a to p_0 is also called relative humidity. The surface tension force F_S which acts on the sphere is [27]:

$$F_S = 2\pi R\Gamma \sin\varphi \sin(\theta_1 + \varphi) \tag{2.21}$$

The total capillary force F_{cap} on the sphere is:

$$F_{cap} = \pi R\Gamma[2\sin\varphi\sin(\theta_1 + \varphi) - \kappa R\sin^2\varphi] \tag{2.22}$$

where θ_1 is the contact angle on sphere with a liquid volume. It has to be noted that it is unclear whether capillary forces act in the adhesion ability of a gecko to adhere. There are different opinions in the literature about this topic [25, 28–32]. Probably Van der Waals forces and capillary forces both play an important role in adhesion.

2.3.3 Adhesion on rough surfaces

Strong adhesion between a stiff, rough surface and a nearly flat counterpart surface is difficult to achieve. Only few contact points exist between the two materials, see Figure 2.10, even if the counterpart surface is very flexible. Few contact points result in low adhesion force due to the short range adhesive forces.

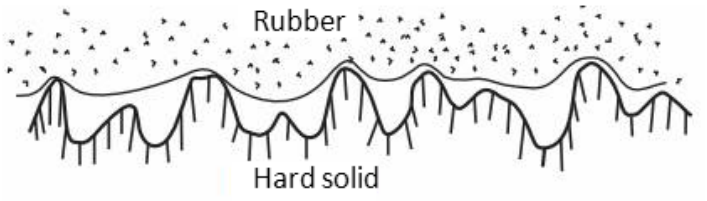

Figure 2.10: *Contact between rubber and a hard and very rough surface, adhesion is imperceptible [16].*

Nearly everything in our surroundings has a certain roughness. Thus idealy, biomimetic adhesives should also adhere on engineered, rough surfaces. So it is of great interest to know the exact influence of roughness on adhesion of biomimetic adhesives. In the last decades the influence of roughness of two elastic bodies was investigated for artificial [10, 33–35], but also for biological [36–40] systems. Huber et al. [41] studied the influence of surface roughness on the adhesion ability of the gecko. They could show that the effective adhesion has a minimum for a certain range of roughness (root mean square roughness RMS = 100–300 nm). Figure 2.11 explains this phenomenon.

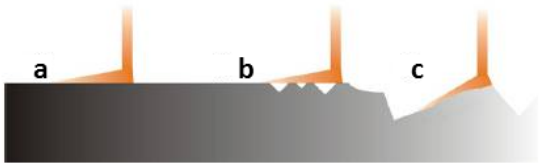

Figure 2.11: *Illustration of adhesion measurements on different RMS roughness: a) Spatula can adhere well to very low roughness. b) Spatula on a surface with intermediate roughness; only few contactpoints exists. c) On surfaces with higher roughness the spatula can adhere well again [41].*

For relatively low roughness, the spatula can adapt very well to the substrate with many contact points. For intermediate roughness the spatulae can only adapt with a few contact points. At higher roughness, the spatulae are able again to adapt to the surface. The influence of surface roughness on biomimetic adhesives was investigated by several working groups [42–45]. To adhere on a rough surface, there is a need to increase the number of contact points. This can be achieved for example with a surface with long fibers like on a toe pad of a gecko, see Figure 2.12. This has the advantage that they can better adapt to irregularities of a surface.

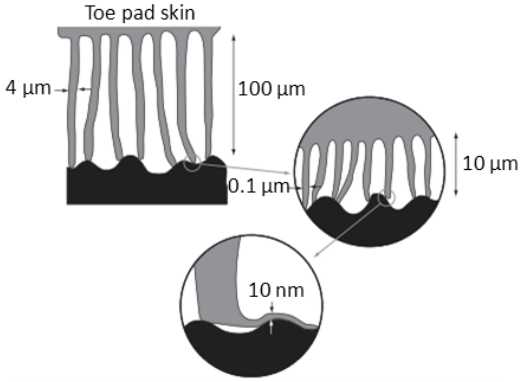

Figure 2.12: *Schematic of thin fibers of the gecko in contact with a rough surface [16].*

Furthermore biological adhesion pads are built in addition in a hierarchical way because of the fact that they consist of an elastically stiff material.

2.3.4 Adhesion measurement techniques

To determine the adhesion strength different tools and testing methods were developed. In general, they can be divided in two groups: adhesion and shear/friction measurements. The

substrate is pressed with a defined preload perpendicular to the sample surface and the sample is moved. For normal adhesion investigations, the force parallel to the preload is measured [46–54, 54–70]. For shear/friction investigations, the force perpendicular to the preload is detected [19, 47, 71–80]. For peel-tests, the sample is removed from the substrate at a defined angle [68, 74, 81, 82]. Combinations of this three different classes are possible. In this thesis only the normal force was measured.

2.4 Spring model of hierarchical gecko structures

In Section 2.1.6 it was shown that by dividing the contact into a large number of small contacts, the pull-off force increases. However this model only considers contact with a flat surface. For rough surfaces the compliance and the adaptability is crucial to achieve high adhesion. Intuitively, a hierarchical structure can better adapt to a naturally rough surface than a one level structure. To confirm this assumption it is necessary to do experiments and/or model simulations.

Bhushan et al. [83] and Kim and Bhushan [18, 84, 85] used a hierarchical spring model to describe the adhesion behavior of a gecko seta to a rough surface. The model consists of three hierarchy levels. The upper level of springs should describe the thicker part of seta, the middle spring level should describe the branches, and the spatulae are described by the lower level of springs (shown in Figure 2.13). In their analysis [18, 83–85], they assumed that the tips of spatula and the rough surface are spherical with constant radius. Autumn et al. [86] showed that an angle α of 30° between substrate and gecko's seta is the optimal angle for attachment experiments. Therefore this angle was fixed for the theoretical studies but is not drawn in Figure 2.13.

If a normal force F_n aligned to the substrate acts, there will be bending δ_b and compressive deformation δ_c [55]:

$$\delta_b = \frac{F_n cos\alpha {L_m}^3}{3EI}; \qquad \delta_c = \frac{F_n sin\alpha L_m}{AE} \tag{2.23}$$

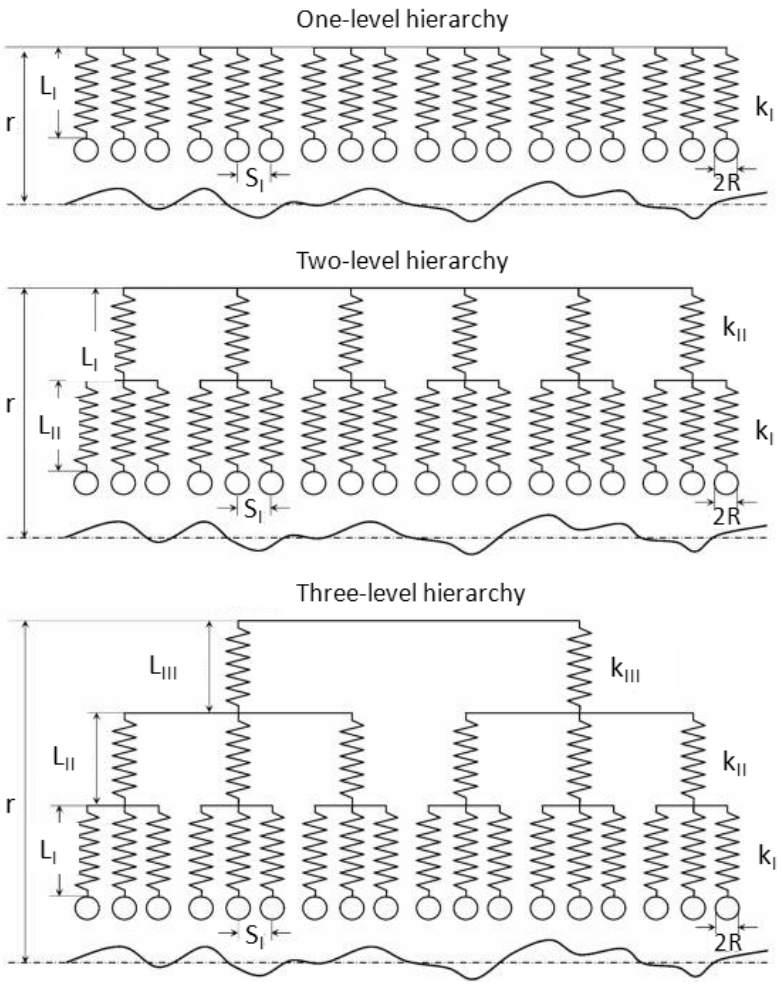

Figure 2.13: *One-, two- and three-level hierarchical spring models which simulate the hierarchical structure of gecko seta with a rough surface.* $L_{I,II,III}$ *describes the length of structure,* S_1 *the space between spatulae,* $k_{I,II,III}$ *the stiffnesses of structures. The different levels are described by indeces* I, II *and* III. *The tip radius is* R *and the distance between upper spring base and the mean line of the rough surface is the distance* r *[84].*

E is the Young's modulus, I describes the moments of inertia with $I = (\pi {R_m}^4)/4$; $A = \pi {R_m}^2$ is the cross-sectional area, L_m/R_m are the length/radius of seta branches.

The net displacement of the assembly $\delta_\perp$ is [55]:

$$\delta_\perp = \delta_c sin\alpha + \delta_b cos\alpha \tag{2.24}$$

With Equations 2.23 and 2.24 the stiffness of seta branches k_m is given by [55]:

$$k_m = \frac{\pi {R_m}^2 E}{L_m sin^2\alpha (1 + 4{L_m}^2 cot^2\alpha/(3{R_m}^2))} \tag{2.25}$$

Gecko setae structures are composed of β-keratin which has a high elastic modulus (1–15 GPa [87]) and are close to DMT model [25], see Equation 2.7.

The effects of hierarchy with one, two and three levels of hierarchy were simulated. It was assumed that the springs and connecting plate are rigid [83]. On each upper level are ten springs, therefore level III is connected to ten springs on level II, and ten springs are on level I. In the simulations random rough substrates were used, which were generated by a software program [88].

Kim and Bhushan [84] calculated the adhesion coefficient (ratio of pull-off force to applied force), number of contacts per unit length and adhesion energy of their multilevel spring model. They have shown that with increasing applied load the adhesion force increases, until the adhesion force has achieved constant values. They have also shown that the stiffness of the springs is very important. The three-level model which has a third level stiffness of $0.1\,k_{III}$, shows a 20–30 % higher adhesion in comparison to a three-level model which has a third level stiffness of k_{III}. They have shown that a three-level model shows a higher relative increase in adhesion, contact numbers and adhesion energy than two and one level models. Furthermore it was shown that substrate roughness reduces the adhesion force. But the simulations predict also a certain roughness at which the gecko cannot stick to a wall although in reality the gecko

can cling to walls with higher roughnesses [84]. This indicates that the lamellar structures on the toes of geckos are also important. So Kim and Bushan propose that the lamellae adapt to the macrorough surface, and the setae to the micro- or nanoroughness.

2.5 Bioinspired adhesion systems

During the last few years several possibilities were developed to produce bioinspired adhesion systems. In this section some important examples and related adhesion measurement results will be presented.

Greiner et al. [89] fabricated two-level structured surfaces with two-step photo-lithography. He investigated the pull-off force of two-level structures and compared them with one-level structures. A schematic of the two-step photo-lithography is shown in Figure 2.14. In a first step the finer structure is built into a so-called SU-8 film by masked irradiation. SU-8 is a commercial epoxy-based negative resist. With ultraviolet light it is possible to cross-link the molecular chains of SU-8. With a second SU-8 coating step the upper structure is built. After the second irradiation step the film can be treated with a developer. All structures, which were exposed, remain after development and the unexposed area is dissolved. The desired hierarchical pillar structure of PDMS can be obtained by a last step, the demolding process of the negative SU-8 structure, as shown in Figure 2.15.

For the adhesion measurements Greiner et al. [89] used a spherical substrate, and the radius of the substrate was much larger than the individual structures. They found that the pull-off force was increased with increasing aspect ratio of the pillar structures, but they did not observe an improvement of the pull-off force with his hierarchical structures. This is in contrast to the theoretical gecko hair model results of Yao et al. [90–92]. They observed an increase in adhesion with increasing structural levels of hierarchy. But they stressed that the nanometer length scale could play an important role.

A further method for fabrication of bioinspired materials is the electrochemical anodization for obtaining porous anodic alumina (PAA) [20, 93–97]. In the last years, progress was made in improving ordering of the porous material. The advantage of this method is the fine porous structure with high aspect ratio. The structure of porous PAA can be described as a

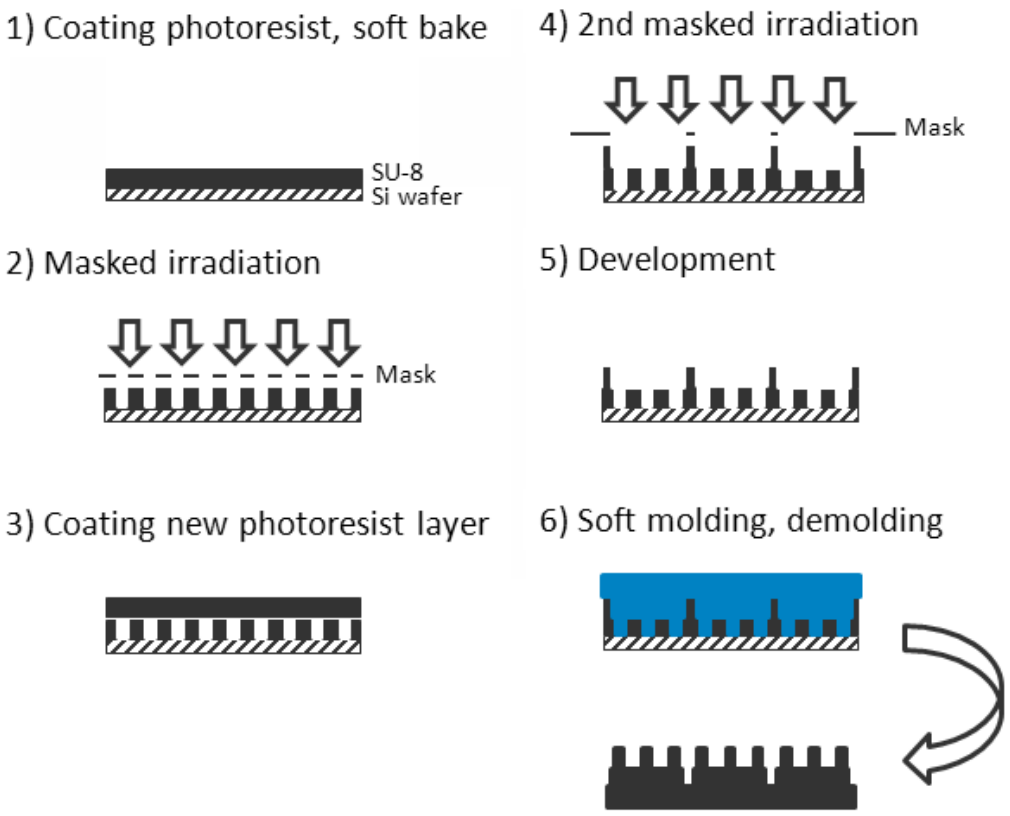

Figure 2.14: *Schematic of the two-step photo-lithography and softmolding, adapted from [89].*

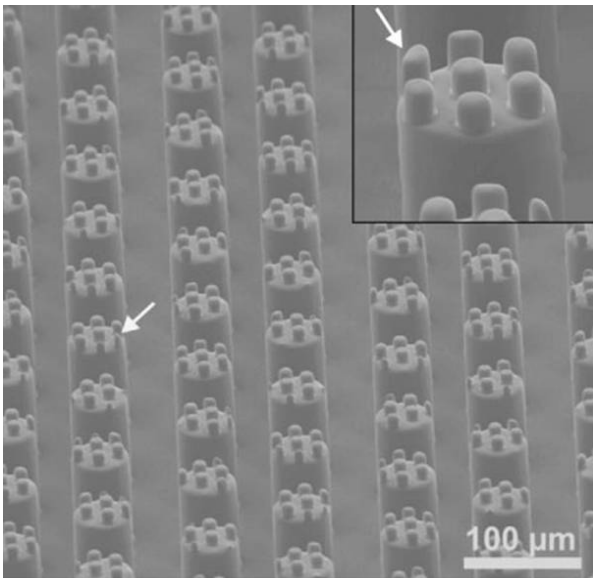

Figure 2.15: *SEM image of hierarchical pillars fabricated with SU-8 photolithographic templates [89].*

honeycomb structure consisting of columnar alumina cells (see Figure 2.16). PAA is formed by an anodization process of aluminum in acidic or basic electrolyte solutions. The dimensions of the anodic porous alumina cells can be determined by the anodizing conditions, which are the electrolyte composition, temperature, period of anodization and applied voltage. A PAA film is shown in Figure 2.17.

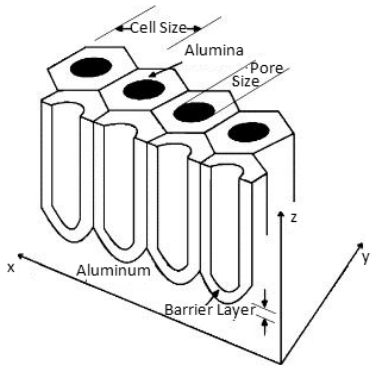

Figure 2.16: *Schematic of a PAA film on aluminum [98].*

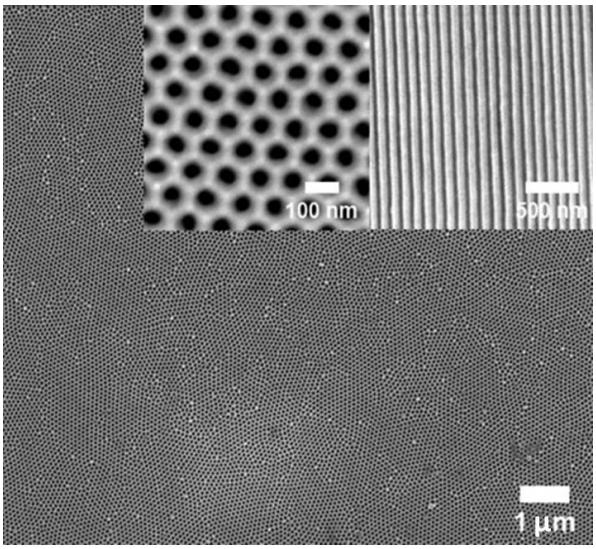

Figure 2.17: *SEM pictures of self-ordered pore configuration of PAA templates (insets: magnification of top and cross-sectional views) [20].*

Meanwhile, PAA templates are frequently used to fabricate hierarchical structures [20, 93–97]. Kustandi et al. [20] fabricated a hierarchical template for soft molding with a two-step anodization procedure, which allowed an infiltration of polymethylmethacrylate (PMMA). In Figure 2.18 a schematic of the process is shown. The process began with a first anodization step carried out in an oxalic acid solution at constant voltage. A mixture of acids removed

the first porous alumina layer. A concave pattern remained. Under different anodization conditions two different PAA membranes were prepared. The aim was to obtain a thick and a thin membrane, which can be bonded and can be used as a hierarchical template for a polymer.

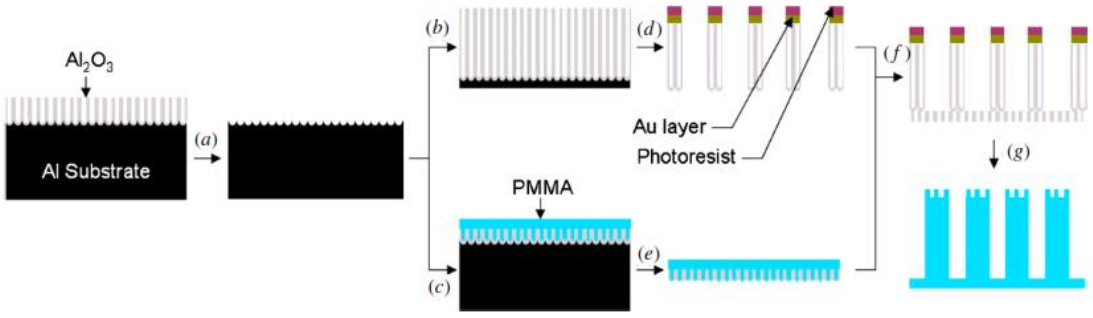

Figure 2.18: *Schematic of the fabrication process: a) Fabrication of concave patterns on the Al substrate, b) anodization for 8 h (25°C), c) anodization for 15 min (2°C) and infiltration of PMMA (120°C), d) micropatterning and Al - Al_2O_3 separation, e) Al - Al_2O_3 separation and pore widening by etching, f) bonding of the two alumina membranes, g) infiltration of PMMA and removal of the template [20].*

The finished structures of a two-level hierarchical microfibril array of Kustandi et al. [20] and Lee et al. [96] are presented in Figure 2.19. The neighboring smaller fibrils bundle together, because of surface adhesive forces and this can follow to a reduction in adhesion [20]. The diameters and lengths of the fibrils reflects the dimensions of the template. The bundling of the fibrils should be prevented in the future to get higher adhesive structures.

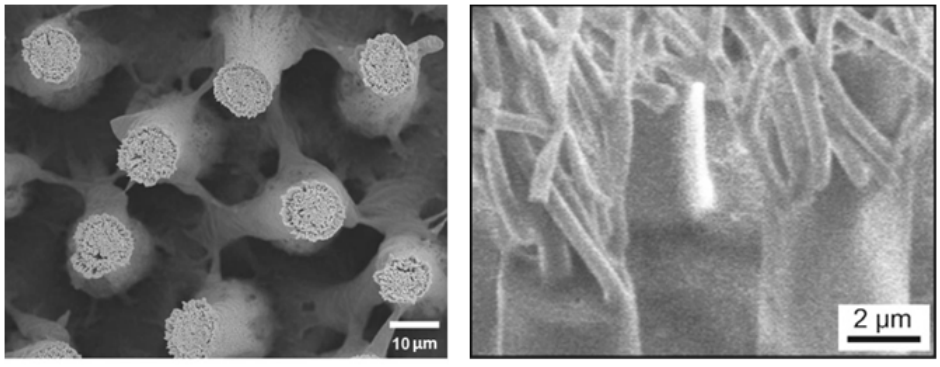

Figure 2.19: *SEM micrograph of hierarchical microfibril arrays [20, 96].*

The dipping technology as presented in Figure 2.20 is used by Murphy et al. [99] to achieve fibers at the microscale with controlled fiber tip shape. For this purpose, pillars which are wetted with a polymer (polyurethane) are placed over a silicon mold. After curing of the

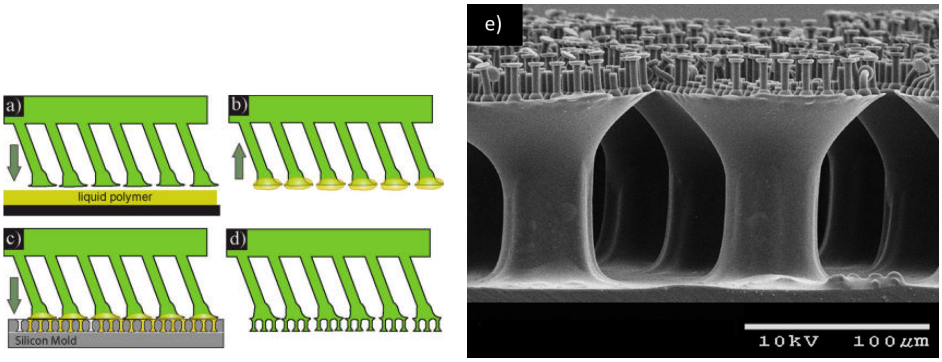

Figure 2.20: *Fabrication process of hierarchical microfibrillar adhesives: a) Fibers were dipped into a liquid polymer. b) The fiber tips are wetted by the liquid polymer. c) The fiber array is pressed against an etched silicon mold; the liqid is flowing into the mold. d) After polymer curing the mold can be removed by a dry etching process. e) SEM image of the polyurethane hierarchical fibers [99].*

polymer a two-level hierarchy is obtained. The adhesion measurements on the two-level structure show that hierarchy increases the adhesion in comparison to a single-level structure, see Figure 2.21.

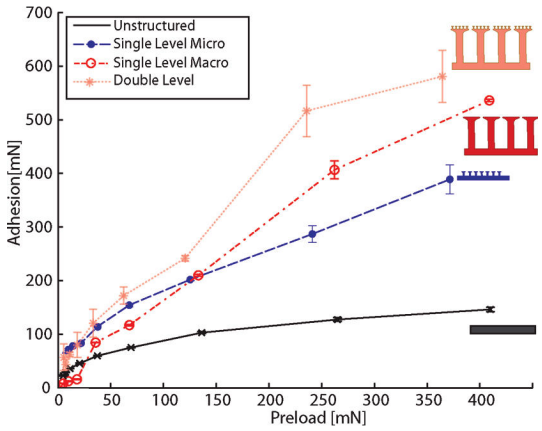

Figure 2.21: *Dependence of adhesion on applied preload of unstructured, single-level micro, single-level macro and two-level structure. Standard deviations are represented by error bars. The two-level structure shows the highest adhesion [99].*

This section presented several methods which were developed to fabricate hierarchically patterned pillar structures and showed that theoretical simulations with hierarchical pillar structures exist; however, there is no clear opinion whether hierarchy really helps or what the influence of hierarchy is on adhesion.

2.6 Elastic buckling of pillars

When a certain load acts on a straight pillar a buckling process occurs and the pillar axis buckles laterally. In 1757 Euler described four different cases for the buckling of an elastically bar with axial working pressure. The cases differ in clamping of the pillars (shown in Figure 2.22).

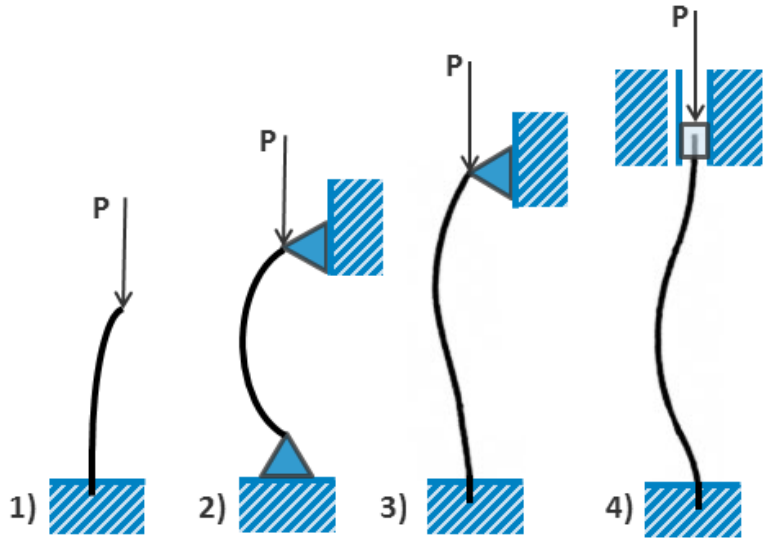

Figure 2.22: *Buckling length of a pillar depends on bearing conditions: 1) clamped at one end; 2) flexible bedded at both end; 3) one end: clamped, the other end: flexible bedded 4) clamped on both sides, adapted from [100].*

It is possible to predict deflections, stresses, moments, etc., on the basis of the initial configuration of a pillar [55]. The critical load, the buckling load P_B, is determined from the so-called Euler equation:

$$P_B = m^2 \frac{\pi^2 E^* I}{L^2} \tag{2.26}$$

where m is the pre-factor depending on the clamping condition of the pillar (clamped-clamped: $m = 2$; clamped-hinged: $m = 1$; clamped-free to rotate, and translate: $m = 3/2$); E^* describes the plain strain modulus $E^* = E/(1 - \upsilon^2)$; I the area moment of inertia, and L the length of the pillar.

The Euler equation can help to predict the critical force P_B of a biomimetic structure which is covered with pillars. For sensitive structures it is very useful to know the critical force; forces above the critical force causes buckling and can provoke damage. If the critical force is exceeded, the adhesion force declines, because most of the pillars retain a slight bend after buckling and contact points get lost [101].

Nearly 200 years after Euler, Maurice A. Biot calculated that the Euler equation is only valid for pillars with aspect ratios above 10 [102] and found a solution based on the elasticity theory for thick pillars (aspect ratios under 10) under axial compression [102].

2.7 Colloidal lithography

Besides classical lithography there exists an alternative route to produce microstructured surfaces, i. e. colloidal lithography. Particle monolayers can be created by using Langmuir-Shaefer-like techniques [103–107], drop-casting [108], dip-coating [109], controlled drying [109, 110], spin coating [111, 112], and electrochemical deposition using a conventional three-electrode configuration [113, 114]. The mechanism of convection assisted particle assembly [115] plays a role in several of the approaches and yields dense particle monolayers with areas of several square centimeters. The particle monolayers can be transferred into an underlying substrate through several methods, for example shadowed evaporation, reactive-ion etching [108, 112, 116–118], electrochemical etching [119], vapour-liquid-solid growth [120], and metal-assisted chemical etching [121]. The most common approach is presented in Figure 2.23.

The size of ordered close-packed crystals of colloidal polystyrene spheres was controlled by etching. The particles can be sputtered with a metal and, after removal of the particles, the substrate can serve as an etching mask for an etching process [121]. Variations of the mask were achieved by variation of the sputter angle. In a second approach core-shell particles were used, which consisted of a core metal particle and a surrounding polymer shell [122, 123]. The shell can be etched away and the metal core particles remain on the substrate in a regular hexagonal array, which can be etched directly into the substrate by a metal-assisted chemical

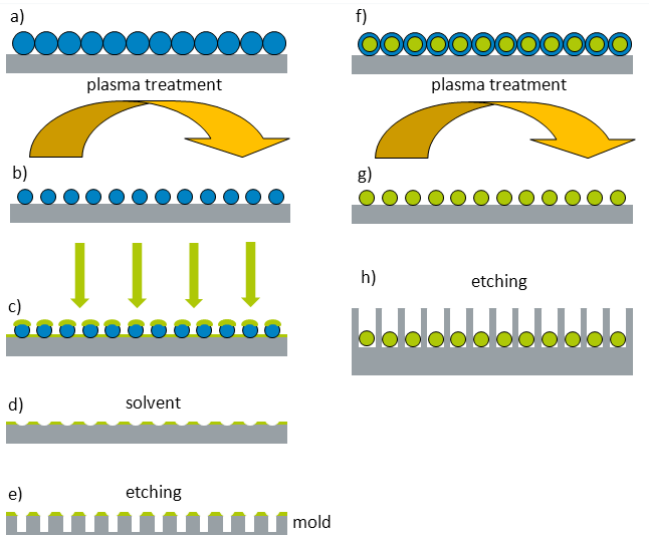

Figure 2.23: *Schematic of a mold fabrication with colloidal lithography: a) fabrication of a polystyrene particle dense packed monolayer, b) etching of the particles by plasma treatment, interspaces develop between the particles, c) sputtering of the particles with a metal, d) removing of the particles with a solvent, e) only the unsputtered areas will be etched; columns form in the substrate which can serve as a mold. f) Fabrication of a dense packed monolayer with core shell particles, g) plasma treatment, the surrounded polymer shell is etched away; the metal particles leave in a regular hexagonal array, h) the metal particles are etched directly in the substrate.*

etching process. The challenge is to achieve monodisperse particles with small deviation from a spherical shape with current core-shell syntheses.

Brodoceanu et al. [124] developed an inverse strategy: metal shell-polymer core particles. Polymer particle monolayers were coated with a gold thin film. Afterwards the polymer cores were removed by thermal annealing at 500–700 °C which produced metal particles with long-range order. A schematic is presented in Figure 2.24. The metal particle size and metal interparticle distance depended on the size of the polymer particles and the thickness of the metal coating.

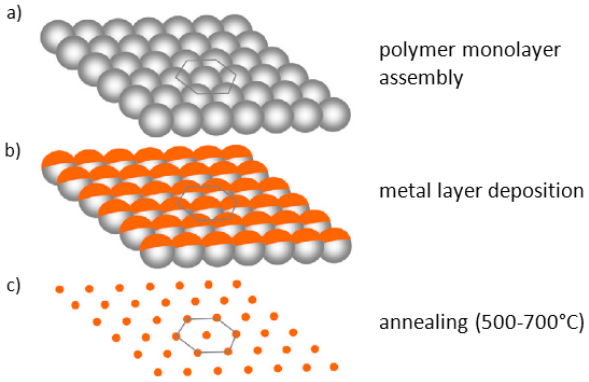

Figure 2.24: *Schematic of the three-step process to produce metal nanoparticle arrays: a) assembling of a polymer monolayer, b) metal layer deposition, c) annealing results in an array of metal nanoparticles [124].*

In general, the advantage of colloidal lithography is the ability to fabricate structures in sub-µm range. The disadvantages of the colloidal lithography are on one hand defects in the hexagonal array of the colloids which affects the patterning; on the other hand there is a limitation in the feature size because the particle size and the interspace distance cannot be separately manipulated. In addition the etch treatment influences the spherical shape of the particles and the substrate roughness may increase.

2.8 Particle based softmolding

The method called particle based softmolding uses colloidal crystals as master molds and is well known in the literature [125–129]. An example for such a fabrication process is presented in Figure 2.25.

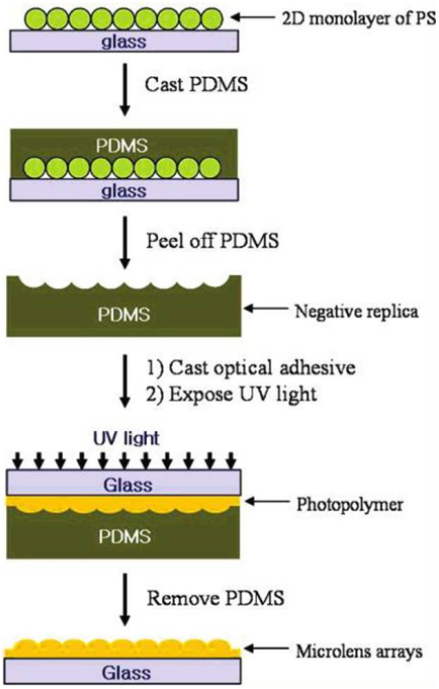

Figure 2.25: *Schematic of fabrication of hemispherical polymer microlens arrays. PDMS molding of polystyrene spheres assembled on glass serves as negative replica [125].*

A two-dimensional colloidal monolayer of polystyrene (PS) particles is prepared by spin-casting onto a glass substrate and is molded by PDMS to fabricate structured negative replica, for example for UV-cured photopolymers. This method fabricates microlens arrays, e. g. for optical systems such as optical fibers that need high quality with minimal defects.

2.9 Discussion and aim of this thesis

The state of the art showed that there exist some fabrication methods of hierarchical bioinspired surfaces which mainly focus structures in the micrometer range. It appears that the focus of most fabrication processes lies on the fabrication of identical copies of natural structure geometries, but a thorough understanding of the respective contact mechanism is missing. Up to now, no clear picture exists of the advantages of such hierarchical structures, except for a few theoretical studies. There are many questions and parameters which are insufficiently or poorly understood. Examples are (see Chapter 4):

- Is it possible to fabricate a hierarchical fibrillar model with different hierarchy levels ranging several orders of magnitude in size?
- Is it possible to better understand the contact formation and deformation phenomena-like, buckling, and adhesion behavior of a hierarchical structure?
- Which influence has micro- and macroroughness on buckling and adhesion of hierarchical structures?
- Does the introduction of a hierarchy to a structure lead to a benefit in its adhesive performance?

Further important questions (see Chapter 5) are:

- Is it possible to find a new route to fabricate small structures (down to nanometer range) which allow large scale patterning at the same time?
- Is it possible to influence micropatterned molds for fabrication of bioinspired adhesives by systematically evaluate the etching process of particles depending on particle size, plasma power, etching time, particle density?
- Is it possible to mold particle based templates to obtain adhesive structures?

The goal of this thesis is to find answers to these questions.

3 Experimental

A method was developed to obtain macroscopic hierarchical pillar structures in the millimeter range by molding with milled aluminum casting molds in different sizes. Further the geometry of the pillar tips was modified by a dipping process. Adhesion measurements were done on different substrates using the obtained structures. Furthermore close- and nonclose-packed particle monolayers were fabricated to analyze the size and shape evolution during oxygen plasma treatment. The individual fabrication, preparation steps and measurements will be explained in the next subsections.

Two subsections of this chapter were accepted for publication: C. T. Bauer, E. Kroner, N. A. Fleck, and E. Arzt, Hierarchical macroscopic fibrillar adhesives: In-situ study of buckling and adhesion mechanisms on wavy substrates, *Bioinspiration Biomimetics*, 2015 [2], and are marked with a footnote.

3.1 Macroscopic pillar experiments

3.1.1 Preparation of hierarchical macroscopic pillars[1]

Different straight self-similar cylindrical PDMS pillars (dimensions see Table 3.1.) of hierarchical macroscopic levels were fabricated using milled aluminum casting molds (Figure 3.1). As molding material, polydimethylsiloxane (PDMS) was chosen for its properties in replication precision and handling.

[1] This subsection is content of C. T. Bauer, E. Kroner, N. A. Fleck, and E. Arzt, Hierarchical macroscopic fibrillar adhesives: In-situ study of buckling and adhesion mechanisms on wavy substrates, *Bioinspiration Biomimetics*, 2015 [2], but does not contain the first paragraph and Figure 3.1.

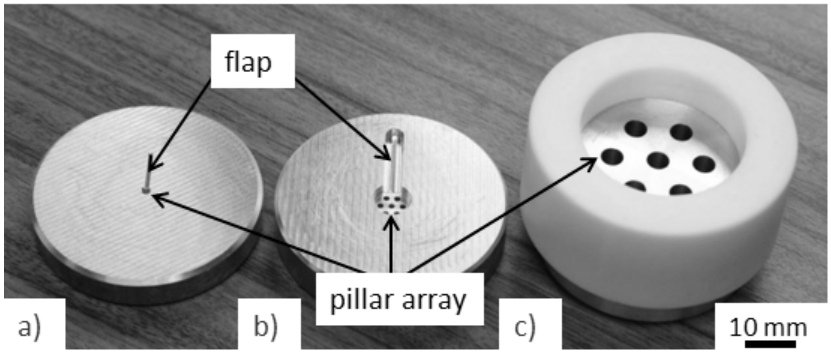

Figure 3.1: *Milled aluminum casting molds with the hexagonal pillar array a) size 3; b) size 2; c) size 1. Size 3 and size 2 has in addition a flap to enable a better demolding of the molded material.*

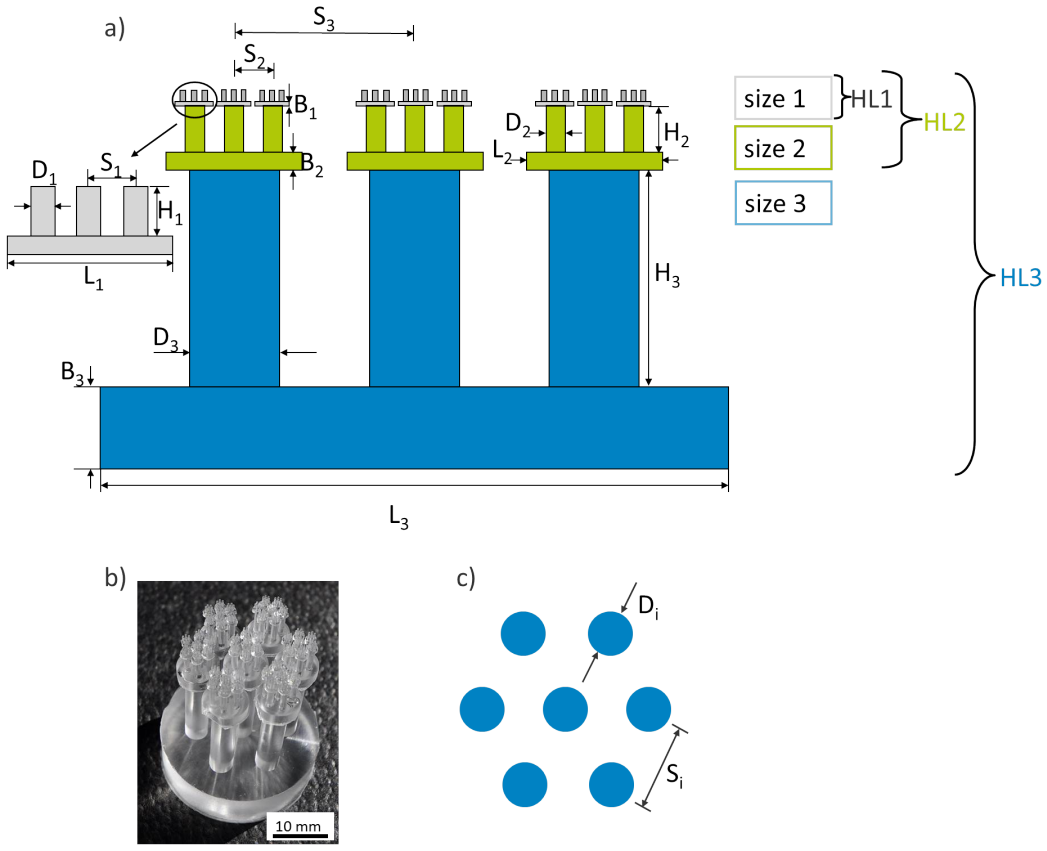

Figure 3.2: *Hierarchical assembly of the macroscopic pillars. a) Schematic overview of the hierarchical assembly; b) photograph of a sample with three hierarchy levels (HL3); c) end view of hexagonal arrangement of 7 pillars at each level of hierarchy.*

Table 3.1: *Geometric parameters of the PDMS structures for different hierarchy sizes.*

parameter	size 1	size 2	size 3
H_i(mm)	1.2	4.9	19.5
D_i(mm)	0.3	1.2	4.8
L_i(mm)	2.1	8.4	33.6
B_i(mm)	≈ 0.8	≈ 2.5	≈ 7.0
S_i(mm)	0.6	2.4	9.6
$I_i(m^4)$	$4.0 \cdot 10^{-16}$	$1.0 \cdot 10^{-13}$	$2.6 \cdot 10^{-11}$
E_i(MPa)	2.4 ± 0.2	3.0 ± 0.5	2.6 ± 0.1

At each level of hierarchy, a set of 7 pillars was arranged in a hexagonal pattern with a central pillar, see Figure 3.2c. Each set was bonded to the top of a larger pillar at the next hierarchy level. This pattern was repeated on moving up the scale of dimension, such that there are 3 levels of hierarchy, with a linear scale factor of ca. 4 on moving from one size to the next. The smallest pillars, 'size 1', are of diameter $D = 0.3\,\text{mm}$, the intermediate pillars, 'size 2', are of diameter 1.3 mm and the largest pillars, 'size 3', are of diameter 4.8 mm. The center-to-center spacing S of each structure equals twice the pillar diameter. H is the height of the pillars, L the width of the backing layer, and B is the thickness of the backing layer. Table 3.1 summarizes the dimensions of the pillars in terms of the parameters, as defined in Figure 3.2, and presents the magnitude of the second moment of area I and Young's Moduli E, which were measured by beam deflection of each pillar under a transverse load. Typical errors of the sizes H_i, D_i, L_i and S_i can be assumed as 2–10 %. Samples were prepared with one hierarchy level (HL1), consisting of only size 1 pillars, two hierarchy levels (HL2) with size 1 and size 2 pillars, and three hierarchy levels (HL3) with size 1, size 2 and size 3 pillars. Figure 3.2 shows a HL3 sample as schematic (Figure 3.2a) and as photograph (Figure 3.2b).

Samples were cast in PDMS using aluminum alloy molds, as reported previously [130, 131]. The PDMS material was prepared by mixing the pre-polymer and cross-linker in a 10:1 ratio from the *Sylgard 184* kit (Dow Corning Ml, USA). To remove air bubbles, the mixture was degassed in a desiccator. After pouring into the casting molds, the PDMS was fully cured in an oven for more than 12 hours at 75°C. Subsequently, the PDMS pillar structure was peeled from the mold and excess material was removed with a scalpel. The pillars of different size

were bonded by a droplet of uncured PDMS, followed by a thermal cure. The above process steps produced PDMS samples with a Young's modulus $E = 2.4$ to $3.0\,\mathrm{MPa}$ as measured by tensile tests (see next subsection). Single pillar size 1 structures were fabricated in the same manner as described before but after the demolding process the pillars around the middle pillar were removed with a scalpel so that only one pillar remained.

3.1.2 Determination of Young's moduli

The Young's Moduli of the pillars of the different hierarchical levels were measured by deflection under transversal load. The pillars were clamped and pure transverse loading F was applied (see Figure 3.3).

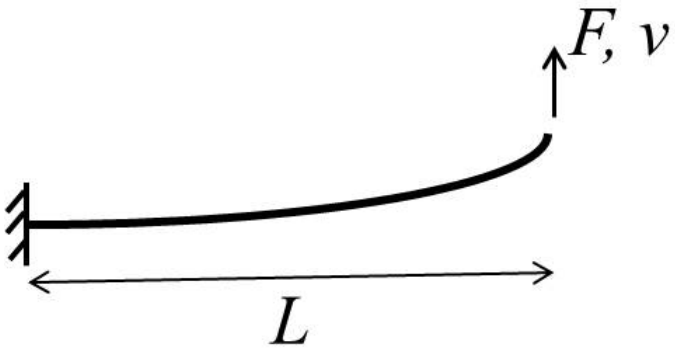

Figure 3.3: *Deflection under transversal load method to determine Young's Modulus* E.

The Young's Modulus E can be determined over the length L, the end deflection ν and second moment of area $I = (\pi/4)\, r^4$:

$$E = \frac{FL^3}{3\nu I} \tag{3.1}$$

3.1.3 Vapor phase silanization

A silanization procedure leads to a hydrophobic layer on the substrate and facilitates the demolding process. The vapor phase silanization procedure was done by placing a 50/50

mixture of perfluorodecyltriethoxysilane and hexane in a desiccator with the casting molds or glass slides, until complete evaporation occurred under vacuum. The substrates were placed such that all areas were accessible for vapor-phase molecules. The silanized samples were maintained at 95°C for 30 min to stabilize the silanized surface by increasing cross-linking.

3.1.4 Preparation of mushroom tips on size 1 pillars

To prepare mushroom tips on size 1 pillars with better reproducibility in comparison to a hand-made dipping process, a dipping tool was developed (see Figure 3.4). It contains a sample holder, which attaches the sample by under-pressure and detaches the sample by over-pressure. With screws it was possible to change the position between the sample holder and the underlying surface. By dipping the set of 7 pillars, each size 1 pillar was pressed against a thin layer of uncured PDMS for 5 min. After this time the sample was withdrawn from the surface and small droplets of liquid PDMS were observed on the tips of the dipped size 1 pillars. These were pressed against a silanized glass slide for 5 min to form a mushroom tip. After curing for 12 h at 75 °C, the structure was peeled from the glass slide. Under the light microscope mushrooms on the tips of size 1 pillars were visible, as presented in Figure 3.5.

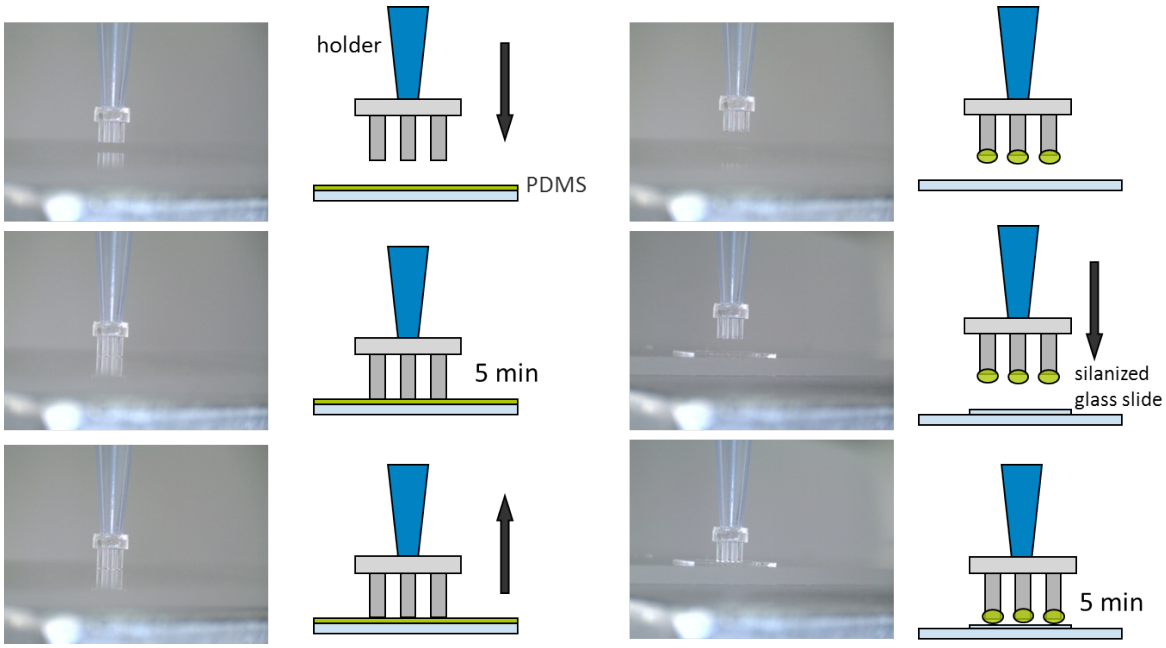

Figure 3.4: *Real pictures and schematic overview of the dipping process.*

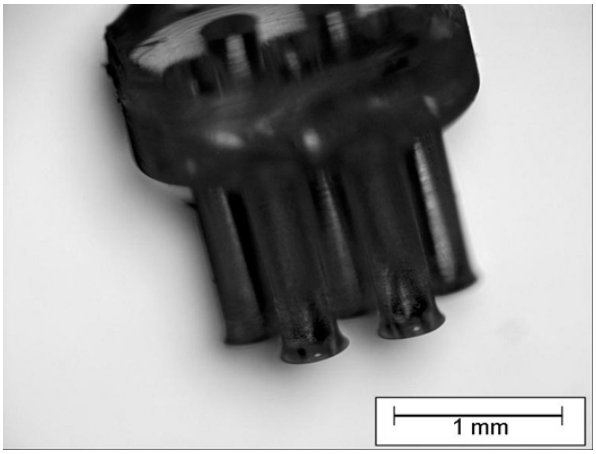

Figure 3.5: *Optical micrograph of mushroom shaped tips of size 1 pillars after the dipping process.*

3.1.5 Adhesion and buckling measurements[2]

Adhesion measurements were performed on a test apparatus, called Macroscopic Adhesion Measurement Device (MAD) [46], presented in Figure 3.6.

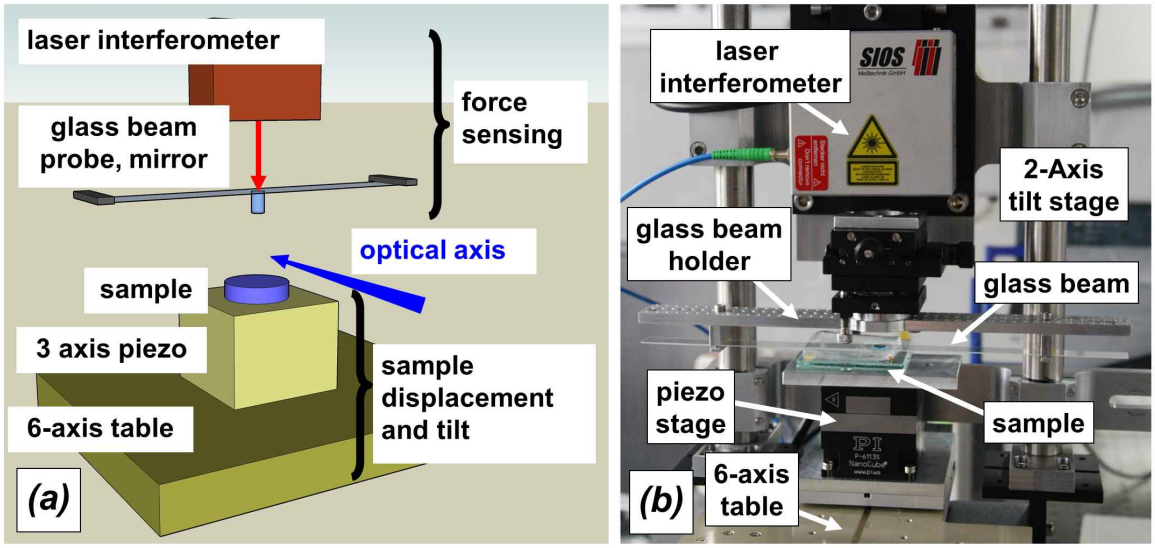

Figure 3.6: *Macroscopic Adhesion Measurement Device [46].*

The samples were fixed on a glass slide and placed on a positioning stage. The machined aluminum substrates had a surface finish of 0.4–0.5 µm (RMS, root-mean-square) and 200–250 µm (RSm, average groove spacing), measured by white light interferometry. In contrast the

[2]This subsection is content of C. T. Bauer, E. Kroner, N. A. Fleck, and E. Arzt, Hierarchical macroscopic fibrillar adhesives: In-situ study of buckling and adhesion mechanisms on wavy substrates, *Bioinspiration Biomimetics*, 2015 [2], but does not contain Figure 3.6 and the last paragraph.

borosilicate glass substrate had a surface finish of 0.01 µm (RMS) and 10 µm (RSm). The roughness was measured by a profilometer. The wavy rough substrates had the following surface topography:

- sinusoidal: wavelength of 4 mm and a peak-peak height of 200 µm, see Figure 3.7a and b.
- truncated sinusoidal: wavelength of 2 mm and a peak-peak height of 200 µm, but with flattened tops of width 1 mm, see Figure 3.7c and d.

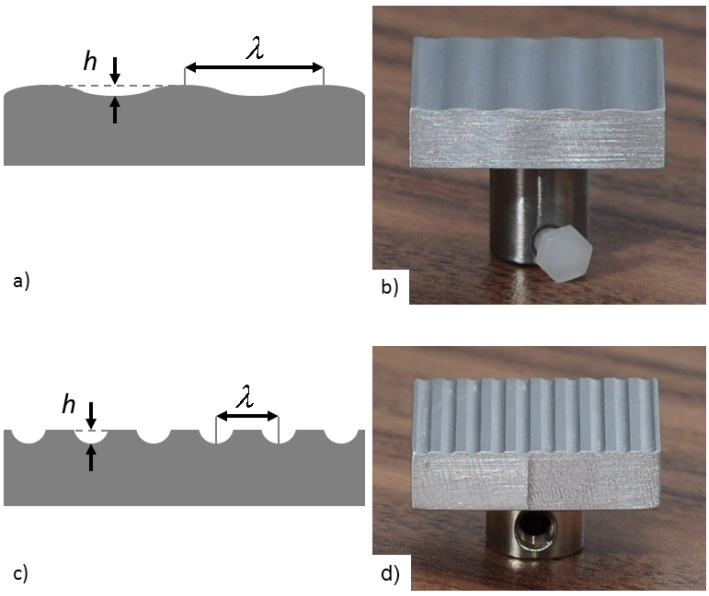

Figure 3.7: *Substrate surfaces with wavy contours for adhesion testing. a) Schematic and b) photograph of the sinusoidal aluminum substrate (λ = 4 mm,* h *= 200 µm), c) schematic and d) photograph of the truncated sinusoidal aluminum substrate (λ = 2 mm,* h *= 200 µm).*

The waviness of the substrates represents macroroughness. Force sensing was realized by a combination of a spring and a laser interferometer. A mirror was attached to the spring, which reflected the laser beam, thus allowing the determination of the spring deflection. The spring constant was determined by calibration with a load cell, and was found to be 2525 N/m. For all measurements a video of the sample deformation was recorded in side view. In addition to adhesion, the compressive buckling preload was measured. It was found that adhesion was limited by the onset of buckling under the preload. Adhesion and buckling measurements were performed on all level combinations (HL1, HL2 and HL3), with and without mushroom shaped tips. The measurements were performed by moving the sample towards the substrate, applying a predefined preload P, and retracting again until pull-off occurred. The measurements with

the flat sample were carried out using glass and aluminum substrates and were repeated three times for each substrate. To determine the pull-off force, F, 15 measurements were performed for each measurement set. Adhesion measurements on the flat rough substrate were performed on the flat part of the truncated sinusoidal aluminum substrate with single pillars to ensure that the probes had the same microroughness. The pull-off forces were multiplied by 7 for comparison with the other measurements. Adhesion measurements on the two rough substrates were performed at different positions with respect to the wavelength of roughness. This was achieved by changing the position along the wavelength in 0.2 mm steps. Scanning one wavelength of the wavy substrate resulted in 21 measurements for the sinusoidal substrate, and 11 measurements for the truncated sinusoidal substrate for each scan. Prior to all measurements, repeated contacts ensured that the substrate had a stable configuration [132] and was well aligned [133]. The correct alignment was checked with an optical camera setup. In all tests of type HL1, HL2 and HL3, the substrate surface was in contact with a single set of 7 pillars of size 1, and the measured force is the total force on all 7 pillars (with the exception of additional single pillar measurements as detailed below). For tests on HL2, the loaded set of 7 pillars of size 1 was placed on a central pillar of size 2. For tests on HL3, the loaded set of 7 pillars of size 1 was placed on the central pillar of a hexagonal arrangement of 7 pillars of size 2 and in turn the 7 pillars of size 2 were bonded to a central pillar of size 3. The error bars in all graphs represent the standard deviation about the arithmetic mean value.

The adhesion of softmolded particle structures (see Subsection 3.2.5) was measured with a borosilicate glass sphere with a diameter of 4 mm. Spherical substrates were independent of misalignment angle [133] and facilitated the measurements with small sample structures. The preload curves were measured and the saturation value of the pull-off forces was determined. This was necessary because in general the contact area of a spherical probe varies with preload and the adhesion values depend on the contact area. Measurements on three different spots were conducted with the prior determined preload force. On each spot a total number of 15 measurements were carriet out.[3]

[3]This paragraph is not content of C. T. Bauer, E. Kroner, N. A. Fleck, and E. Arzt, Hierarchical macroscopic fibrillar adhesives: In-situ study of buckling and adhesion mechanisms on wavy substrates, *Bioinspiration Biomimetics*, 2015 [2].

3.1.6 Overview of experiments with macroscopic pillar structures

The following figure gives an overview of the experiments with the macroscopic pillars. The individual steps of the scheme were explained in the subsections before.

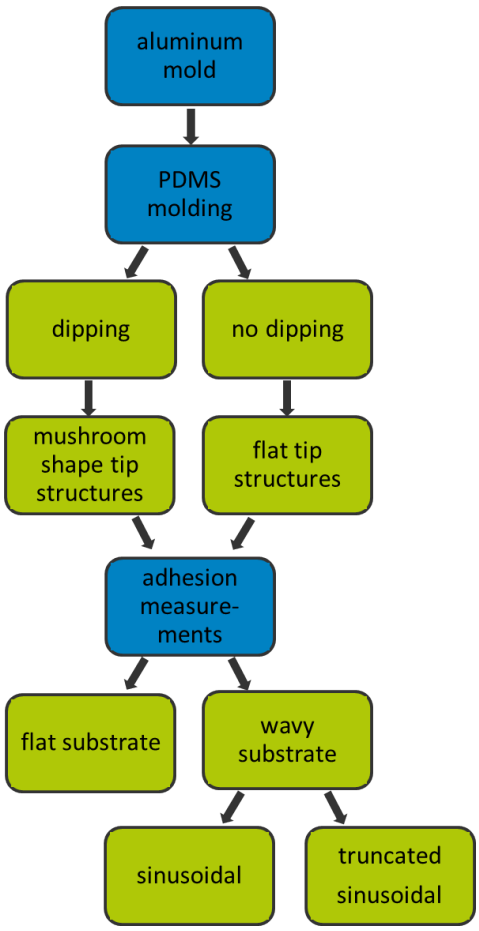

Figure 3.8: *General realization of experiments with macroscopic pillar structures.*

3.2 Fabrication of particle monolayers, plasma-etching and particle-based softmolding

Within a project funded by the German Science Foundation (DFG) within the framework of SPP1420 ('Biomimetic Materials Research: Functionality by Hierarchical Structuring of Materials') the second topic focussed on new fabrication methods which allow larger scale fabrication of micropatterned surfaces and at the same time can be combined with current state of the art patterning methods.

3.2.1 Preparation of close-packed monolayers

As substrates for the particles, silicon wafers with <100> crystallographic orientation (Asahi Kasei, Tokio, Japan) or silicon wafers with a PS layer (see Subsection 3.2.3) were used. Four different sizes of monodispersed PS particles were used: diameter 0.25 µm (*Polystyrene solids*, Bangs Laboratories, USA), 0.5, 1 and 3 µm (*carboxyl latex* 4 % w/v, Invitrogen, Darmstadt, Germany) were used. The silicon substrates were cleaned with isopropanol (*Normapur*®, purity 99.7 %) and treated with oxygen plasma (50 W, 5 min, *PICO Variante E*, Diener Electronic, Ebhausen, Germany) to clean and to hydrophilize the surface for a better wettability by the particle suspension to the substrate. The particles were deposited on a substrate with the Convection Assisted Particle Assembly (CAPA) setup [115], which is presented in Figure 3.9.

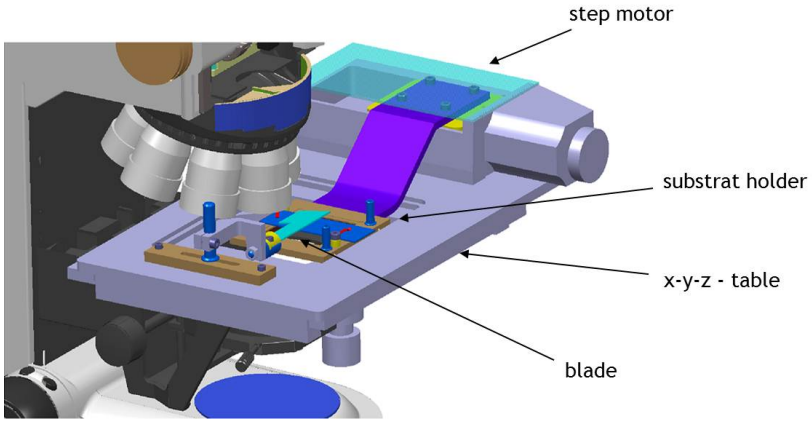

Figure 3.9: *Schematic of the Convection Assisted Particle Assembly (CAPA) tool [134].*

The substrate lies on a substrate holder/x-y-z-table, which can be moved by a step motor (*Precision Linear Stage PLS-85*, miCos GmbH, Eschenbach, Germany) against a blade. A suspension reservoir that is positioned between glass slide and substrate leaves a thin wetting film upon displacement. By the evaporation process, which induces convection in the wet particle suspension layer, a particle film forms (schematically shown in Figure 3.10). To get a dense particle monolayer on the substrate, the distance between blade and substrate, the supension mixing ratio, the temperature and the pulling velocity play an important role. The setup is mounted on the stage of an optical microscope (*Axio Imager A1m*, Zeiss, Oberkochen, Germany), which allows to observe the deposition process in-situ and allows precise control over the thickness of the film. With the CAPA setup the goal was to produce two-dimensional close-packed particle monolayers.

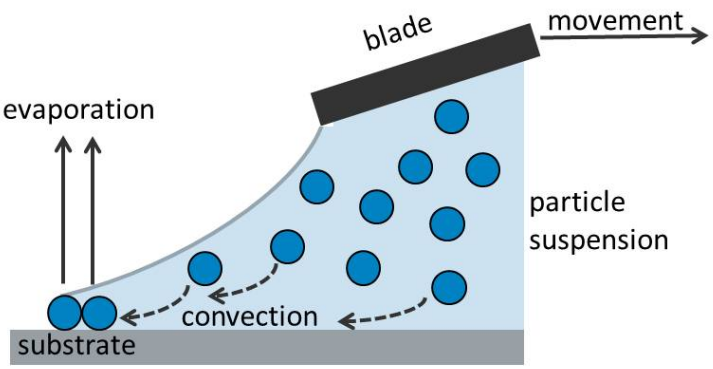

Figure 3.10: *CAPA mechanism.*

3.2.2 Preparation of nonclose-packed monolayers

To obtain nonclose-packed monolayers for reference measurements a small amount of the particle suspension reservoir (see Section 3.2.1) was diluted by ultrapure water (ca. 1:10) and dropped on a silicon wafer, followed by drying. The CAPA setup was not used.

3.2.3 Fabrication of a PS layer on silicon

To enhance the connection between substrate and PS particles, during the annealing, a PS layer was deposited on the silicon substrate. To produce a thin PS layer on the silicon wafer, polystyrene was dissolved in toluene (mass fraction of the solved component $w = 0.028$). The resulting solution was used for spin-coating. The solution was spread in the middle of a silicon wafer, and spin-coated (*CT62 Virgin*, Süss MicroTec AG, Garching, Germany) at 3500 rpm for 15 s. With this settings the thickness of the PS layer was $178\,\text{nm} \pm 8\,\text{nm}$. The coating thickness was determined by ellipsometry (*M-2000DI Ellipsometer*, J. A. Woolam Co., Inc., Lincoln, Nebraska, USA).

3.2.4 Annealing and plasma-induced size reduction

Before the particles on the substrate were treated with plasma it was very important to fix the particles to the substrate, otherwise the ion bombardment in the plasma process could knock the particles away from their position. Therefore the particles were annealed to the substrate in an oven (*Haraeus Vakuum Wärme- und Trockenschrank*, Thermo Fisher Scientific, Waltham,

Massachusetts, USA) for 60 s at 110 °C. The 1 µm particles were annealed for 90 s to create strong particle-substrate junctions. The particles were etched in pure oxygen plasma (*PICO Variante E*, Electronic Diener, Ebhausen, Germany) with different power (10 W–80 W) and times (2 min–90 min) to change interparticle distances. An oxygen flow volume of 220 cm^3/min was used as plasma source. To investigate the influence of heat, reference measurements were carried out: The plasma chamber was vented at regular intervals to avoid temperatures over 30 °C in the setup, to reduce thermal effects.

3.2.5 Particle based softmolding

After positioning of the particles on the silicon substrate, the particles were treated with oxygen plasma (50 W, 1 min) to make the surface more hydrophylic. Afterwards the particles were molded with PDMS (preparation see in Subsection 3.1.1).
The particles on the polystyrene layer were annealed (110 °C, 10 min) and then treated subsequent with oxygen plasma (20 W, 10 min) to tune interparticle distances, before the molding process started. The PDMS was cured at 75 °C in the oven for at least 12 h. The PDMS structures were exposed in the solvent acetone for 24 h to solve the polystyrene. To enhance the cleaning effect of the solvent an ultrasonic bath was used for 15 min. Figure 3.11 presents the three different used particle based softmolding strategies and the expected appearance of the PDMS structures.

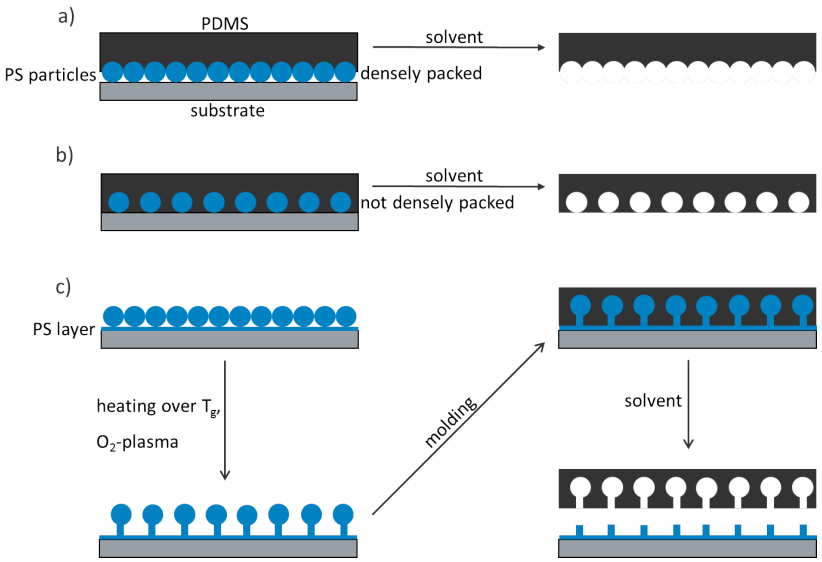

Figure 3.11: *Schematic of the three different used particle based softmolding strategies: a) molding of densely packed particles; b) molding of annealed and plasma etched particles and c) molding of annealed and plasma etched particles on a polystyrene layer.*

3.2.6 Overview of particle monolayer deposition, plasma etching and particle based softmolding

Figure 3.12 shows the general process of the realization of experiments with the PS (polystyrene) particles. The individual steps were described in the subsections before.

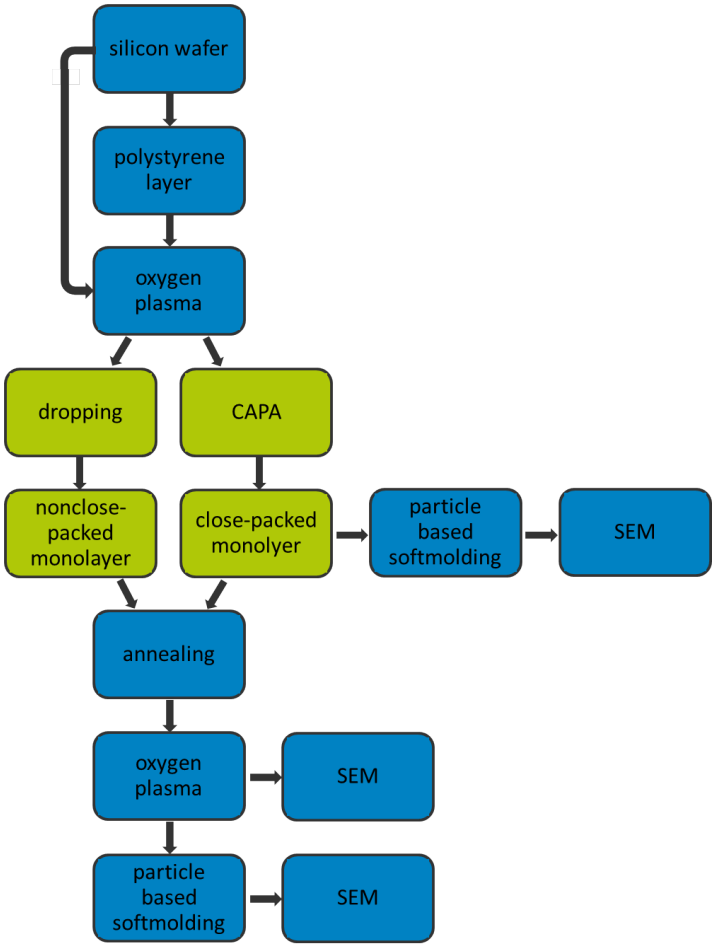

Figure 3.12: *General process of particle monolayer deposition, plasma etching and particle based softmolding.*

4 Hierarchical macroscopic fibrillar adhesives: In-situ study of buckling and adhesion mechanisms on wavy substrates[1]

4.1 Abstract

Nature uses hierarchical fibrillar structures to mediate temporary adhesion to arbitrary surfaces. Such structures are provide high compliance such that the flat fibril tips can be better positioned with respect to asperities of a wavy rough substrate. We investigated the buckling and adhesion of hierarchically structured adhesives in contact with smooth, flat rough and wavy rough substrates. A macroscopic model for the structural adhesive was fabricated by molding polydimethylsiloxane into pillars of diameter in the range 0.3 mm to 4.8 mm, with up to three different hierarchy levels. Both flat-ended and mushroom shaped hierarchical samples buckled at preloads one quarter that of the single level structures. We explain this behavior by a change in the buckling mode; buckling leads to a loss of contact and diminishes adhesion. Our results indicate that hierarchical structures can have a strong influence on the degree of adhesion on both flat and wavy surfaces. Strategies are discussed that achieve highly compliant surfaces which adhere to rough surfaces.

[1]This chapter was accepted for publication: C. T. Bauer, E. Kroner, N. A. Fleck, and E. Arzt, Hierarchical macroscopic fibrillar adhesives: In-situ study of buckling and adhesion mechanisms on wavy substrates, *Bioinspiration Biomimetics*, 2015 [2].

4.2 Introduction

Animals such as various species of insects, spiders and lizards, can adhere to different kinds of surfaces [13, 15, 135–138]. They have developed hairy attachment systems which enable them to stick to a wide range of substrate roughness. The gecko, for this purpose, possesses a hairy dry adhesion system with at least three levels of hierarchy [30, 139–141]: the toe pad surface consists of lamellae covered with setae, which branch into even finer spatulae. It has been suggested that geckos have adapted to generate much higher adhesive forces than is strictly necessary for flat smooth surfaces: this redundancy in adhesion allows them to adhere to rough surfaces [41, 142–144].

Adhesion of patterned structures to rough surfaces has received comparatively little attention in the literature to date. Several research groups have developed artificial gecko-inspired adhesion surfaces [42, 50, 54, 55, 57, 145–149] or even hierarchical structures [44, 48, 89, 96, 97, 99, 150–153], but only few studies exist on bioinspired adhesion structures on rough surfaces [45, 143, 154, 155]; some papers address adhesion of an artificial hierarchical system to rough surfaces [156–162] and experiments with living geckos on engineered rough substrates has been made [163]. Furthermore simulation of artificial gecko array on rough surfaces has been conducted [164]. Several theoretical studies suggest that the introduction of structural hierarchy increases adhesion to rough surfaces [83, 84, 165], but experimental evidence is lacking.

The aim of the present study is to explore the role of structural hierarchy on adhesion to a micro- and macrorough substrate. We report experiments on hierarchically structured model adhesives, with millimeter-size ‘macroscopic’ pillars on flat and wavy surfaces. A macroscopic model allows the contact and deformation phenomena of the system to be observed [130, 166], thereby giving detailed insight into the interaction mechanisms. The results suggest that a hierarchical structuring of dry adhesives does not necessarily result in increased adhesion. Rather, a new design path for artificial fibrillar adhesives on rough surfaces can be derived.

4.3 Materials and methods

Adhesion experiments were performed on samples with different levels of structural hierarchy, i.e. one, two, and three levels of hierarchy. Further, the tips of the structures were modified to resemble two different geometries, i.e. flat tips and mushroom shaped tips. The samples were brought in contact with flat smooth, flat rough and wavy rough substrates in order to explore the sensitivity of adhesion to surface topography and structural hierarchy. Polydimethylsiloxane (PDMS, Sylgard 184 kit, Dow Corning MI, USA) was chosen for its properties in replication precision and handling. At the low testing velocities, PDMS is believed to have low viscoelasticity at room temperature; it is recognized that the presence of viscoelasticity strongly influences adhesion and would thereby complicate the interpretations of our experiments [167, 168].

4.3.1 Preparation of hierarchical macroscopic pillars

Hierarchical structures were made from self-similar cylindrical pillars, as shown in Figure 4.1. At each level of hierarchy, a set of 7 pillars was arranged in a hexagonal pattern with a central pillar, see Figure 4.1c. Each set was bonded to the top of a larger pillar at the next hierarchy level. This pattern was repeated on moving up the scale of dimension, such that there are 3 levels of hierarchy, with a linear scale factor of ca. 4 on moving from one size to the next. The smallest pillars, 'size 1', are of diameter $D = 0.3\,\mathrm{mm}$, the intermediate pillars, 'size 2', are of diameter 1.3 mm and the largest pillars, 'size 3', are of diameter 4.8 mm. The center-to-center spacing S of each pillar equals twice the pillar diameter. H is the height of the pillars, L the length of the backing layer, and B is the thickness of the backing layer. Table 4.1 summarizes the dimensions of the pillars in terms of the parameters, as defined in Figure 4.1, and presents the magnitude of the second moment of area I and Young's Moduli E, which were measured by beam deflection of each pillar under a transverse load. Typical errors of the sizes H_i, D_i, L_i and S_i can be assumed as 2–10 %. Samples were prepared with one hierarchy level (HL1), consisting of only size 1 pillars, two hierarchy levels (HL2) with size 1 and size 2 pillars, and three hierarchy levels (HL3) with size 1, size 2 and size 3 pillars. Figure 4.1 shows a HL3

sample as schematic (Figure 4.1a) and as photograph (Figure 4.1b).

Table 4.1: *Geometric parameters of the PDMS structures for different hierarchy sizes.*

parameter	size 1	size 2	size 3
H_i(mm)	1.2	4.9	19.5
D_i(mm)	0.3	1.2	4.8
L_i(mm)	2.1	8.4	33.6
B_i(mm)	≈ 0.8	≈ 2.5	≈ 7.0
S_i(mm)	0.6	2.4	9.6
I_i(m^4)	$4.0 \cdot 10^{-16}$	$1.0 \cdot 10^{-13}$	$2.6 \cdot 10^{-11}$
E_i(MPa)	2.4 ± 0.2	3.0 ± 0.5	2.6 ± 0.1

Samples were cast in PDMS using aluminum alloy molds, as reported previously [130, 131]. The PDMS material was prepared by mixing the pre-polymer and cross-linker in a 10:1 ratio. To remove air bubbles, the mixture was degassed in a desiccator. After pouring into the casting molds, the PDMS was fully cured in an oven for more than 12 hours at 75°C. Subsequently, the PDMS pillar structure was peeled from the mold and excess material was removed with a scalpel. The pillars of different size were bonded by a droplet of uncured PDMS, followed by a thermal cure. The above process steps produced PDMS samples with a Young's modulus $E = 2.4$ to 3.0 MPa as measured by tensile tests (method is explained in Subchapter 3.1.2). Single pillar size 1 structures were fabricated in the same manner as described before but after the demolding process the pillars around the middle pillar were cut so that only one pillar remained.

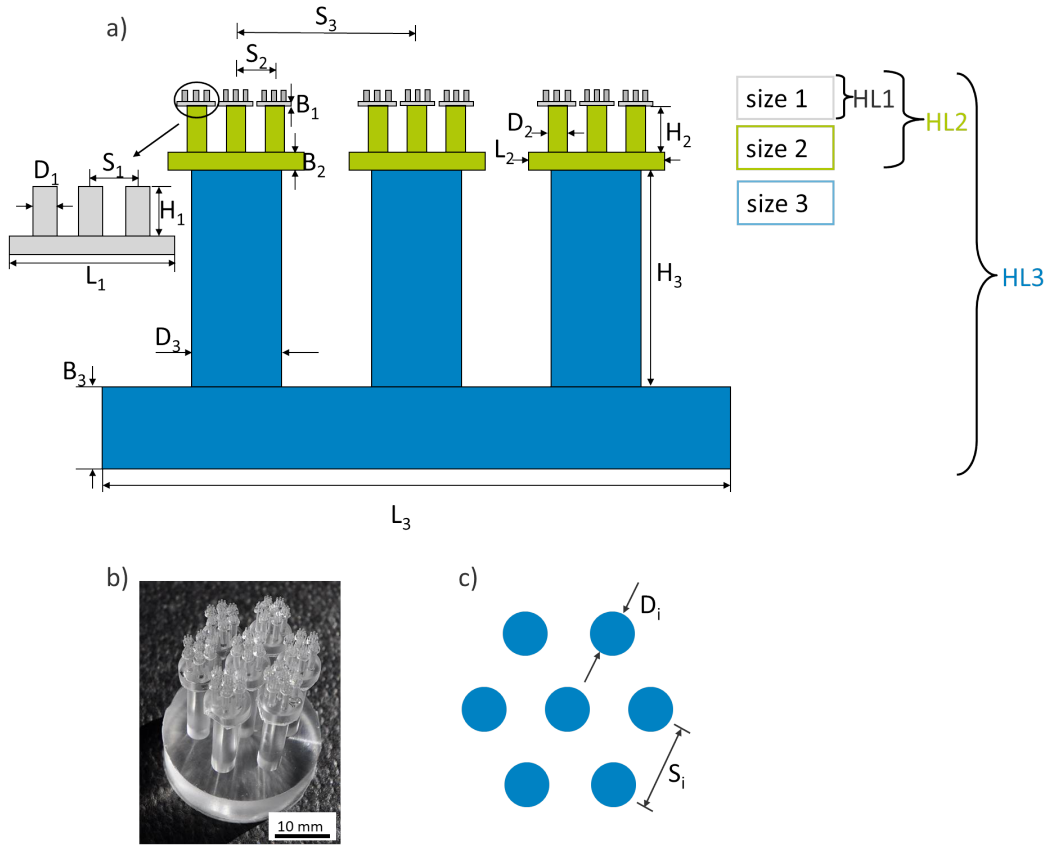

Figure 4.1: *Hierarchical array of the macroscopic pillars. a) Schematic overview of the hierarchical array; b) photograph of a sample with three hierarchical levels (HL3); c) end view of hexagonal arrangement of 7 pillars at each level of hierarchy.*

4.3.2 Preparation of mushroom tips on size 1 pillars

In all adhesion experiments the contact elements were the tips of the size 1 pillars, in either the as-cast flat end geometry or in a so-called 'mushroom' geometry. To achieve the mushroom geometry, the tips of size 1 pillars were modified using the following steps as previously established [57].

(i) A droplet of liquid PDMS was deposited onto each size 1 pillar by dipping the set of 7 pillars into a thin layer of uncured PDMS.
(ii) The droplets were deformed into a mushroom shape by pressing the pillars against a glass slide for a period of 12 hours at 75°C. The glass slides were pre-treated by placing a 50/50 mixture of perfluorodecyltriethoxysilane and hexane adjacent to the glass slides in a desiccator, until complete evaporation occurred under vacuum. The glass plates were maintained at 95°C for 30 minutes to stabilize the silanized surface. This allowed for easy removal of the cured PDMS from the glass.
(iii) After cure, the pillars were peeled from the glass slides.

Figure 4.2 shows a schematic of a mushroom shaped tip. The geometry of the tips was determined by optical microscopy and the following sizes, as described in Figure 4.2, were found: height $H \approx 75\,\mu m$, width $W \approx 40\,\mu m$, angle $\alpha \approx 50\,^\circ$ and tip radius $\rho \approx 20\,\mu m$.

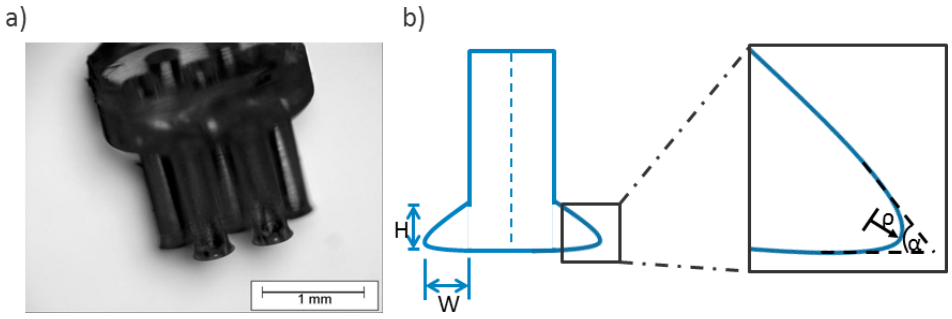

Figure 4.2: *a) Optical micrograph of mushroom shaped tips of size 1 pillars after the dipping process, b) schematic of a mushroom shaped tip with the geometry parameters height* H*, width* W*, the angle* α *of the mushroom cap and tip radius* ρ (not drwan to scale).

4.3.3 Adhesion and buckling measurements

Adhesion measurements were performed on a test apparatus, called Macroscopic Adhesion Measurement Device (MAD) [46]. The samples were fixed on a glass slide and placed on a positioning stage. A flat substrate of borosilicate glass and two aluminum substrates with wavy surfaces were used as substrate surfaces. The machined aluminum substrates had a surface finish of 0.4–0.5 µm (root-mean-square) and 200–250 µm (RSm), measured by white light interferometry. In contrast the borosilicate glass substrate had a surface finish of 0.01 µm (root-mean-square) and 10 µm (RSm). The roughness was measured by a profilometer. The wavy rough substrates had the following surface topography:

- sinusoidal: wavelength of 4 mm and a peak-peak height of 200 µm, see Figure 4.3a and b.
- truncated sinusoidal: wavelength of 2 mm and a peak-peak height of 200 µm, but with flattened tops of width 1 mm, see Figure 4.3c and d.

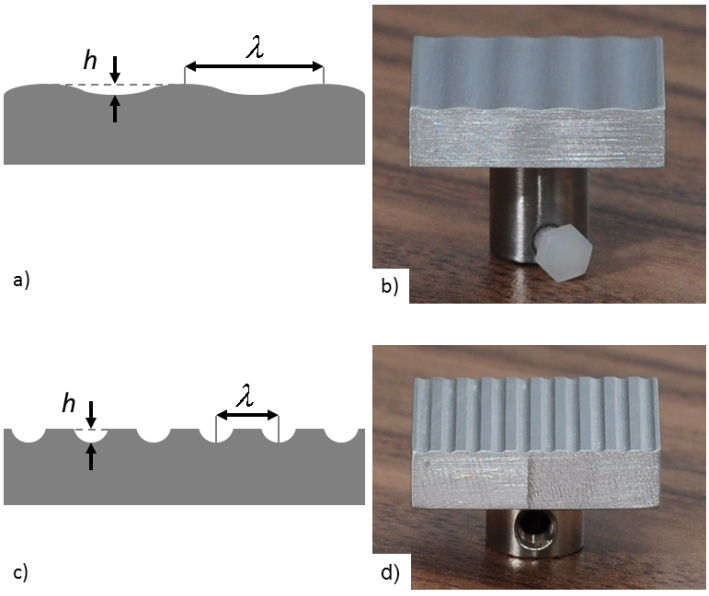

Figure 4.3: *Substrate surfaces with wavy contours for adhesion testing. a) Schematic and b) photograph of the sinusoidal aluminum substrate ($\lambda = 4\,mm$, $h = 200\,\mu m$), c) schematic and d) photograph of the truncated sinusoidal aluminum substrate ($\lambda = 2\,mm$, $h = 200\,\mu m$).*

The waviness of the substrates represents macroroughness. Force sensing was realized by a combination of a spring and a laser interferometer. A mirror was attached to the spring, which reflected the laser beam, thus allowing the determination of the spring deflection. The spring constant was determined by calibration with a load cell, and was found to be 2525 N/m. For all measurements a video of the sample deformation was recorded in side view.

In addition to adhesion, the compressive buckling preload was measured. It was found that adhesion was limited by the onset of buckling under the preload. Adhesion and buckling measurements were performed on all level combinations (HL1, HL2 and HL3), with and without mushroom shaped tips. The measurements were performed by moving the sample towards the substrate, applying a predefined preload P, and retracting again until pull-off occurred. The measurements with the flat sample were carried out using glass and aluminum substrates and were repeated three times for each substrate. To determine the pull-off force, F, 15 measurements were performed for each measurement set. Adhesion measurements on the flat rough substrate were performed on the flat part of the truncated sinusoidal aluminum substrate with single pillars to ensure that the probes had the same microroughness. The pull-off forces were multiplied by 7 for comparison with the other measurements. Adhesion measurements on the two rough substrates were performed at different positions with respect to the wavelength of roughness. This was achieved by changing the position along the wavelength in 0.2 mm steps. Scanning one wavelength of the wavy substrate resulted in 21 measurements for the sinusoidal substrate, and 11 measurements for the truncated sinusoidal substrate for each scan. Prior to all measurements, repeated contacts ensured that the substrate had a stable configuration [132] and was well aligned [133]. The correct alignment was checked with an optical camera setup. In all tests of type HL1, HL2 and HL3, the substrate surface was in contact with a single set of 7 pillars of size 1, and the measured force is the total force on all 7 pillars (with the exception of additional single pillar measurements as detailed below). For tests on HL2, the loaded set of 7 pillars of size 1 was placed on a central pillar of size 2. For tests on HL3, the loaded set of 7 pillars of size 1 was placed on the central pillar of a hexagonal arrangement of 7 pillars of size 2 and in turn the 7 pillars of size 2 were bonded to a central pillar of size 3. The error bars in all graphs represent the standard deviation about the arithmetic mean value.

4.4 Results

4.4.1 Adhesion experiments using a flat substrate

Representative force-displacement curves for the total force on 7 pillars of a HL1 sample with mushroom shaped tips are given in Figure 4.4a. The peak positive force is defined as compressive preload P, whereas the peak negative force is defined as the pull-off force F, as shown in Figure 4.4a.

When the preload is sufficiently high, buckling occurs at $P = P_B$, as shown in the rightmost plot of Figure 4.4a. The dependence of F upon P is given in Figure 4.4b; three regimes can be identified. Representative plots of force versus displacement for each regime are shown in Figure 4.4a, and each regime is now described in turn.

Regime I ($P \ll P_B$): For $0\,\mathrm{mN} < \mathrm{P} < 30\,\mathrm{mN}$ F increases steeply with increasing P due to contact formation. A low preload $\mathrm{P} \approx 30\,\mathrm{mN}$ is required to form contact between all pillar tips and the substrate. A force-displacement curve in this regime shows a small compressive (preload P) and a low tensile value (pull-off force F).

Regime II ($P < P_B$): F increases slightly with increasing P for $30\,\mathrm{mN} < \mathrm{P} < 330\,\mathrm{mN}$. This is ascribed to the fact that microscopic asperities on the contacting tip are flattened by increasing P. A force-displacement curve in this regime shows higher compression and higher tension compared to Regime I.

Regime III ($P = P_B$): The pillars buckle elastically at a critical preload $P_B \approx 340\,\mathrm{mN}$. Then the preload P saturates at $P = P_B$ and the pull-off force F decreases with increasing displacement in the post-buckling regime. The peak pull-off force F_{max} occurs at the onset of elastic buckling at $P = P_B$, as shown in Figure 4.4b.

Representative snapshots of the buckling mode for HL1, HL2 and HL3 sample are shown in Figures 4.5 a, b, and c, respectively. In the case of HL2 and HL3, the pillars of size 2 and 3 buckled in the opposite direction to that of the pillars of size 1.

The buckling preload P_B for the three levels of hierarchy and for the two types of tip shapes against a flat substrate is shown in Figure 4.6a. Note that the buckling preload P_B of a single hierarchy level HL1 is about 4 times that for hierarchy levels HL2 and HL3. The buckling

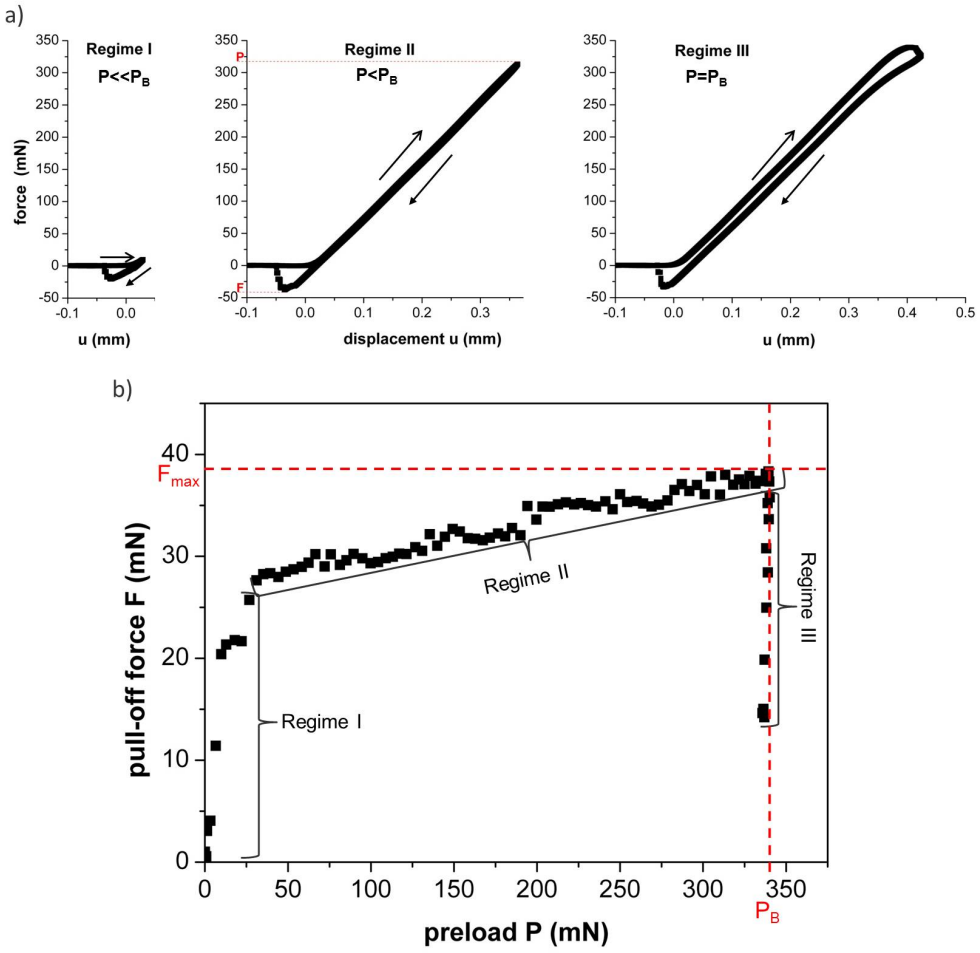

Figure 4.4: *a) Force-displacement curves of three different characteristic regimes for an HL1 sample with mushroom shaped tips on the flat glass substrate, measured on all 7 pillars. The sample approaches the substrate and forms contact (Regime I); with higher displacement the pull-off force F increases (Regime II) until a critical preload P is reached (Regime III). The pull-off force* F *decreases with increasing displacement. The peak load is determined as the buckling preload* P_B*. b) The pull-off force* F *as a function of preload* P *is given for an HL1 sample with mushroom shaped tips on the flat glass substrate, measured on all 7 pillars. The pull-off force* F *increases with increasing preload, until a critical preload* P_B *is reached. Above the critical preload* P_B*, further sample compression does not lead to an increase in preload* P *but to a collapse of the structures and subsequently to a drop in pull-off force* F*.*

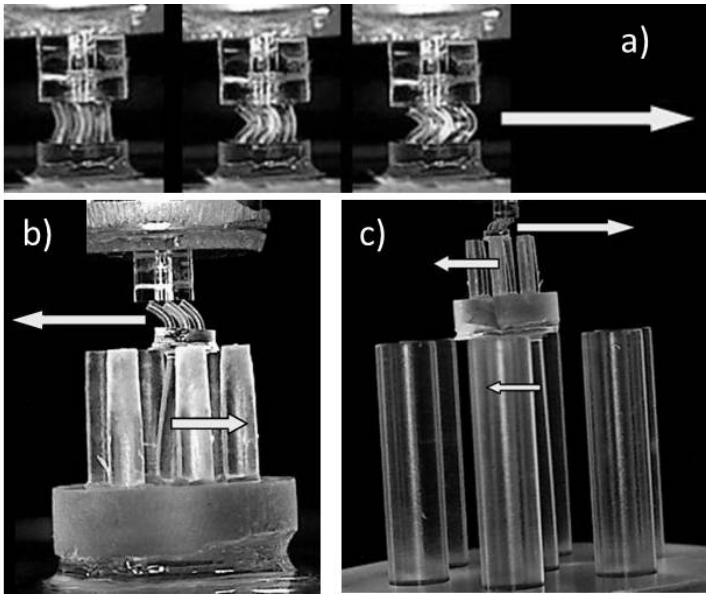

Figure 4.5: *Buckling mode as a function of hierarchy level for a) HL1, b) HL2 and c) HL3, measured against a flat substrate. The arrows indicate the direction in which the pillars deflect.*

preload P_B has comparable values for both flat and mushroom tip structures: the presence of the mushroom tip has a negligible effect upon the value of P, and upon the buckling mode.

Figure 4.6b shows the maximum pull-off forces F_{max} upon reaching the critical buckling preload. Here, the single-level structure HL1 displays a slightly higher pull-off force F_{max} than the hierarchical structures HL2 and HL3. The mushroom shaped tip structures showed an enhancement in pull-off force F_{max} by up to a factor of 3 to 30 compared to the flat tips.

The corresponding adhesive strength ('apparent' and 'actual') values are presented in Table 4.2. For the calculations of the 'apparent' adhesive strength, the apparent contact area was chosen as $({L_1}^2\pi/4) = 3.46$ mm^2 (see also Figure 4.1 and Table 4.1). For the calculations of the 'actual' adhesive strength, the contact area was chosen for structures without mushroom as $7((D_1)^2\pi/4) = 0.49\,\text{mm}^2$ and for structures with mushroom as $7((D_1 + 2W)^2\pi/4)$ (see also Figure 4.1, Table 4.1 and Figure 4.2).

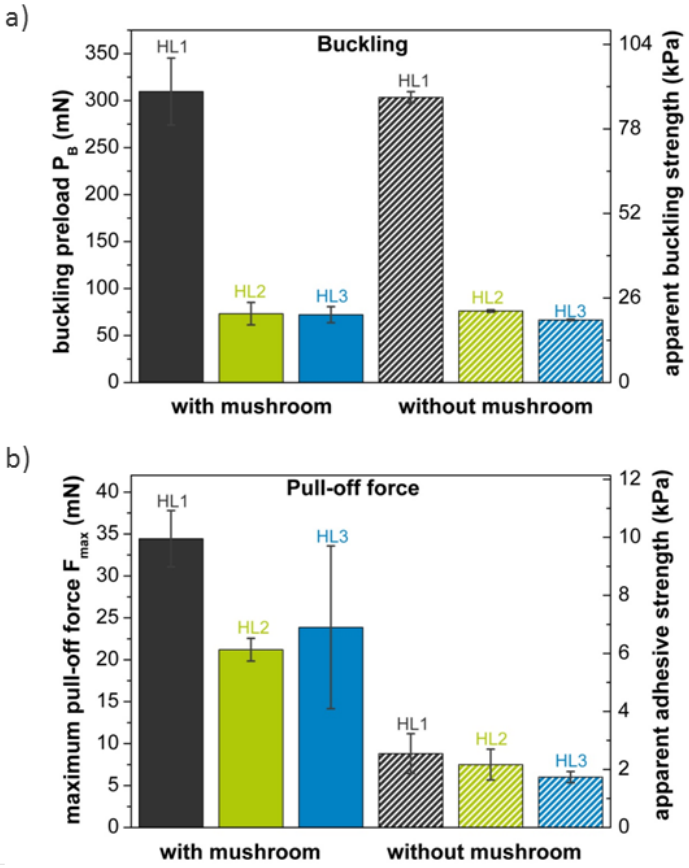

Figure 4.6: *Critical preload* P_B *and pull-off forces* F_{max}*, as well as the corresponding 'apparent' strength values, measured on all 7 pillars of size 1: a) Buckling preloads* P_B *for different specimens measured against the flat glass substrate: HL1, HL2 and HL3 structures, with and without mushrooms. b) Pull-off force* F_{max} *for HL1, HL2 and HL3 structures with and without mushrooms measured against the same substrate.*

Table 4.2: *Adhesive strength values of HL1, HL2 and HL3 structures with and without mushrooms measured against a flat glass substrate.*

structure	'apparent' adhesive strength (kPa)	'actual' adhesive strength (kPa)
HL1/m	9.94 ± 0.97	43.58 ± 4.25
HL2/m	6.12 ± 0.39	26.84 ± 1.72
HL3/m	6.89 ± 2.80	30.20 ± 12.29
HL1	2.54 ± 0.68	17.97 ± 4.84
HL2	2.17 ± 0.53	15.30 ± 3.75
HL3	0.23 ± 0.31	12.25 ± 1.36

4.4.2 Adhesion experiments using a flat rough substrate

The buckling preload P_B for the three levels of hierarchy against a flat rough aluminum substrate and flat smooth glass substrate is shown in 4.7a. The buckling preload of a single hierarchy level HL1 is again about 4 times higher than for hierarchy levels HL2 and HL3. It is seen that the presence of microroughness has negligible effect on the buckling mode.

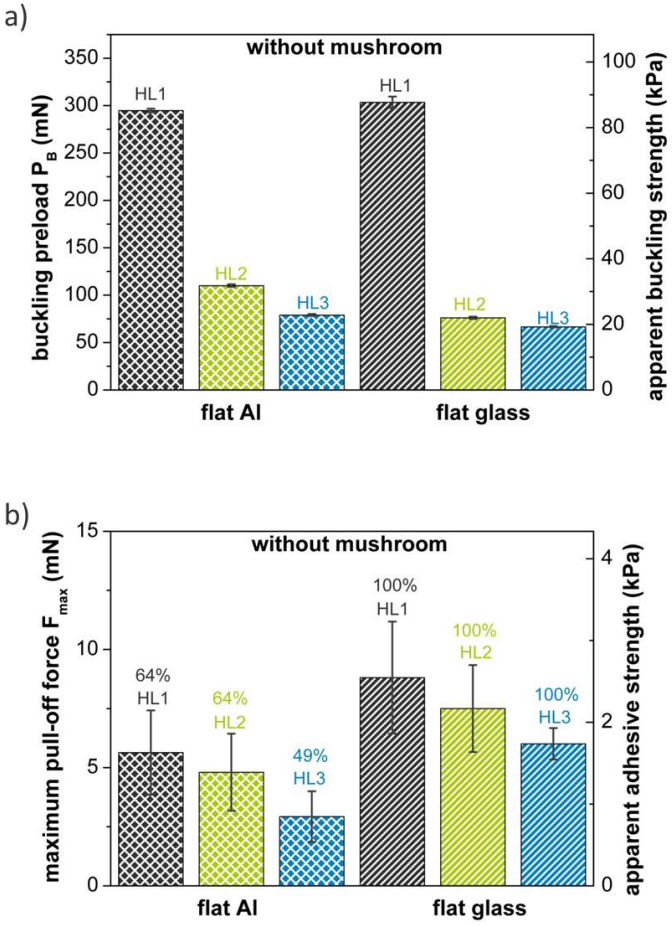

Figure 4.7: *a) Critical preload* $\mathrm{P_B}$ *and b) pull-off forces* $\mathrm{F_{max}}$*, as well as the corresponding 'apparent' strength values: Measurements on single pillar on flat aluminum and on all 7 pillars of size 1 on flat glass: HL1, HL2 and HL3 structures without mushrooms. The results from single pillar measurements were multiplied by 7 for comparison with the other measurements.*

Figure 4.7b shows the maximum pull-off forces F_{max} upon reaching the critical buckling preload. Here, the single-level structure HL1 displays a higher pull-off force F_{max} than the hierarchical structures HL2 and HL3. HL3 shows the lowest pull-off force F_{max}. The microroughness of

the flat rough aluminum substrate showed a decrease in pull-off force F_{max} by up to 35 to 50 % compared to the flat smooth glass substrate.

4.4.3 Adhesion experiments using wavy rough substrates

The hierarchical pillars were pressed against the sinusoidal substrate of wavelength $\lambda = 4\,\text{mm}$ until a buckling event (at least buckling of one HL1 pillar) occurred. Figure 4.8a shows the buckling load P_B for 7 pillars as a function of testing position y, as defined in Figure 4.8b. The schematic below the graph depicts the position of the contacting elements with respect to the wavy substrate; the dots indicate the center position of the center pillar of the hexagonal array. Figure 4.8b also shows the maximum pull-off force F_{max}.

The buckling preload values P_B differ significantly for the HL1, HL2 and HL3 samples, recall Figure 4.8a. Generally, the single-level structure HL1 exhibits the highest buckling loads, but there is also a large variation with position; these samples buckle at the lowest preload for the substrate positions $\lambda/4$ ($\text{y} = 1.0\,\text{mm}$) and $3\lambda/4$ ($\text{y} = 3.0\,\text{mm}$), where the highest slope of the substrate surface is found. Although the shapes of the curves for the HL2 and HL3 samples resemble that of the HL1 sample, the absolute values are lower. Mushroom shaped tips tend to have a slightly decreased buckling preload compared to the flat tip structures. In similar fashion, the largest values of F_{max} occur at $\text{y} = 2.0\,\text{mm} = \lambda/2$, at the peak of the sine wave. For the HL1, HL2 and HL3 samples, the F_{max} values are comparable, but lower than the adhesion forces obtained by flat substrate measurements. Mushroom shaped structures always show increased adhesion compared to the flat tip pillars.

Similar experiments were performed with a truncated substrate of wavelength 2 mm. The results are shown in Figure 4.9. Again, a significantly reduced buckling preload P_B is observed for structures with more than one level of hierarchy. The buckling preload curves are also symmetric. The values of F_{max} for the truncated sinusoidal substrate exceed the values in Figure 4.8 for the sinusoidal substrate.

The buckling preload P_B for the truncated sinusoidal substrate is highest at the positions λ ($\text{y} = 0\,\text{mm}$ and $\text{y} = 2.0\,\text{mm}$), i.e. in the valleys of the substrate. Minima in the buckling preload P_B were found at the intermediate positions of the maxima of the substrate, approximately at

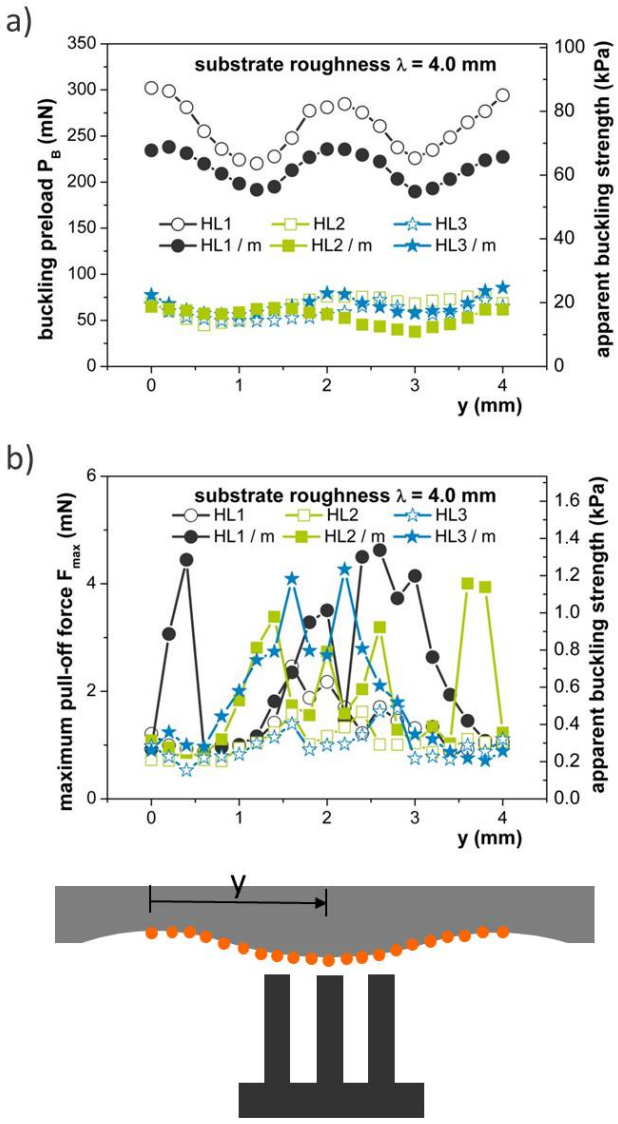

Figure 4.8: *Measurement results on samples with HL1, HL2 and HL3, both with flat tips and mushroom tips (indicated as 'm') measured on all 7 pillars of size 1. The forces were measured with a wavy substrate ($\lambda = 4\,mm$, $h = 200\,\mu m$) as a function of substrate position. a) Buckling preload* P_B *and b) maximum pull-off force* F_{max}*, with the corresponding 'apparent' strength values. The schematic below shows the testing position of the center pillar with respect to the wavy substrate (drawn with correct relative scale).*

positions $\lambda/4$ ($y = 0.5\,mm$) and $3\lambda/4$ ($y = 1.5\,mm$). At positions close to $\lambda/2$ ($y = 1.0\,mm$), the substrate is similar to a flat substrate and buckling is delayed to preload values P_B that are about a factor of about 30 to 40 % higher than in the lowest buckling positions.

For the maximum pull-off forces F_{max}, shown in Figure 4.9b, several trends were observed. The HL1 samples adhered better than both the HL2 and HL3 samples, which showed comparable pull-off forces. Again, the substrate symmetry is mirrored in the pull-off forces. The lowest forces were found at positions λ ($y = 0\,mm$ and $y = 2.0\,mm$). The maximum pull-off force F_{max} is almost independent of position for the flat tip HL2 and HL3 structures.

Again, mushroom shaped structures showed increased adhesion compared to the flat tip pillars with the same hierarchical structure, independent of the number of hierarchy levels or the testing position. Mushroom tips increased pull-off forces by a factor of 3 to 5. For a better interpretation of the measurements on a wavy substrate, additional measurements with size 1 single pillars will now be reported.

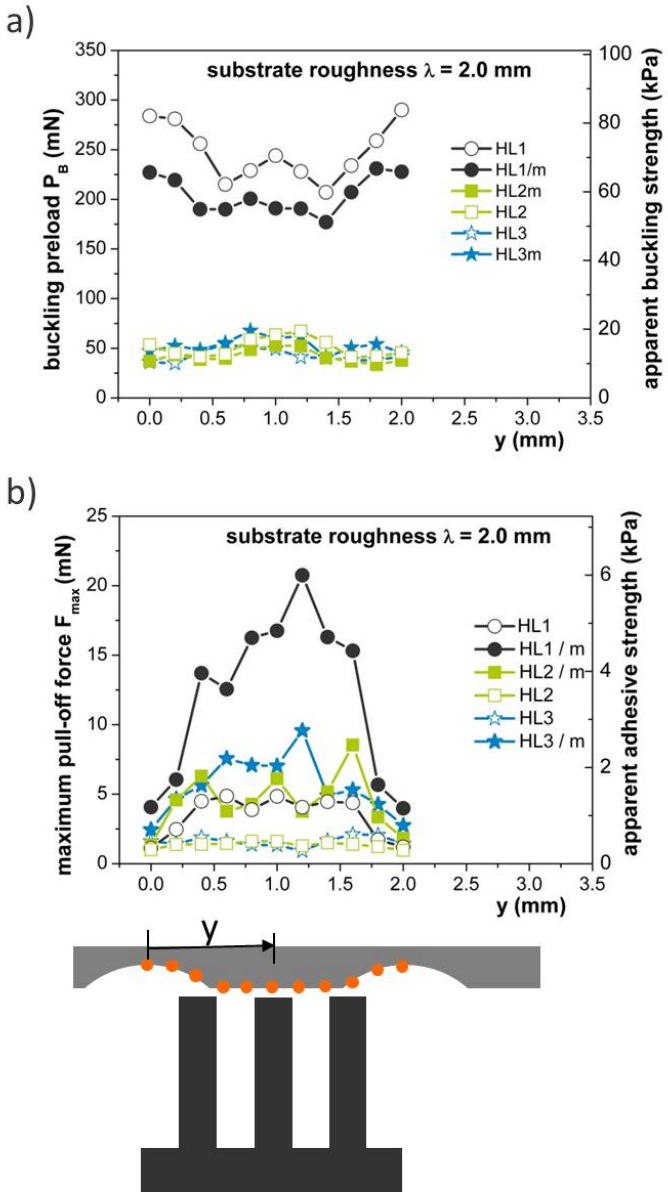

Figure 4.9: *Experiments similar to Figure 4.8 but with a truncated sinusoidal substrate. The x-axis shows the position of the sample with respect to the wavy substrate; a) Buckling force* $\mathrm{P_B}$*, and b) maximum pull-off force* $\mathrm{F_{max}}$*, with the corresponding 'apparent' strength values. Below, a schematic is given showing the wavy substrate and the testing position of size 1 structure.*

4.4.4 Size 1 single pillar measurements

In order to gain further insight into adhesion on a wavy substrate, additional single pillar buckling measurements were conducted. Figure 4.10 shows the measured buckling preload for:

(i) a single pillar (*sp,experiment*),
(ii) the theoretical buckling preload for a hexagonal pillar array by making use of single pillar measurement values (*hp,theory*); the definition is given in Figure 4.10.
(iii) the measured values for a hexagonal pattern consisting of 7 pillars (*hp,experiment*) and
(iv) the measured single pillar values (*sp,experiment*) multiplied by 7 (*7*(sp,experiment)*).

All values are presented for a sinusoidal punch of wavelength a) $\lambda = 4\,\text{mm}$, and b) $\lambda = 2\,\text{mm}$. In Figure 4.10a the *sp,experiment* values (and the *hp,experiment* results) show lowest values of P_B at $\lambda/4$ ($y = 1.0\,\text{mm}$) and at $3\lambda/4$ ($y = 3.0\,\text{mm}$). The measured values for the hierarchically assembled pillars are adequately approximated by multiplying the single pillar value by 7 (*7*(sp,experiment)*). The procedure was repeated for the truncated sinusoidal substrate ($\lambda = 2\,\text{mm}$, see Figure 4.10b). The *sp,experiment* values show the highest buckling load at the position of the flat part of the substrate as well as at λ ($y = 0\,\text{mm}$ and $y = 2\,\text{mm}$). Again, the 7*(*sp,experiment*) values agree reasonably well with the *hp,experiment* values.

Figure 4.11 presents the force-displacement curves of the single pillar (sp) at selected positions y on a wavy substrate ($\lambda = 4\,\text{mm}$) and includes curves for the *hp,theory* and for the *hp,experiment* curve. The individual pillars of an HL1 hexagonal pillar array do not make contact simultaneously during the experiment because of the waviness of the substrate. The differences in distance between the substrate and the sample are measured experimentally and considered in Figure 4.11 by an off-set in the displacement.

The applied preload P on each pillar decreases by 30–40 % after the buckling event, then increases again until the sample is retracted from the substrate. The hp_{sum} curve is the sum of the single pillar values for an assumed hexagonal pillar array with consideration of the off-set in the displacement. The hp_{sum} curve and the experimentally measured hp curve show a similar trend, with a buckling load P_B deviation of only 6 %.

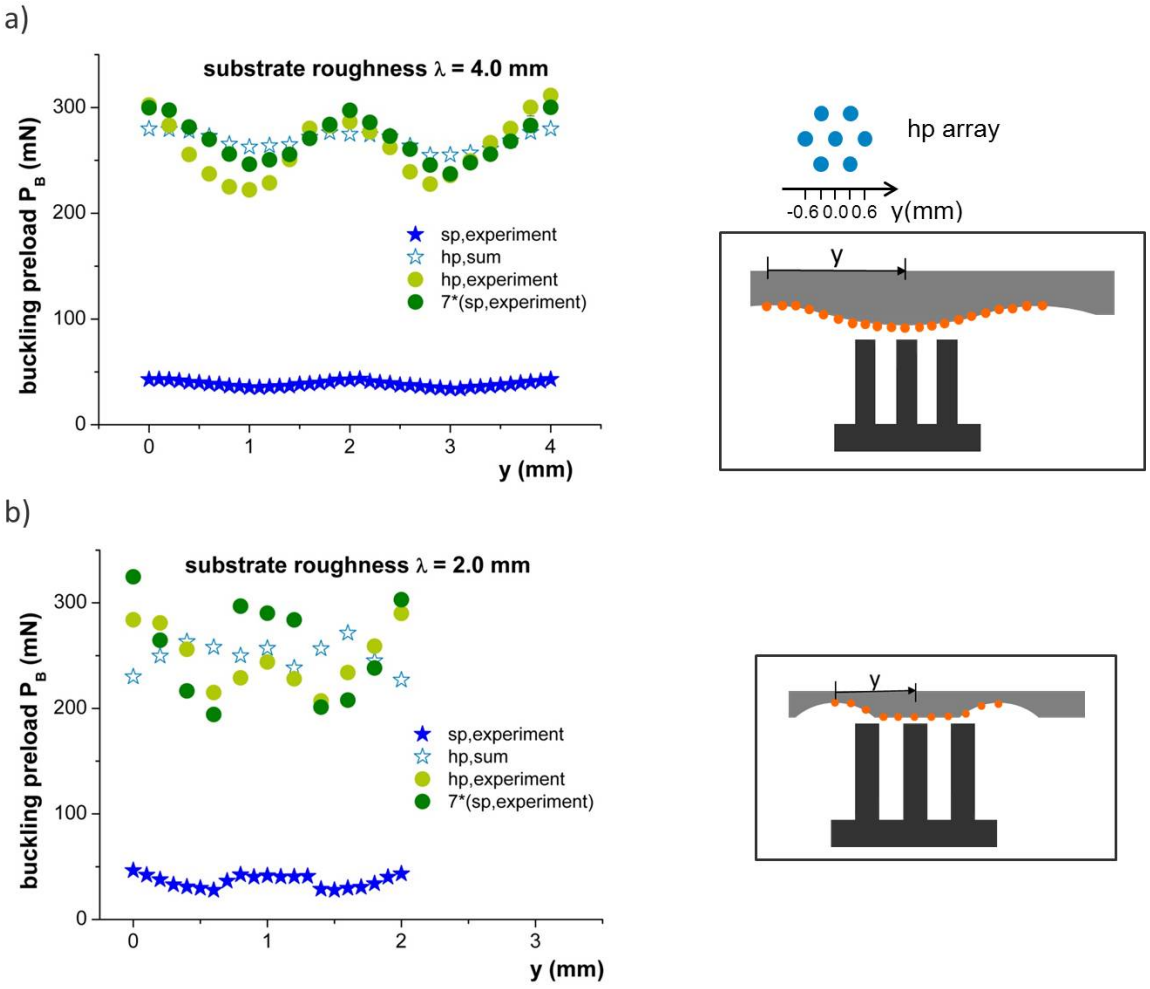

Figure 4.10: *Buckling preloads of a size 1 single pillar (sp) and of a size 1 hexagonal pillar (hp) array: a) sinusoidal substrate with $\lambda = 4.0\,mm$, and b) truncated sinusoidal substrate with $\lambda = 2.0\,mm$. The* 'hp,sum' *values are the sums of the single pillar measurements at the respective positions (see schematic insert).*

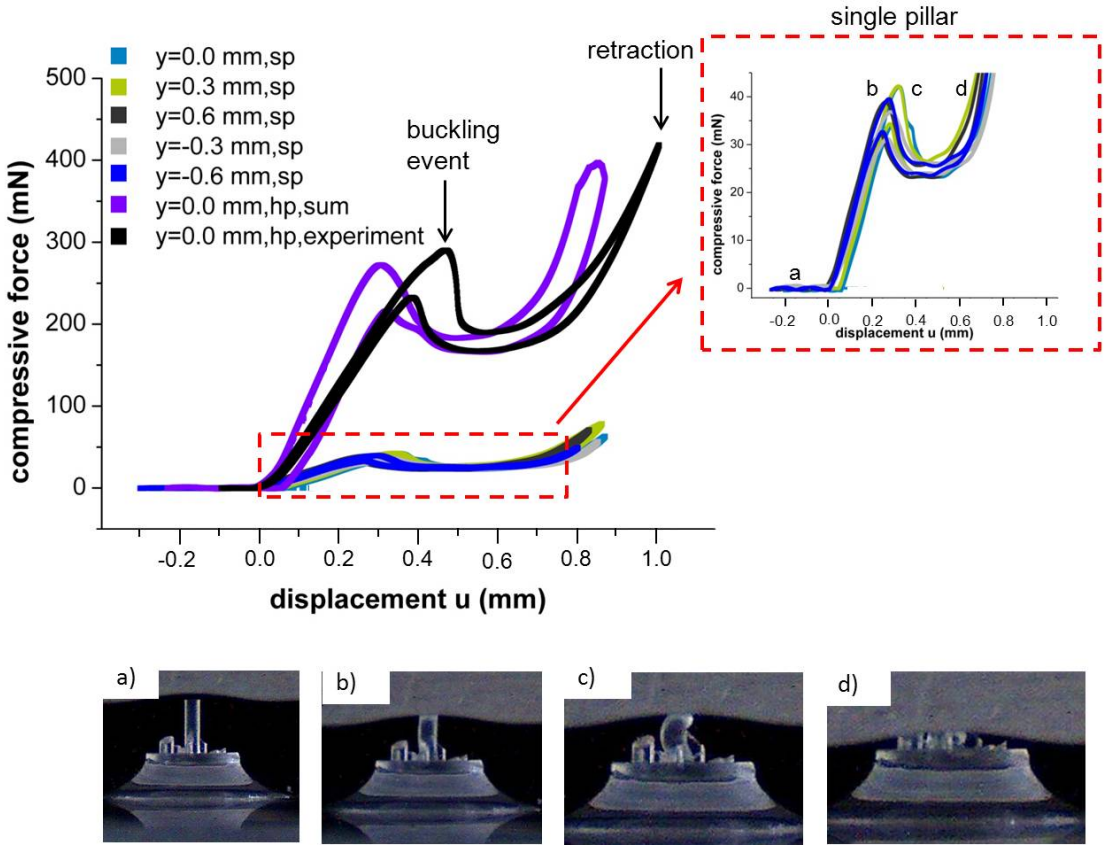

Figure 4.11: *HL1 force/displacement curves measured on a wavy substrate* ($\lambda = 4\,mm$, $h = 200\,\mu m$)*: a) uncompressed, b) just before buckling, c) buckled, d) strongly compressed for the case* $y = 0\,mm$*. The results of the first five measurement curves* ($y = 0.0$, *0.3, 0.6, -0.3, -0.6 mm*) *are based on size 1 single pillar* (sp) *measurement results. The* 'hp,sum' *data points are the sums of the single pillar measurement at the respective positions; The experimental data curve* 'hp,experiment' *is based on a real measurement with a hexagonal array of size 1 pillars.*

4.5 Discussion

4.5.1 Experiments on a flat substrate

The experiments on flat substrates have shown that the buckling behavior of the structures strongly depends on hierarchy. While non-hierarchical (HL1) structures have buckling loads of approx. 300 mN, the hierarchical samples show values of around 75 mN, a factor of 4 lower. This can be explained by the change in the buckling mode with structural hierarchy.

a) Estimation of the buckling load for a single size 1 pillar (H = 1.2 mm, D = 0.33 mm)

The Euler load P_E for a size 1 pillar is = 12 mN with the assumption of Young's modulus E = 3 MPa and second moment of area. In contrast, a pillar with one end hinged and the other fixed implies a buckling load of 2.04 P_E. Also, the pillar is stocky (aspect ratio = 4), hence Biot [102] finds an elevation in buckling load of 50 %. Thus, the predicted buckling load is 3.06 P_E or 37 mN. As the observed buckling load for a single pillar (no mushroom tip) is 43 mN, i.e. 17 % above the prediction, the agreement is adequate for our purposes.

b) Estimation of the buckling load for a hierarchical pair of pillars

Now consider the elastic buckling response of a pillar which has a stepwise jump in bending modulus along its length. The predicted ratio of buckling strength for HL1 and HL2 is 2.05/0.423 = 4.8, which again conforms well to the observed ratio of 3.9 to 4.9 (deviation of 2 to 19 %). The detailed estimation and derivation is summarized in the Supporting Information (see Section A1). The results presented in Figure 4.6b show that there is a notable difference in adhesion (maximum pull-off force) between flat tip structures and structures with mushroom shaped tips, as expected from earlier studies [57, 169, 170]. For adhesion against flat surfaces, the effect of tip shape dominates over the effect of hierarchy. Interestingly, the mushroom shaped structures show buckling load values similar to flat tip structures. This is in contrast to the experiments performed by Paretkar et al. [101, 171], who found that mushroom tips can delay buckling. This discrepancy may be ascribed to different mushroom tip geometry, which is more difficult to control in the fabrication process for the microscopic structures.

An important outcome of the present work is that hierarchical structures tend to show lower adhesion compared to single level samples if tested against a flat substrate. A possible

explanation is that the hierarchical samples require a higher preload to fully adapt to the substrate, e.g. adaptation to micro- and nanoroughness. However, a high preload cannot be achieved due to buckling, which would lead to a loss in tip contact and thus a loss in adhesion. It can be concluded that the introduction of a hierarchy is not necessarily beneficial: it will not increase adhesion against smooth, flat surfaces, but may even reduce it due to the buckling at lower preload for hierarchical structures.

4.5.2 Experiments on a flat rough substrate

To investigate the influence of microroughness on adhesion, measurements on a flat rough aluminum substrate were made. The adhesion decreased by 35 to 50 % in comparison to measurements on a flat smooth glass substrate for HL1, HL2 and HL3. This supports the assumption that microroughness decreases adhesion [33]. Fuller and Tabor [33] correlated the decrease of adhesion with an 'adhesion parameter' $1/\Delta c$

$$\frac{1}{\Delta c} = \left(\frac{4\psi}{3}\right)\left[\frac{4E}{3\pi\beta^{\frac{1}{2}}\Delta\gamma}\right]^{\frac{2}{3}} \tag{4.1}$$

where ψ is the root-mean-square roughness, E the Young's modulus, β the radius of curvature of asperity and $\Delta\gamma$ the surface energy ($0.02\,\mathrm{J/m^2}$). The radius of curvature of asperity β of the substrate can be calculated as

$$\beta = \frac{\Theta^2}{4\pi^2\psi} \tag{4.2}$$

where Θ is the RSm roughness of the substrate, i. e. the average groove spacing of the roughness. In Figure 4.12 the relative pull-off force is plotted as a function of the adhesion parameter. The adhesion parameters for flat smooth glass and flat rough aluminum substrate were calculated: $1/\Delta c_{glass} = 0.029$ and $1/\Delta c_{Al} = 0.656$. This means that for the flat glass substrate no relevant adhesion decrease is expected in contrast to the rough aluminum substrate,

for which a decrease of about 32 % is predicted. Our results of 35 % for HL1 and HL2 is in good agreement with this value.

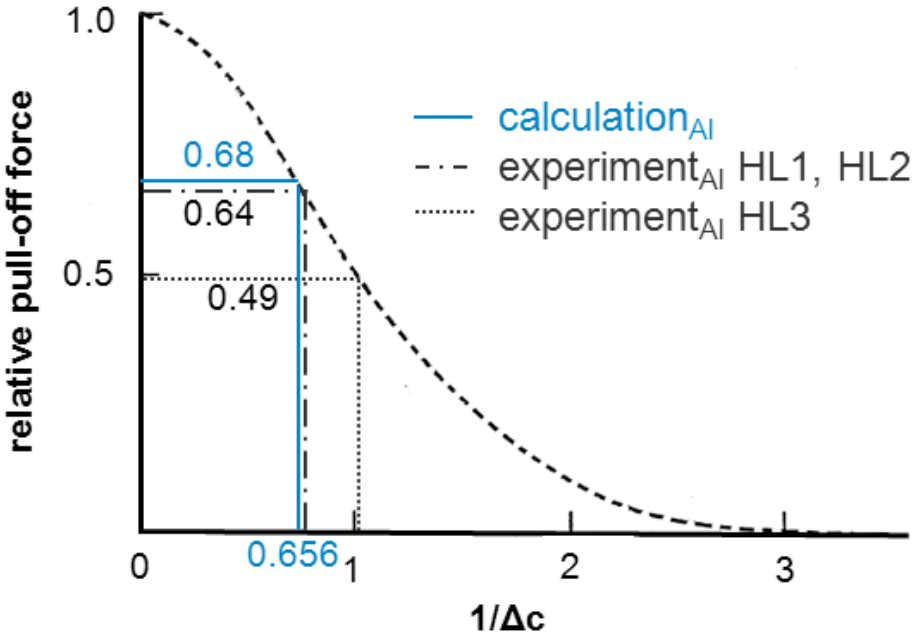

Figure 4.12: *Relative pull-off force plotted as a function of the adhesion parameter $1/\Delta c$, modified after Fuller and Tabor [33], with calculated relative pull-off force and experimental values of HL1, HL2 and HL3 on flat rough aluminum.*

4.5.3 Experiments on wavy rough substrates

In our study, we used two different wavy substrate surfaces to test the adhesive behavior of fibrillar surfaces. Some generic observations were made that shed light on buckling and adhesion mechanism. In the experiments on wavy substrates, mushroom shaped structures adhered better than flat tip structures as expected [57]. The tests on both wavy substrates also showed that the samples adhered best if they were positioned at the peak of the profile, while testing on the substrate surface of maximum inclination gave the lowest adhesion.

The positional dependence of buckling does not differ between the two wavy substrates. For the truncated sinusoidal and the sinusoidal substrate, buckling is favored at the intermediate positions between the wave peaks/flat part and the valleys, leading to a buckling preload with a frequency twice that of the substrate sinus. These findings confirm that the buckling behavior depends on the surface topography.

The adhesion behavior differs for the two wavy surfaces; for the truncated sinusoidal substrate, the non-hierarchical structures gave the highest pull-off values. Clearly, an introduction of a hierarchy is not favorable here. However, on the sinusoidal wavy substrate, the adhesion – although low – is comparable for the single level and multi-level hierarchical structures. It can be assumed that this is due to the longer wavelength of the substrate protrusions, where the pillars can better adapt to the wavy substrate.

4.5.4 Size 1 single pillar measurements

The theoretical buckling load value for a size 1 hexagonal pillar array shows that the best agreement was achieved by multiplying the sp measurements with the number of pillars and not to add the values according to a theoretical hexagonal pillar array value. But when the off-set of the individual force/displacement curves (presented in Figure 4.11) is accounted for, the agreement is even better. The repeated increase of the force F with larger displacement after the first buckling process can be explained by contact formation of the lateral side of the pillar. Deviations of *hp,experiment* and *hp,theory* values, which are based on sp measurements, occur because the interactions between the pillars are neglected and cannot be calculated using sp measurements. But the measurements showed that sp measurements can help to achieve a rough prediction for buckling preloads P_B for a hexagonal array on a wavy substrate but cannot replace the measurements with a real hexagonal array.

Overall, the insight created by our mechanistic study suggests that the design of hierarchical fibrillar adhesive surfaces needs to consider both their compressive and adhesive behavior. It is also likely that different design strategies will have to be applied to different degrees of roughness. The present paper is a first step in the direction of a rational design of such structures.

4.6 Conclusions

We have carried out a mechanistic study of hierarchical model adhesives in contact with substrate surfaces with model roughness. It can be concluded that the following considerations are essential in the design of hierarchical adhesive structures:

- Irrespective of number of hierarchies and other parameters, a mushroom tip shape leads to higher adhesion, both for rough and smooth surfaces.
- For optimizing adhesion, the sensitivity to buckling of the structure should be minimized. This allows higher compressive preloads resulting in higher adhesive strength. As hierarchical structures may have a higher propensity of buckling, highly hierarchical structures may not always be beneficial.
- In our study, no benefits were found for the introduction of a third hierarchy level. If adhesion has to be generated against a smooth substrate, a hierarchical system will not result in better results, but may decrease the structure stability and the permissible structure packing density. Also for small roughness amplitudes, a single hierarchical level may still be sufficient.
- The lateral dimensions of the structures have to be much smaller than the wavelength of the substrate. In our studies, we found similar adhesion for hierarchical and non-hierarchical structures with a substrate wavelength 10 times as large as the smallest pillar diameter.
- The effect of microroughness was reasonably well explained by the model of Fuller and Tabor.
- If a high compliance of the structure is necessary, e.g. to accommodate high roughness of the substrate surface, the introduction of hierarchy can lead to a compliance increase by a decreased buckling preload. By buckling 'into' asperities, such a structure has the potential of increasing the contact area and hence adhesion.

Although our study on hierarchical surface patterns gave a detailed insight into deformation behaviour and adhesion of more complex geometry, it has to be considered that vertical structures may not be the optimum design for application of bioinspired adhesives due to buckling effects. Future work should therefore consider angled hierarchical structures and their adhesive performance on rough surfaces.

Supporting Information

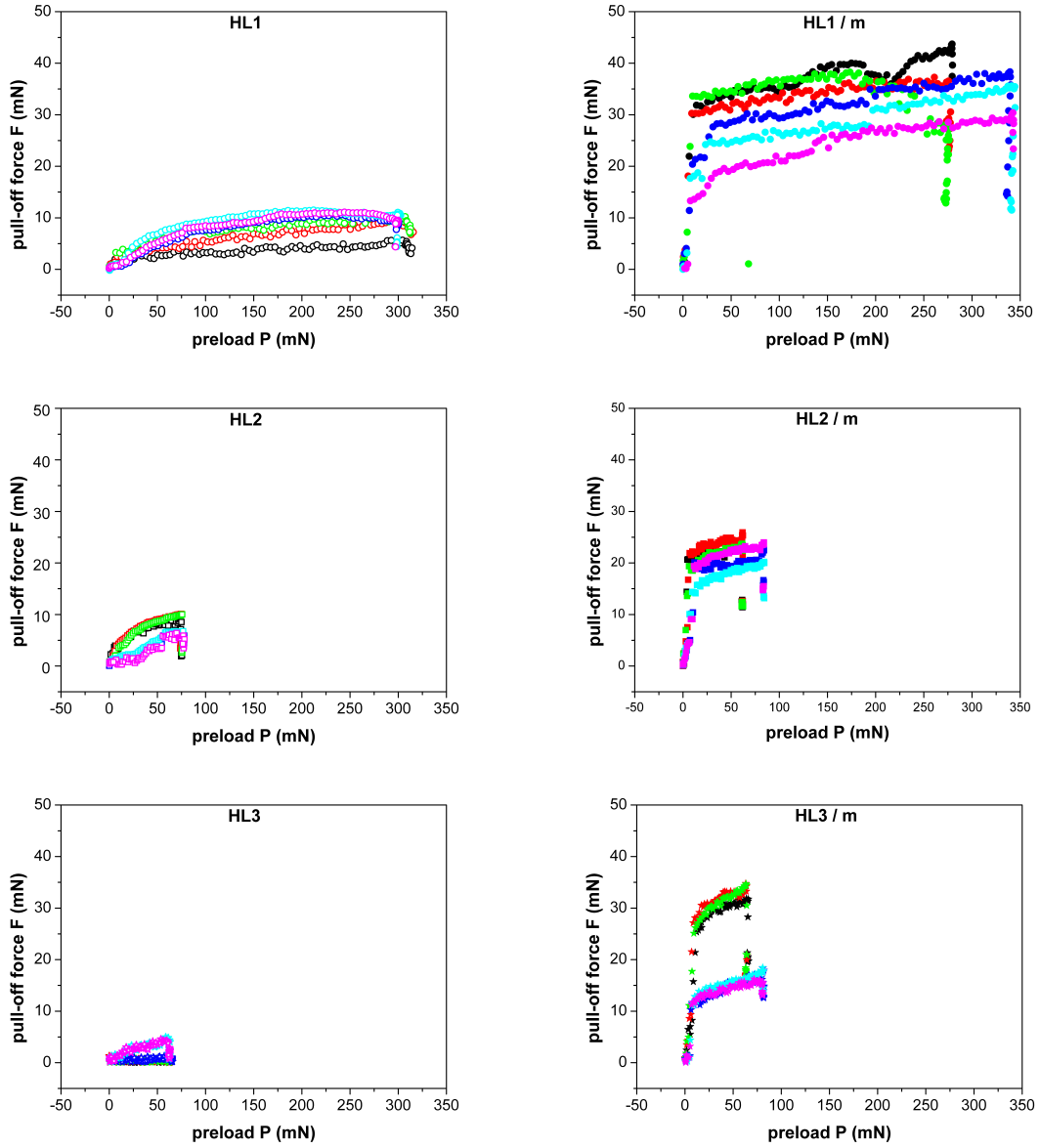

Figure A1: *Dependence of pull-off force* F *on applied preload* P *of HL1, HL2 and HL3 with (/m) and without mushrooms on a flat substrate.*

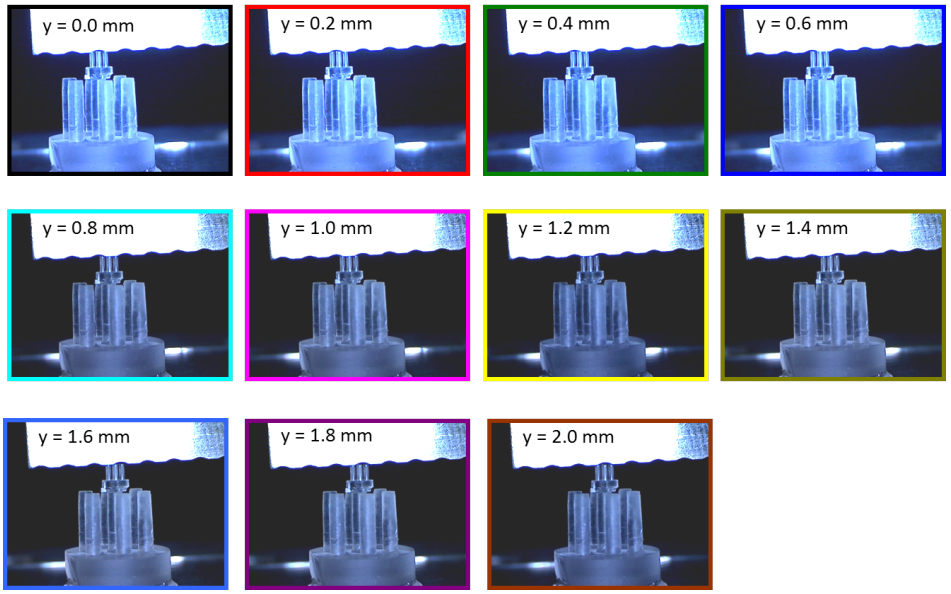

Figure A2: *Adhesion measurements of a HL2 sample at different positions of a wavy substrate. For each measurement, the sample was shifted by 0.2 mm.*

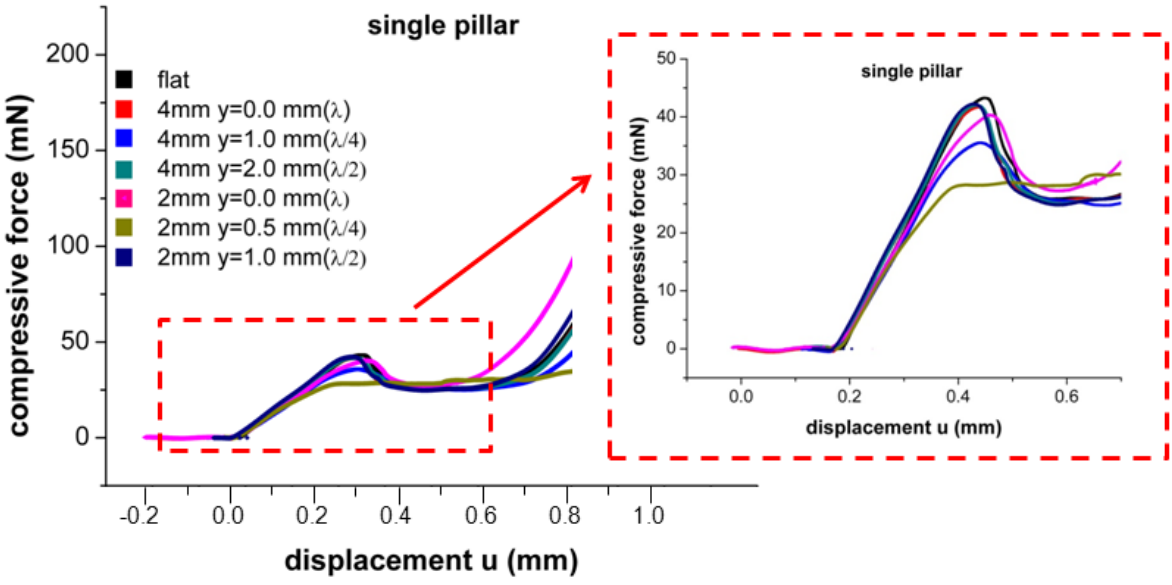

Figure A3: *Force/displacement curves measured on a flat, on a truncated wavy substrate ($\lambda = 2\,mm$, $h = 200\,\mu m$) and on a wavy substrate ($\lambda = 4\,mm$, $h = 200\,\mu m$). The results of the measurement curves are based on size 1 single pillar (sp) measurement results.*

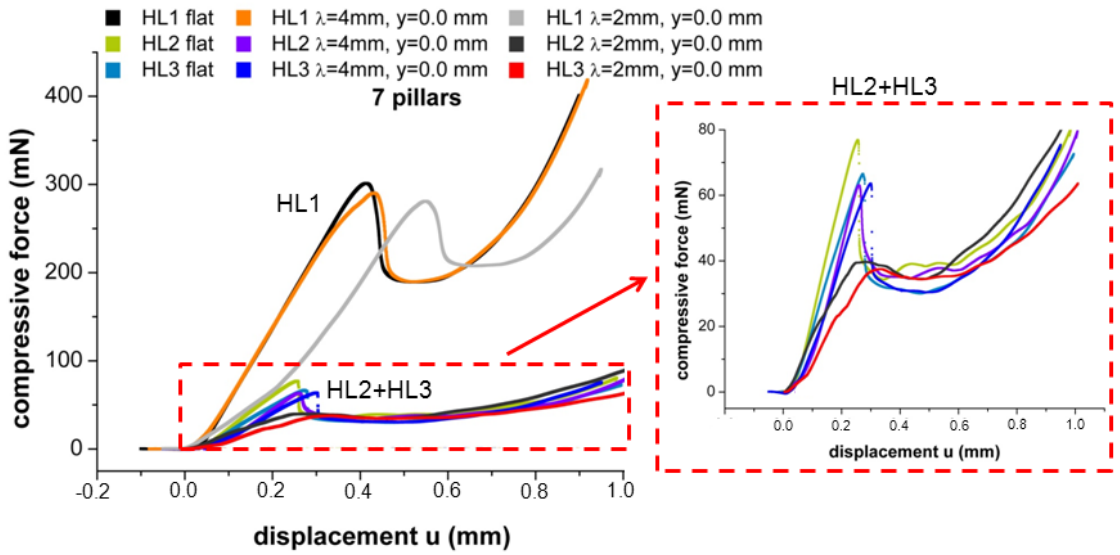

Figure A4: *Force/displacement curves measured on a flat, on a truncated wavy substrate ($\lambda = 2\,mm$, $h = 200\,\mu m$) and on a wavy substrate ($\lambda = 4\,mm$, $h = 200\,\mu m$). The results of the measurement curves are based on a HL1, HL2 and HL3 hexagonal pillar array (*hp*).*

A. Detailed estimation of the buckling load for a hierarchical pair of pillars

Consider the elastic buckling response of a pillar which has a stepwise jump in bending modulus along its length. The top pillar 1, of length l_1 and bending modulus $(EI)_1$, is supported by an underlying pillar 2, of length l_2 and bending modulus $(EI)_2$, as shown in Figure A5. The top end of pillar 1 is subjected to an end load P and is restrained against lateral motion by a force F, which only develops in the buckled state. The top end of beam 2 is adhered to the bottom of pillar 1, while the bottom end of pillar 2 is fully clamped. Now consider the buckled state of pillars 1 and 2. In the buckled state, the pillars deflect transversely into the shape *u(x)*. At any section x, the bending moment distribution is $M = (EI)_i\ \ddot{u}(\mathrm{x})$ (for columns $\mathrm{i} = 1{,}2$), where the prime denotes differentiation with respect to x, and

$$M(x) = (EI)_i \ddot{u}(x) = Fx - Pu(x) \tag{A1}$$

This second order differential equation has solution

$$u(x) = A\sin(w_1 x) + \frac{F}{P}x \tag{A2}$$

for pillar 1 and

$$u(x) = B\sin(w_2 x) + C\cos(w_2 x) + \frac{F}{P}x \tag{A3}$$

for pillar 2, where

$$w_i{}^2 = \frac{P}{(EI)_i} \text{ for } i = 1, 2. \tag{A4}$$

Imposition of the end conditions $u(l_1 + l_2) = \dot{u}(l_1 + l_2) = 0$ gives

$$C = -B\frac{(\sin\zeta - \zeta\cos\zeta)}{(cos\zeta + \zeta\sin\zeta)} \tag{A5}$$

where $\zeta = (l_1 + l_2)w_2$. Now impose continuity of $u(l_1)$ and $\dot{u}(l_1)$ at the junction between pillars 1 and 2. Then, A2 and A3, along with A5, imply

$$\begin{pmatrix} a_{11} & a_{12} \\ a_{21} & a_{22} \end{pmatrix} \begin{pmatrix} A \\ B \end{pmatrix} = \begin{pmatrix} 0 \\ 0 \end{pmatrix} \tag{A6}$$

where

$$a_{11} = (\cos\zeta + \zeta\sin\zeta)\sin(w_1 l_1) \tag{A7a}$$

$$a_{12} = (\sin\zeta - \zeta\cos(w_2 l_1) - (\cos\zeta + \zeta\sin\zeta)\sin(w_2 l_1)) \tag{A7b}$$

$$a_{21} = (\cos\zeta + \zeta\sin\zeta)w_1 l_1\cos(w_1 l_1) \tag{A7c}$$

$$a_{22} = -(sin\zeta - \zeta\cos\zeta)w_2 l_1\sin(w_2 l_1) - (\cos\zeta + \zeta\sin\zeta)w_2 l_1\cos(w_2 l_1) \tag{A7d}$$

Finite values for (A, B) are obtained when the determinant of a_{ij} vanishes, thereby defining the buckling equation for the load P. It is convenient to non-dimensionalise the problem to the form

$$\frac{P}{P_E} = f\left(\frac{(EI)_1}{(EI)_2}, \frac{l_2}{l_1}\right) \tag{A8}$$

where $P_E = \pi^2(EI)_1/{l_1}^2$ is the Euler buckling load for a pillar of length l_1, and bending modulus $(EI)_1$, and pivoted at both ends. Contours of P/P_E are plotted as a function of $(EI)_1/(EI)_2$ and l_2/l_1 in Figure A6 by solving for $det(a_{ij})=0$ using a root finding algorithm within MATLAB.

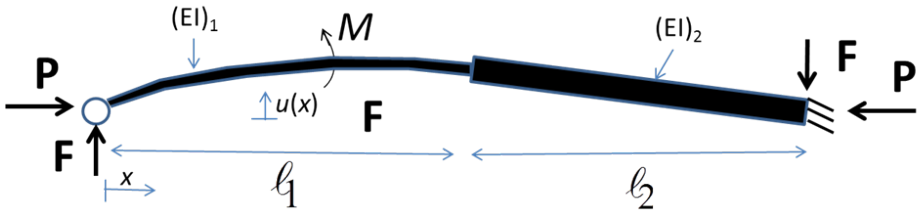

Figure A5: Schematic of the buckling/bending process of a HL2 with parameters.

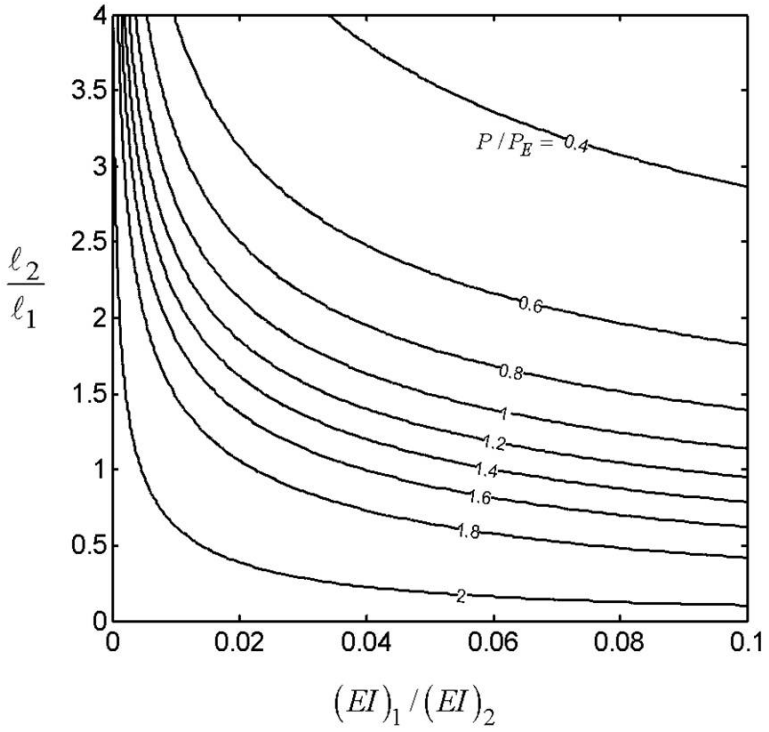

Figure A6: *Contours of* P/P_E.

$P/P_E = 0.423$. For a single pillar (size 1), $P/P_E = 2.05$, and so the ratio of buckling strength for HL1 and HL2 is $2.05/0.423 = 4.8$.

5 Size and shape evolution of PS particle layers during etching[1]

Within a project funded by the German Science Foundation (DFG) within the framework of SPP 1420 ('Biomimetic Materials Research: Functionality by Hierarchical Structuring of Materials') the second topic focussed on new fabrication methods which allow larger scale fabrication of micropatterned surfaces and at the same time can be combined with current state of the art patterning methods.[2]

5.1 Abstract

Crystalline monolayers of polymer particles are useful templates for surface microstructuring. In this chapter the use of oxygen plasma to tune interparticle distances in such films is discussed. A systematic evaluation of the etch process depending on particle size, plasma power, etching time and particle density was performed. The size evolution of individual particles was analyzed using scanning electron microscopy and compared with different models of the etching process. The authors conclude that none of the existing etch models fit the data very well. Analysis of the particle shape throughout the etching process indicates that changes in particle geometry occur depending on their original size and density. In dense films, bridges form between the particles' original contact points. Particles increasingly deviate from

[1] This chapter was published as a full paper: C. T. Bauer, A. Wonn, D. Brodoceanu, P. Born, E. Kroner, and T. Kraus, Size and shape evolution of PS particle layers during etching, *Bioinspired, Biomimetic and Nanomaterials*, 2:130–140, 2013 [3]. Paragraphs or sections, which are not content of the publication, are marked with a footnote.

[2] This paragraph is not content of C. T. Bauer, A. Wonn, D. Brodoceanu, P. Born, E. Kroner, and T. Kraus, Size and shape evolution of PS particle layers during etching, *Bioinspired, Biomimetic and Nanomaterials*, 2:130–140, 2013 [3].

a spherical geometry. Such shape changes are not captured by current models of the etching process. The authors propose a mechanism to explain the formation of bridges between the particles and their role in the preservation of long-range order.

5.2 List of notations

$\hat{y}_i$	theoretical data
d	bonds diameter between particles
D(t)	time dependent particle diameter
D_0	initial particle diameter
D_{crit}	critical particle diameter at which order is lost
df	standard deviation
$\|k\|$	absolute value of the etch rate
k	etch rate
k_1	etch rate of the Linear model
k_2	etch rate of the Spherical cap model
k_3	etch rate of the Constant volume-loss model
l(t)	time-dependant diameter of the area of a spherical segment
t	etching time
T_g	glass transition temperature
y_i	experimental data
ΔV	particle volume change
$\alpha(t)$	time-dependent linear increasing angle

5.3 Introduction

Microstructured polymer surfaces have applications in diverse fields [172]. For example, polymer microstructures have been created that mimic the adhesion system of the gecko [50, 54, 145, 146, 149, 173, 174]. Today, polymer surfaces are fabricated using combinations of electron beam [175, 176] or ion beam lithography [177], X-ray lithography [178] laser interference lithography [179, 180], photolithography [181–183] soft lithography [184–186] and

nanoimprint [125–127, 187].

Alternative routes to microstructured surfaces use monodispersed particles assembled into crystalline monolayers. Such monolayers have been created using Langmuir-Shaefer-like techniques [103–107], drop-casting [108], dip-coating [109], controlled drying [109, 110], spin coating [111, 112] and electrochemical deposition using a conventional three-electrode configuration [113, 114]. The convective particle assembly mechanism [115] occurs in several of these approaches and yields dense particle monolayers over a relatively large area. Dense polymer particle monolayers are useful primary patterns for the fabrication of biomimetic surfaces. Naturally occurring microstructures often comprise a simple unit cell with characteristic length scales below a micrometer that is repeated over macroscopic scales to control wetting, optical appearance, friction, adhesion [50, 54, 145, 146, 149, 173, 174] and others. Biomimetic, artificial versions of such microstructures can be efficiently fabricated when starting with a dense particle layer. First, the layer is etched until the desired spacing between the features is achieved. The particles are then converted into suitable geometries by a succession of etching and deposition steps. In this article, the authors discuss a reactive ion etching process that is suitable to define the spacing between the surface features. The authors discuss the microstructures that can be attained when etching polystyrene (PS) particle monolayers in oxygen plasma.

Table 5.1 provides an overview of the previous studies on this etch process. In all cases, PS particles were deposited as dense monolayers, subjected to plasma and analyzed for their geometry. The particles reduced their diameter and a spaced array resulted. All authors analyzed the temporal evolution of particle sizes to enable prediction of etching times required for specific spacings.

Effects of temperature on the etching process have been reported. Blättler et al. [109] and Vogel et al. [104] cooled the sample for an optimal etching result. Blättler et al. [109] observed that without cooling, the particles softened, deformed plastically and became connected by a confluent polymer layer. Vogel et al. [104] reported on a slight decrease in etching rates with increasing temperature.

Deviations from the original spherical shape after etching have also been reported. Blättler et al. [109] observed that particles etched to below 30 % of their original diameter assumed a

star-like appearance. A loss of spherical shape has also been reported by Brombacher et al. [188]. Shape changes were exacerbated when the particles had been thermally treated before etching. Cong et al. [189] annealed PS spheres at a temperature of 110 °C for 1 and 2 min before the plasma treatment to improve the layer quality after the etch. They reported that the treatment prevented the plasma from moving the particles by increasing their contact area with the substrate and with each other, thereby retaining long-range order. The authors are not aware of a detailed analysis on when the original order of the particle monolayer is lost.

In this article, the authors analyze in detail the temporal evolution of PS particles in oxygen plasma depending on time, plasma power, initial particle diameter and density of the particle layer. The authors fit the data with different models that have been proposed and show that none fits significantly better than a simple linear law. In the second part, the authors analyze the evolution of the particle shapes from their original spherical geometry to the final morphology and the loss of order that occurs in the process.

5.4 Methods and materials

Monolayers were prepared from PS lattices through convective assembly. Silicon wafers with <100> crystallographic orientation (Asahi Kasei, Tokio, Japan) were used as substrates. Four different sizes of monodispersed PS particles with diameters of 0.25 µm (*Polystyrene solids*, Bangs Laboratories, USA), 0.5, 1 and 3 µm (*carboxyl latex* 4 % w/v, coefficient of variation of diameter: 0.5 µm 1.1 %, 1 µm 4.5 %, 3 µm 6.0 %, Invitrogen, Darmstadt, Germany) were used. The silicon substrates were cleaned with isopropanol (*Normapur*®, purity 99.7 %, VWR, Germany) and treated with oxygen plasma (50 W, 5 min) to remove residues and to improve wetting. The particles were deposited on the silicon substrate using convectively assisted particle assembly on a specialized setup. Details on the setup and the process can be found in previous publications [115]. Briefly, the setup consists of a glass slide that is moved against the substrate by a linear motor (*Precision Linear Stage PLS-85*, miCos GmbH, Eschenbach, Germany). A suspension reservoir is held between glass slide and substrate and leaves a thin wetting film upon displacement. Evaporation drives particles into a dense particle film

Table 5.1: *Overview of the literature of particle etching.*

Author	**Particle diameter** D_0	**Etched fraction of the initial diameter**	**Plasma reactor**	**Process gases**	**Analysis**
Blättler et al. [109]	220 nm, 500 nm, 2 µm	Nearly completely	RIE-ICP system Type 80 Plus (Oxford)	Equal fractions of N_2 and O_2	Particle diameter
Brombacher et al. [188]	180 nm	Nearly completely	RIE-ICP system Type 80 Plus (Oxford)	O_2	Particle diameter
Chau et al. [113]	200 nm, 500 nm	Less than 50 %	RIE-ICP system Type 80 Plus (Oxford)	Pure O_2, Ar and O_2 mixture	Particle diameter
Chau et al. [107]	200 nm	Nearly completely	RIE-ICP system Type 80 Plus (Oxford)	O_2	Particle diameter
Cheung et al. [112]	500 nm	Less than 50 %	RIE	Different fractions of CF_4 and O_2	Particle diameter
Cong et al. [189]	465 nm, 1 µm		March PX-250 plasma etching system	O_2	Neck length and neck width
Haginoya et al. [190]	200 nm	Nearly completely	RIE	O_2	Particle diameter
Li et al. [103]	320 nm	Less than 50 %	RIE-ICP system Type 80 Plus (Oxford)	O_2	Particle diameter
Pai et al. [111]	500 nm		RIE	O_2	Distance between particles
Plettl et al. [108]	100 nm, 200 nm	More than 50 %	RIE-ICP system TYPE 80 Plus (Oxford)	O_2	Particle diameter
Vogel et al. [104]	246 nm, 408 nm	More than 50 %	Plasma cleaner Femto (Diener Electronic)	O_2, pure Ar	Particle diameter
Yan et al. [191]	200 nm, 300 nm, 500 nm, 1 µm 2 µm	More than 50 %	Plasma reactor JEH-OOTS, Jeol	Ar	Particle diameter
Zhang et al. [105]	200 nm	Less than 50 %	RIE system MERIE ME-3A mold, China	O_2	Particle diameter

that forms under appropriate conditions. The setup includes an optical microscope (*Axio Imager A1m*, Zeiss, Oberkochen, Germany) for in situ observation and tuning the deposition parameters. Sparse particle layers were created by dispensing a drop of diluted particle suspension on a silicon wafer and slowly drying it.

Thermal annealing was performed prior to plasma treatment.The monolayers were placed in a convection oven (*Haraeus Vacuum Heating and Drying Ovens*, Thermo Fisher Scientific, Waltham, MA, USA) for 60 s at 110 °C above the glass transition temperature (T_g) of PS. Particles with 1 µm diameter were annealed for 90 s.

The particles were etched in a plasma reactor (*PICO Variante E*, Diener Electronic, Ebhausen, Germany) at different radio frequency (RF) power (10–80 W, RF = 13.56 MHz) and exposure times (2–90 min). An oxygen flow of 220 cm^3/min was maintained throughout the etch process. The plasma chamber, a quartz tube, had an inside length of 300 mm and a diameter of 140 mm. Samples were placed on the centre of the bottom electrode, made of aluminium. In some experiments, the plasma chamber was vented at regular intervals to allow the setup to cool down. The plasma reactor had a temperature sensor integrated into the electrode on which the samples were placed.

Geometrical analysis of the sample was performed using scanning electron microscopy (*FEI Quanta 400F Rasterelektronenmikroskop*, FEI Europe, Eindhoven, the Netherlands). The etched particle layers were coated with a thin gold film (≈ 30 nm) in a standard magnetron sputter-deposition system (*Auto Fine Coater*, JEOL JFC-1300, Japan) to reduce the effect of electrostatic charging. A secondary-ion-detector was used to record images at an accelerating voltage of 12.5 kV. All images were analyzed by using ImageJ software (available to download from National Institutes of Health). The hexagonal order was determined by visual inspection of the images. The diameters of five particles were measured for each sample (this number of particles was sufficient because the deviation was negligible). To obtain the time-dependant diameter D(t), the average was calculated from these five values. The data points were fitted by using different etch models (see Section 5.5). All fits were performed using the *Origin 8* software package (OriginLab Corporation) with the Levenberg-Marquardt algorithm [192] (see www.originlab.de). The quality of the fit was quantified using the reduced χ^2, which is

the residual sum of squares (RSS) divided by the standard deviation (df), $\chi^2 = \mathrm{RSS}/\mathrm{df}$, RSS equaling

$$RSS = \sum_{i=1}^{n} (y_i - \hat{y}_i)^2 \tag{5.1}$$

where y_i is the experimental and $\hat{y}_i$ the theoretical data. Values of reduced χ^2 between 0 and 1 indicate a good fit (see www.originlab.de).

The particle based softmolding was performed with particles which were deposited on a silicon wafer and on a thin PS layer on a silicon wafer through convective assembly and were molded with polydimethylsiloxane (PDMS). To produce the thin PS layer on the silicon wafer, polystyrene was dissolved in toluene (mass fraction of the solved component $w = 0.028$). The resulting solution was used for spin-coating. The solution was spin-coated (*CT62 Virgin*, Süss MicroTec AG, Garching, Germany) 3500 rpm for 15 s. With this adjustments the thickness of the PS layer was 178 nm ± 8 nm. The coating thickness was determined by ellipsometry (*M-2000DI Ellipsometer*, J. A. Woolam Co., Inc., Lincoln, Nebraska, USA). The PDMS material was prepared by mixing the pre-polymer and cross-linker in a 10:1 ratio from the *Sylgard 184* kit (Dow Corning Ml, USA). To remove air bubbles, the mixture was degassed in a desiccator. The samples, particles on the polystyrene layer, were annealed in the oven (110 °C, 10 min) and treated subsequent with oxygen plasma (20 W, 10 min). Before the PDMS was poured on the substrates the samples were treated with oxygen plasma (50 W, 1 min) to make the surface more hydrophilic. The PDMS was cured by 75 °C in the oven for at least 12 h. The PDMS structures were exposed in the solvent acetone for 24 h to solve the polystyrene. To enhance the cleaning effect of the solvent an ultrasonic bath was used for 15 min.[3]

[3]This paragraph is not content of C. T. Bauer, A. Wonn, D. Brodoceanu, P. Born, E. Kroner, and T. Kraus, Size and shape evolution of PS particle layers during etching, *Bioinspired, Biomimetic and Nanomaterials*, 2:130–140, 2013 [3].

5.5 Results and discussion

5.5.1 Particle size

Monolayers of PS particles with initial diameters of 0.25, 0.5, 1 and 3 µm were etched in oxygen plasma. The samples were first annealed at 110 °C for 60 s (1 µm particles for 90 s) to create strong particle-substrate junctions. Then, each sample was exposed to oxygen plasma at a constant power setting for a defined period, removed from the plasma reactor and analyzed by electron microscopy. Figure 5.1 and Figure B1 (in the Supporting Information) show typical sets of scanning electron microscopic images that indicate the particles' shrinking. Note that separate samples were used for every combination of etching time and RF power. Plasma variations were ruled out by repeating etches at identical settings and finding negligible differences between different runs.

Sample temperature during etching may influence the etch rate [104, 109]. Such effects were evaluated in a second set of experiments by venting the plasma chamber at regular intervals so that the setup could cool down. Only minor differences were found between samples etched continuously and those etched in multiple steps to avoid overheating. The temperature influence seems to be small at least for particles with initial diameters of 0.5 and 3 µm at 40 W RF power. Flat PS layers, however, etched slightly faster, if no cooling was allowed.

Samples with disordered, sparse particle layers were also prepared to assess the effects of particle proximity. Dense and sparse particle layers with original diameters of 0.5 and 3 µm were etched at 40 W RF power and compared with each other. In sparse particle layers, particles covered an area fraction below 10 %, while dense layers covered 80–90 % of the substrate. Particles in sparse layers were etched more rapidly.

For example, particles in sparse layers with 0.5 µm original diameter were 30 % smaller than particles in dense layers after 15 min etching time. Reference measurements were performed on homogeneous PS layers on silicon wafers. The PS layer can be considered as a monolayer of particles with infinite diameter. Figure B2 shows the temporal evolution of its thickness.

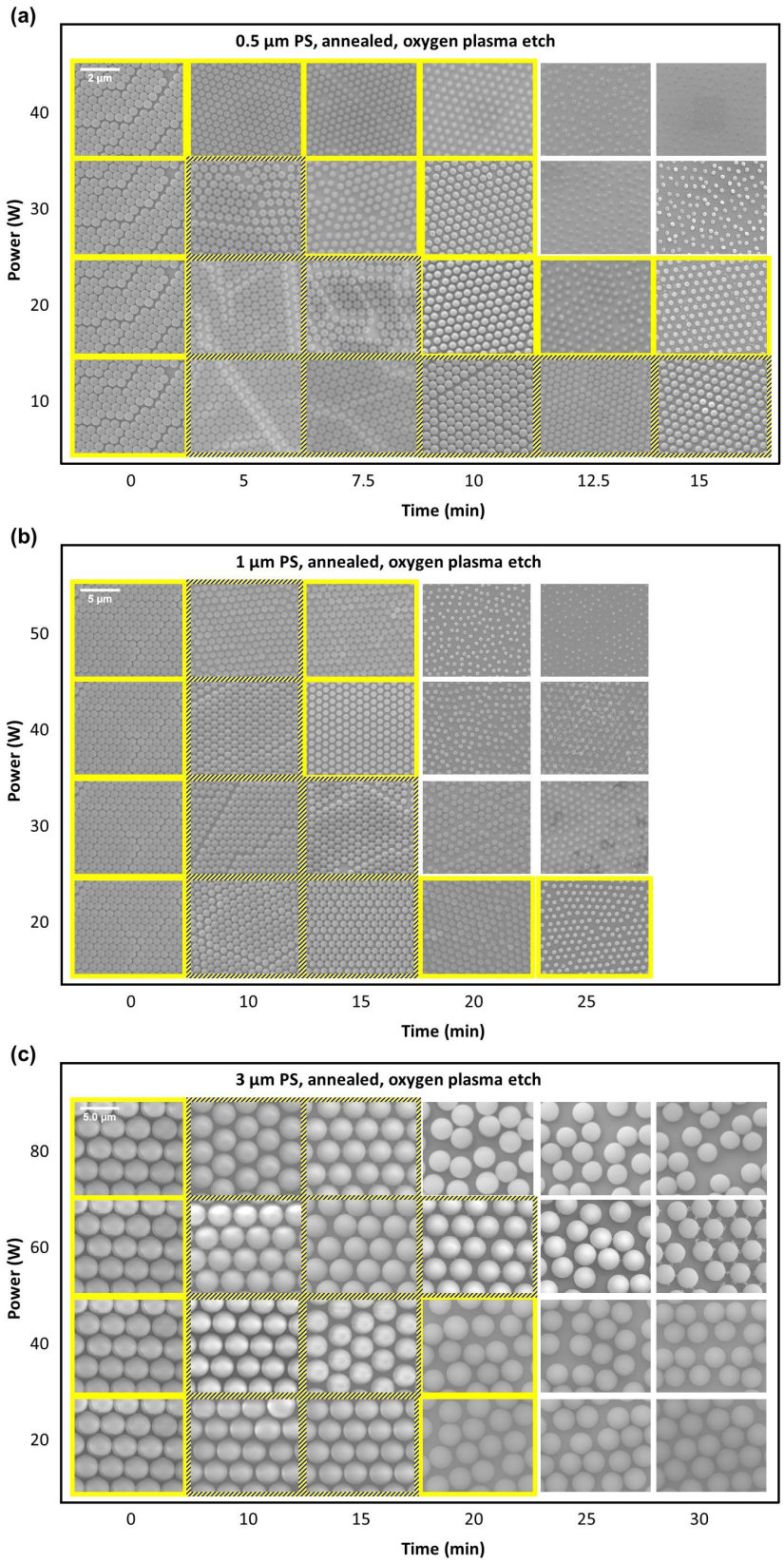

Figure 5.1: *Electron micrographs of PS particle monolayers etched for different times (original particle diameters D_0: (a) 0.5 µm, (b) 1 µm and (c) 3 µm. Samples, where order was retained, are marked with a yellow border; samples that retained order and developed bridges between particles are marked with a yellow-blue border. The scale bar in (a) is 2 µm and in (b) and (c) 5 µm and applies to all pictures.*

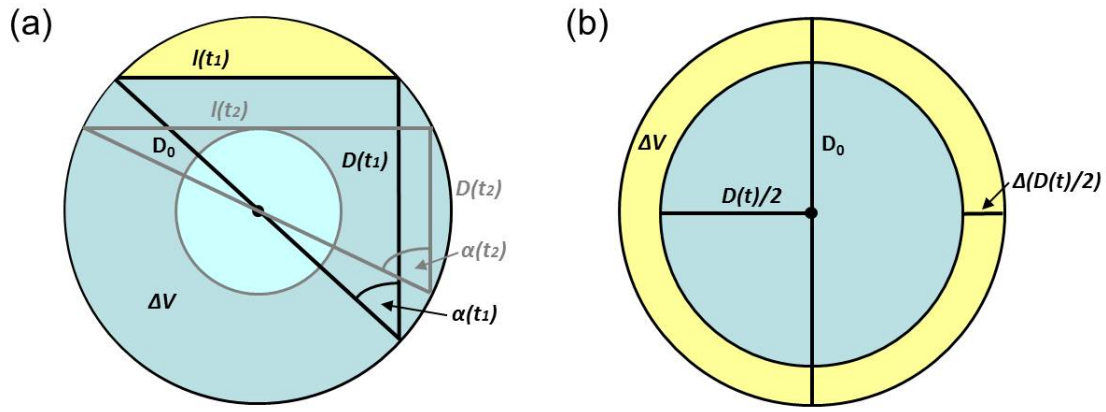

Figure 5.2: *Symbols used in the derivation of (a) spherical cap model for the etch rate and (b) constant volume-loss model, a new model that assumes constant isotropic etching.*

In the following, the authors use three different models to fit the time-dependant diameter of the etched particles. Several publications report a linear dependence of the particle diameter D_0 on the etch time t [103, 104, 107–109, 112, 113, 188]:

$$D(t) = k_1 t + D_0 \tag{5.2}$$

where k_1 is a constant that fully characterizes the etch process and D_0 is the original particle diameter. This relation is denoted 'linear model' throughout this article.

Yan et al. [191] and Zhang et al. [105] refer to a model due to Haginoya et al. [190] that assumes etching from the top of the sphere (illustrated in Figure 5.2(a)). Haginoya et al. [190] assumed that a particle with an initial diameter D_0 is etched with a linearly increasing angle α (Figure 5.2(a)). Using Haginoya's symbols, the angle change translates into a size change of the particle according to $sin\alpha(t) = l(t)/D_0$, so that the diameter declines with time according to

$$D(t) = D_0 cos\left(arcsin\frac{k_2 t}{2D_0}\right) \tag{5.3}$$

where k_2 is a constant that fully characterizes the etch process and D_0 is the original particle diameter. This relation is referred to as 'spherical cap mode' throughout this article.

A third model (illustrated in Figure 5.2(b)) that the authors introduce here is based on the assumption that the volumetric etch rate remains constant during the entire etch and that the etch is entirely isotropic. The differential change in volume is then

$$\Delta V = \frac{4}{3}\pi\left(\frac{D}{2} + \Delta\left[\frac{D}{2}\right]\right)^3 - \frac{4}{3}\pi\left(\frac{D}{2}\right)^3 \tag{5.4}$$

where D_0 is the initial particle diameter and $\mathrm{D} = \mathrm{D(t)}$ the time-dependant diameter. Integration leads to a time-dependant diameter

$$D(t) = \left(8k_3 t + {D_0}^3\right)^{\frac{1}{3}} \tag{5.5}$$

where k_3 is the model-dependant etch rate. This relation is denoted 'constant volume loss model' throughout this article.

Fits using the three models were performed for all particle diameters and plasma powers for both dense and sparse particle layers. The details of the fits are included in Figures B3–B8 of the Supporting Information. Figure 5.3 shows the magnitude of the models' constants for the different etches. The authors also evaluated the quality of the fits using the reduced χ^2 (Figure 5.4).

Figure 5.4 shows the quality of the fits for the above three models when etching dense particle layers of different particle sizes. The bars indicate the reduced χ^2 averaged over fits at all plasma powers, the error bars indicate the standard deviation. The temporal evolution of particle size depended on RF power and original diameter. The simplest (linear) etch model provides the best fit in all cases, whereas more complicated models do not provide better agreement. The average quality of all fits – including the linear model – is poor, however. Note that the etching of a continuous thin film is almost perfectly fit by the linear model (Figure 5.4(a)).

It is questionable how meaningful it is to derive model constants from such poor fits. It is interesting, however, that the constants obtained in all three fits indicate the expected trends: Figure 5.3 indicates increasing absolute values of the three different fitting constants with

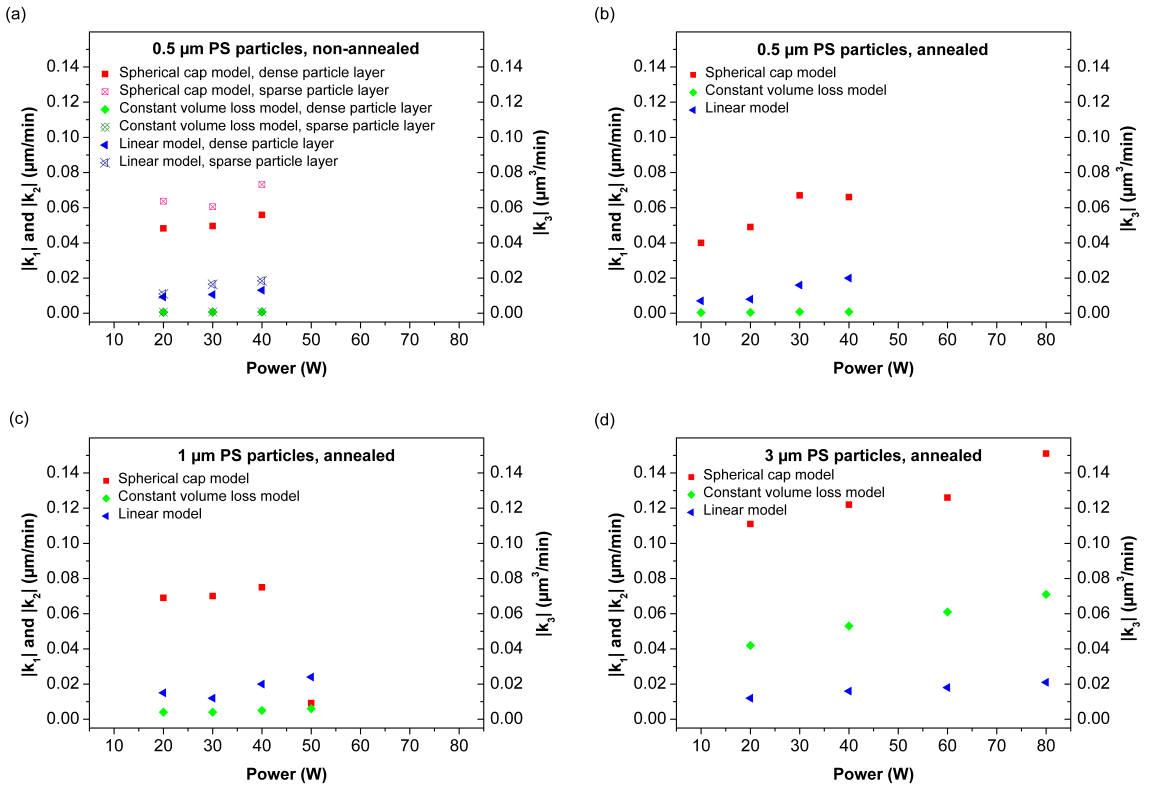

Figure 5.3: *Absolute values of the parameters obtained by fitting three different etch models to the size evolution of dense and sparse PS particle layers (original diameter of (a) 0.5 µm, non-annealed, (b) 0.5 µm, annealed, (c) 1 µm, annealed and (d) 3 µm, annealed).*

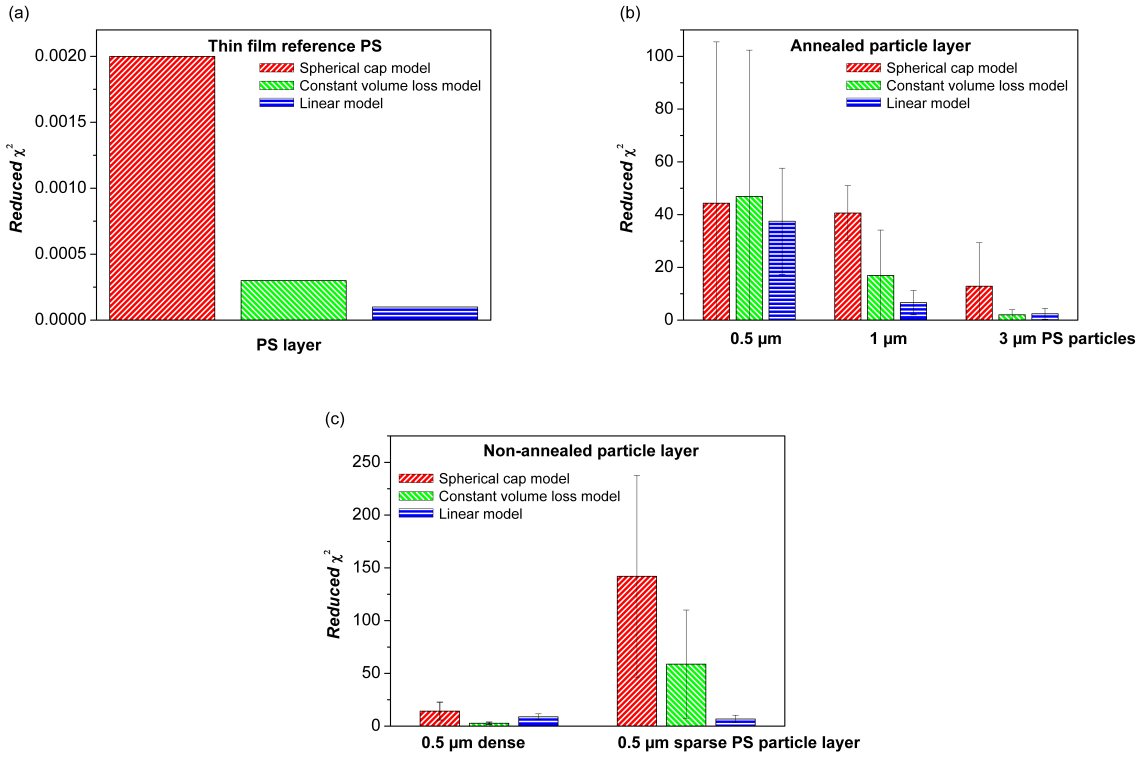

Figure 5.4: *Quality of fits (measured as reduced χ^2) for three models fitting the evolution of (a) the planar reference PS layer, (b) dense, annealed PS particle layers (original diameter of 0.5, 1 and 3 µm) and (c) dense and sparse non-annealed PS particle layers (original diameter of 0.5 µm).*

increasing RF power, corresponding to increasing etch rates. If the goal of such fits is merely to provide a rough prediction of the etching time needed to reach a certain particle size, a linear fit is sufficient and an etch rate of 0.015 µm/min gives a rough estimate (Figure 5.5). It is not possible, however, to reconstruct the actual etch mechanism by comparing different fits.

Deviations from the proposed models have been reported earlier. For example, Vogel et al. reported a stagnation of the particle diameter during etching after some time [104], which we also observed after 10–15 min for particles with initial diameters of 0.25 and 0.5 µm (see Figure 5.6(a) and Figure 5.6(b)). The data points after saturation were disregarded in all fits, but the agreement remained poor. The authors believe that the origin of the poor fits is the deviation of the particle from their original spherical geometry. In the second part, the authors analyze the shape changes that occur during etching.

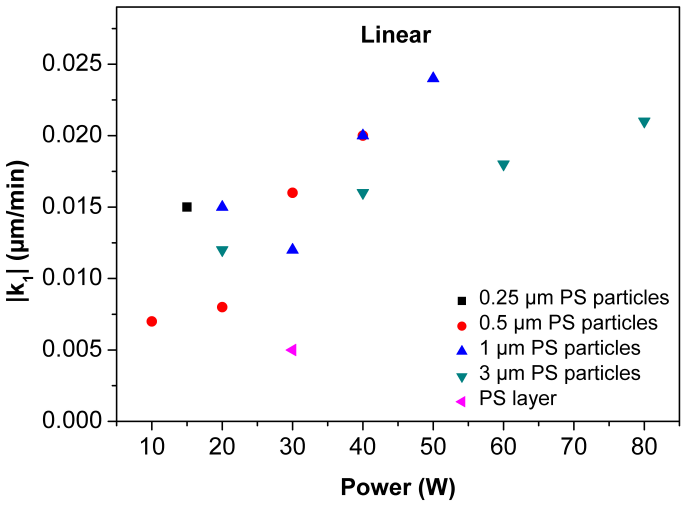

Figure 5.5: *Absolute values of the etch rate $|k_1|$ obtained by linear fitting of dense PS particle layers (original diameter of 0.25, 0.5, 1 and 3 µm) and the planar PS layer.*

5.5.2 Particle shape and arrangement

Figure 5.1 clearly indicates morphological changes in both particle geometry and particle arrangement. At the beginning of the experiment, every sample exhibited hexagonal order (indicated by a yellow border in Figure 5.1). During etching, bridges between the particles

formed (indicated by a yellow-blue border in Figure 5.1). The bridges disappeared in the further process before the hexagonal order was lost. Both changes occurred earlier for increased RF power. Morphological changes occurred for both sparse and dense particle layers. The deviation from the spherical shape toward the end of the etching process was smaller for sparse particle layers but still noticeable. The evolutions of the particle diameters did not follow simple linear or any of the other proposed etch laws for both dense and sparse particle layers.

Samples with disordered, sparse particle layers were also prepared to analyze etching effects on particle shape and arrangement. Bridges only occurred in dense layers. Qualitatively, the deviation from the spherical shape toward the end of etching was smaller for sparse layers, but still noticeable.

Figure 5.6(a)–5.6(d) illustrate the decline in particle diameters during the oxygen plasma etch as a function of RF power. The loss of order and the presence of bridges between the particles are indicated. The smallest particles (0.25 µm diameter) could not be analyzed in any detail, they etched rapidly even at the lowest RF powers that could be set reliably. They were not considered further in this study. Tables B1–B4 in the Supporting Information provide a fully detailed overview on the morphological changes that occurred during the etch treatments.

The development of polymer bridges between the shrinking particles, an effect also observed by Cong et al. [189], is a striking deviation from an isotropic etch mechanism. It only occurred in dense particle layers and was more pronounced if the layer had been thermally annealed. The authors believe that annealing converts the small contact points of densely packed particles into larger contact areas. The annealing was performed at 110 °C, which is slightly above glass transition temperature for PS particle ($T_g = 100\,°C$) during which the point contacts between particles are converted to area contacts [189].

The authors proposed a mechanism for bridge formation that explains the observed structures (see Figure 5.6(e)). Longer annealing times result in thicker bonds d between particles. Upon oxygen plasma treatment, the surface of PS particles is isotropically etched. The reactive plasma etches the exposed surface including the bonds between particles, which are slowly

converted to bridges that thin until they break at a critical particle spacing. Longer annealing times result in larger particle contact areas and, thus, to a greater stability of the bond.

The bridges have a stabilizing effect on the lateral position of particles on the substrate [189]. This effect is further enhanced by the presence of particle-substrate bonds that also develop during annealing. The authors often observed the emergence of six protrusions on the particles after the bridges had been broken and etched away that indicate the hexagonal order in the original monolayer.

The protrusions were located on each particle surface where the bonds originally occurred, while their size was related to the thickness d of the initial bonds formed during the annealing process. Figure 5.6(e) shows the typical hexagonal shape of the individual particles after annealing and etching.

Thermal annealing therefore helps retaining a regular structure in two ways: it increases the particles' contact area with the substrate, which prevents rolling, and induces the formation of bridges that retain long-range order. If the thermal annealing times were above 60 s, the bridges became 'skins' as shown for 1 µm particles in Figure 5.1(b): polymer planes partially connecting the particles over their entire perimeter. Such skins were etched during the plasma treatment until they became bridges.

Figure 5.6(f) shows the critical particle diameter D_{crit} at which order is lost as a function of the original particle diameter D_0. D_{crit} is nearly independent from the RF power and the etch time. The particles with an initial diameter of 3 µm reached D_{crit} after a size reduction of 5 %, 1 µm of 47 %, 0.5 µm of 63 % and 0.25 µm of 68 %: smaller D_0 lead to increased ratios between D_{crit} and D_0. The gap between the particles at D_{crit} ranged between 150 and 500 nm but did not exhibit a simple relation to D_0. The authors believe that the geometry of the bridges depends on the original particle size. The bridges reliably retain order. When they are etched after a time that depends on the original particle size and the annealing time, order persists for a short additional period that depends on the same parameters. Finally, the particle-substrate bond also breaks and order is lost.

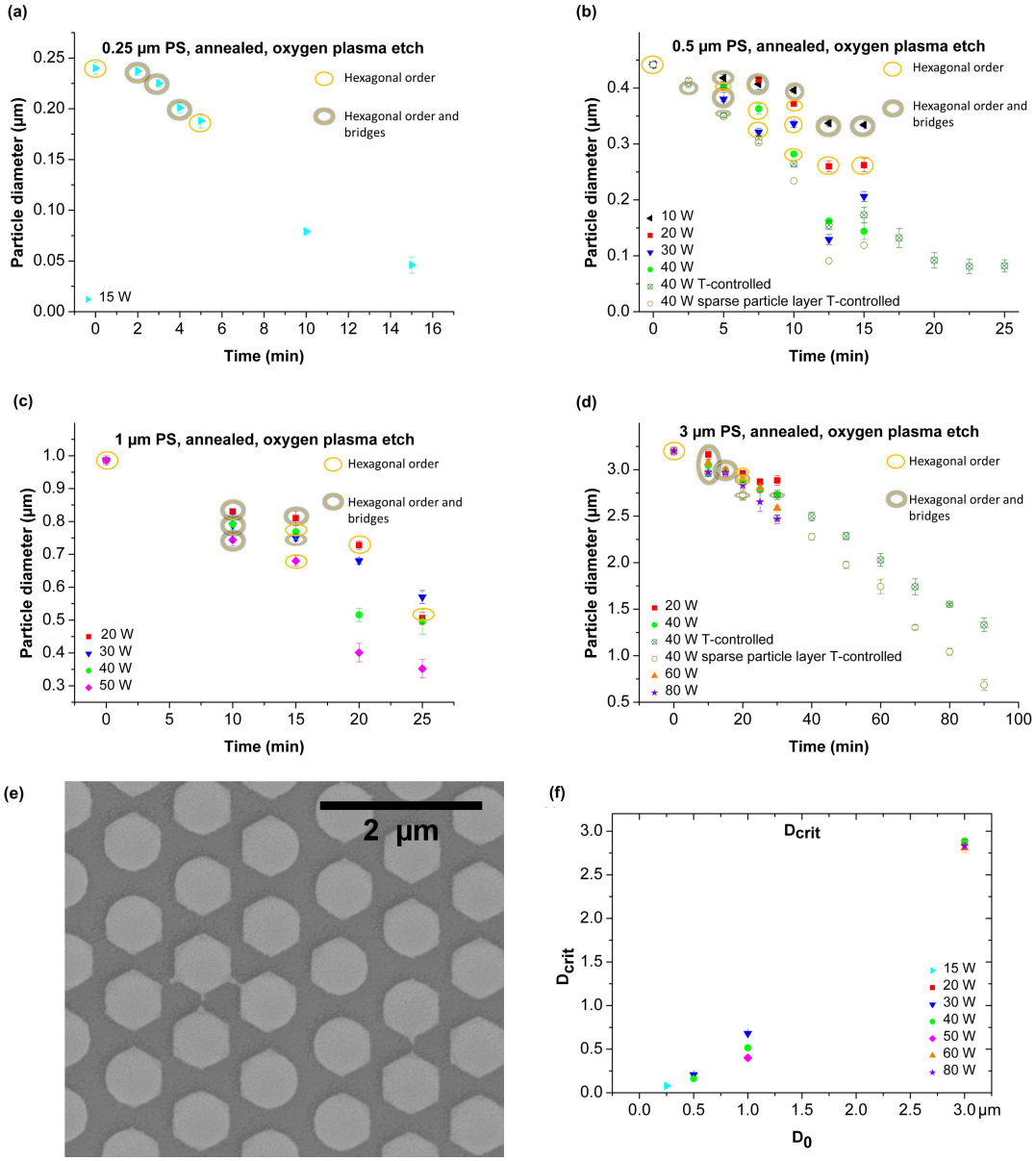

Figure 5.6: *(a)–(d) Time-dependent particle diameters of dense particle layers at different RF powers in continous or intermittent etching (original particle diameters D_0: (a) 0.25 µm, (b) 0.5 µm, (c) 1 µm and (d) 3 µm). Yellow rings indicate hexagonal order; yellow rings with blue edge indicate hexagonal order and bridges between the particles. (e) Top view SEM micrograph of PS particles (diameter of 1 µm) after 90 s annealing at 110 °C and subsequent oxygen plasma treatment (15 min at 40 W RF power). Hexagonal shape was assumed by further etching of the particles. (f) Critical particle diameter D_{crit} at which order is lost over the initial diameter D_0 depending on the RF power.*

5.6 Particle based softmolding[4]

5.6.1 Particle based softmolding of PS particles on a silicon substrate

PS particles with different original diameter were deposited on an oxygen plasma treated silicon surface and were molded with PDMS. In Figure 5.7 a PDMS structure molded with PS particles with an original diameter of 0.25 µm is presented. Particle-like structures (ps), continous PDMS layer (ls) and so called 'golfball structures' (gs) are visible. Golfball structures are circular dimpled structures and resemble a golfball surface.

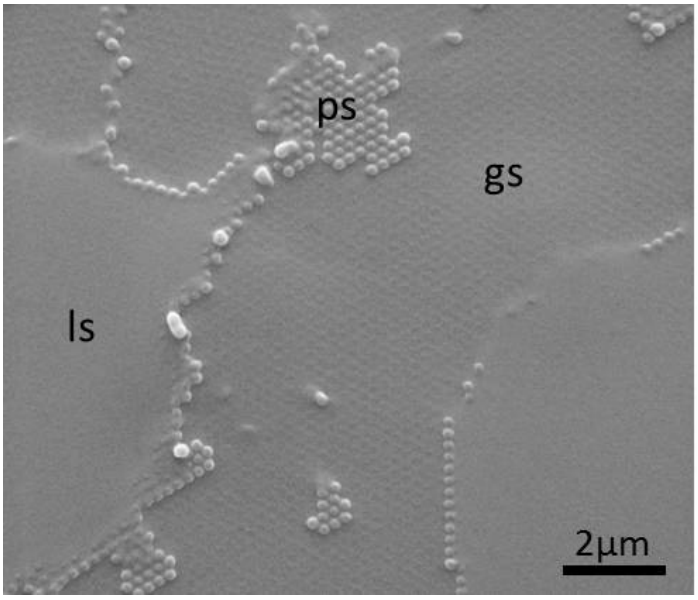

Figure 5.7: *PDMS molding: 0.25 µm PS particles deposited on an oxygen plasma treated (50 W, 5 min) silicon surface, molded with PDMS and cured in an oven for 12 h. Particle-like structures (ps), continous PDMS layer (ls) and golfball structures (gs) are visible.*

A PDMS mold of PS particles with original diameter of 0.5 µm is presented in Figure 5.8. There were large areas with golfball structures (gs) and mushroom shaped structures (ms). But there were also particle-like formations (ps).

In Figure 5.9 a PDMS mold of 1 µm (diameter) PS particles is presented. The experimental approach was the same as above, but PS particles with 3 µm diameter were used. On the PDMS molding similar structures were observed in comparison to the other size structured

[4]This section is not content of C. T. Bauer, A. Wonn, D. Brodoceanu, P. Born, E. Kroner, and T. Kraus, Size and shape evolution of PS particle layers during etching, *Bioinspired, Biomimetic and Nanomaterials*, 2:130–140, 2013 [3].

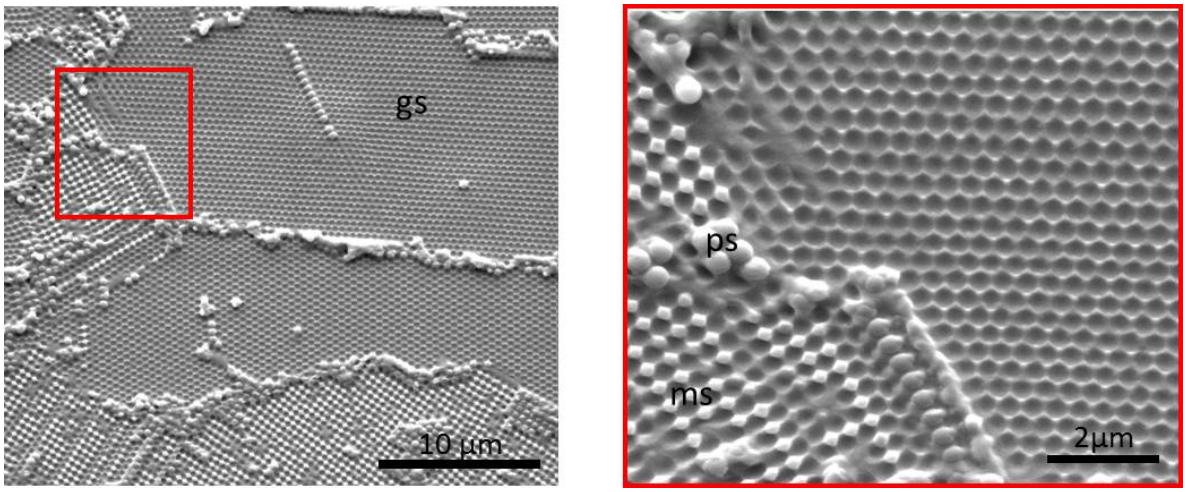

Figure 5.8: *PDMS molding: 0.5 µm PS particles deposited on an oxygen plasma treated (50 W, 5 min) silicon surface, molded with PDMS and cured in an oven for 12 h. Particle-like structures (ps), golfball structures (gs) and mushroom shaped structures (ms) are visible.*

PDMS surface. There were also areas resembling golfball structures (gs), structures which resemble to mushroom shaped structures (ms), and particle-like formations (ps).

In Figure 5.10 a golfball structure (gs) is shown. The experimental approach was the same as above, but PS particles with 3 µm diameter were used. A lot of particle-like structures were on the sample. Regions with a continuous polymer layer (ls) were observed and mushroom shaped structures (ms) were only found in small areas.

The particle based softmolding of PS particles on a silicon surface worked with particles with a diameter of 0.25 µm, 0.5 µm, 1 µm and 3 µm. Parts of the PDMS moldings look like golfball structures (gs). These structures could be achieved because the particles are densely packed and the PDMS could not flow between the particles. PDMS has a high viscosity. An additional reason could be that the stabilizer (formic acid) on the surface of the PS particles, which was added during the industrial fabrication process, makes the shell of the particles hydrophilic. Thereby the wettability of the particles could be reduced because PDMS is hydrophobic. But sometimes there are structures with little elevations, which resemble mushroom-shapes (ms). The PDMS could flow around the particles to the silicon surface. Particle-like formations (ps) have also been observed. These are probably particles, which were embedded into PDMS. But it can be also assumed that some particles did not stick to the substrate and were detached with PDMS. If too much PDMS flows under the particles, the result is a continous PDMS

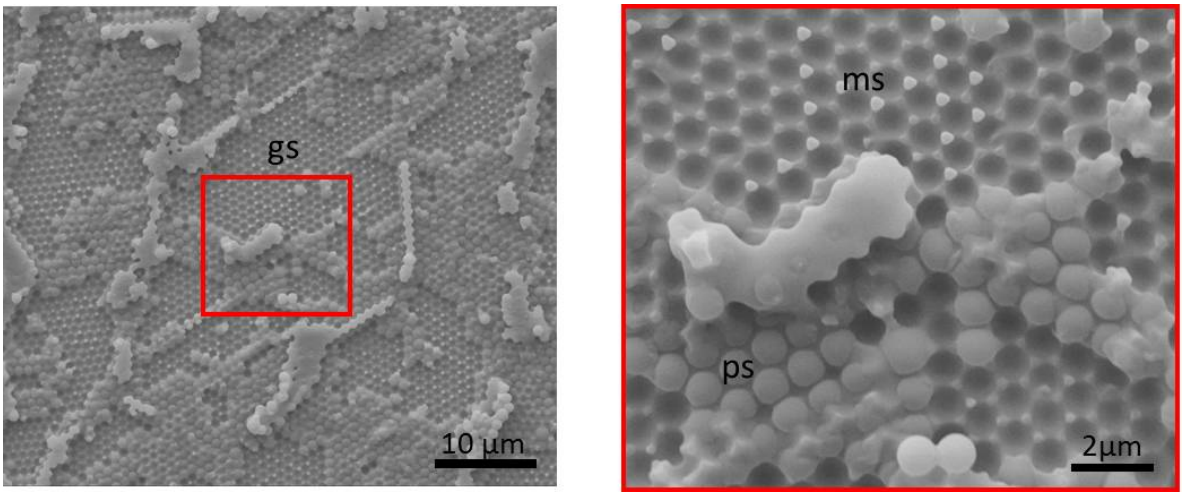

Figure 5.9: *PDMS molding: 1 µm PS particles deposited on oxygen plasma treated (50 W, 5 min) silicon surface, molded with PDMS and cured in an oven for 12 h. Particle-like structures (ps), golfball structures (gs) and mushroom shaped structures (ms) are visible.*

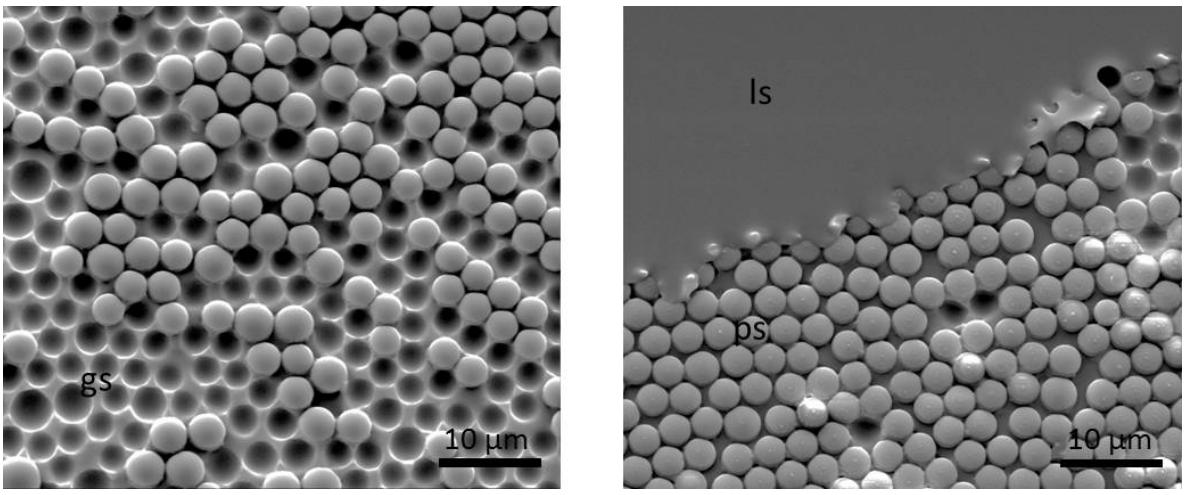

Figure 5.10: *PDMS molding: 3 µm PS particles deposited on an oxygen plasma treated (50 W, 5 min) silicon surface, molded with PDMS and cured in an oven for 12 h. Particle-like structures (ps), continous PDMS layer (ls) and golfball structures (gs) are visible.*

layer without any visible structures on the PDMS surface. In general particles with an original diameter of 0.5 µm and 1 µm showed better PDMS molding structures (especially golfball structures (gs) and mushroom shaped structures (ms)) than the other particle sizes. The skin surface of Isotoma saltans (presented in Figure 5.11) looks similar to the PDMS mushroom shaped structure. Such structures may have antiwetting and antiicing properties [193, 194].

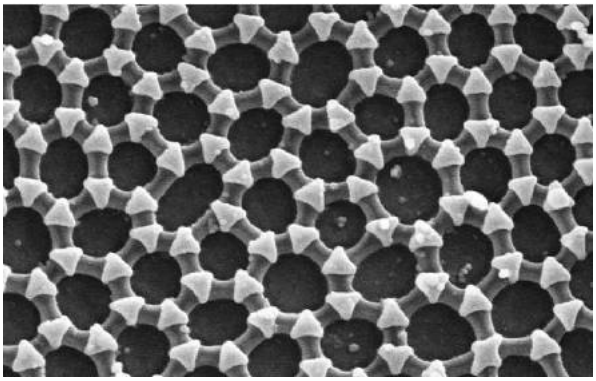

Figure 5.11: *Micro- and nanostructure of a springtail (Isotoma saltans) [195].*

5.6.2 Particle based softmolding of PS particles on a silicon substrate with a thin PS layer underneath

To enhance the connection between substrate and PS particles a PS layer was deposited on the silicon substrate. The PS particles, which were deposited on this thin (178 nm ± 8 nm) PS layer, were annealed in an oven (by 110 °C for 1 min 30 s) and treated with oxygen plasma (20 W, 10 min). Figure 5.12 presents little columns between PS particles and PS layer. The little columns have the same formation mechanism as the bridges between particles (shown in Subchapter 5.5.2). Annealing, results into bonds between the PS particles and PS layer. The reactive plasma converts the bonds into columns. The columns could present an additional possibility for polymers to flow under the particles and mold mushroom shaped structures.

To show the effect of columns between PS particles and PS layer, the structures were also softmolded by PDMS. The results are presented in Figure 5.13. The PDMS molding was treated with acetone to dissolve the PS particles. An ultrasonic bath treatment (15 min) was chosen to enhance the cleaning effect. On the left SEM picture of Figure 5.14 a hole structure is presented. But a field with golfball structures was also found. On the right SEM picture of

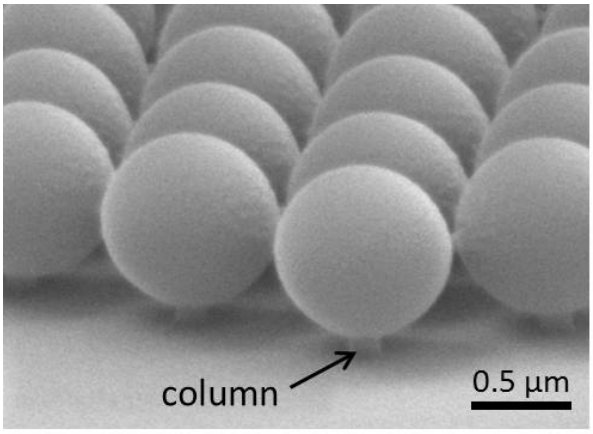

Figure 5.12: *SEM pictures (15 ° tilted) of PS particles with an origin diameter of 1 µm on silicon with a 140 nm PS layer, annealed in an oven at 110°C for 1 min 30 s.*

Figure 5.14, which were taken with a higher magnification. It was seen, that little droplets are coming out of some holes.

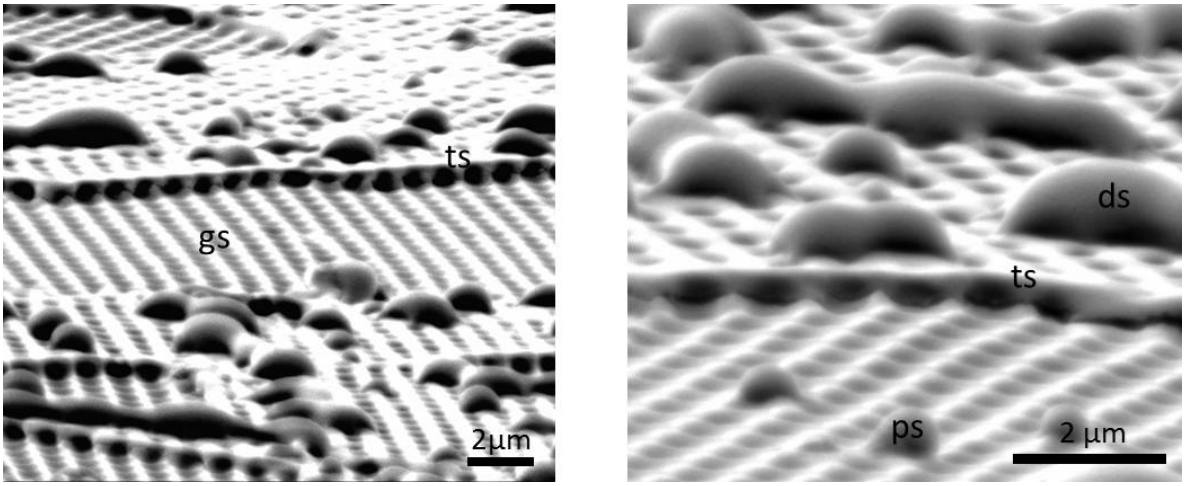

Figure 5.13: *SEM pictures (15 ° tilted) from PDMS molding of PS particles on a silicon wafer with a 178 nm PS layer, 24 h treatment with acetone and 15 min ultrasonic bath. The PDMS reacted on the sample for 24 h before it was cured. Particle-like structures (ps), drop-like structures (ds), golfball structures (gs) and tunnel structures (ts) are visible.*

The PDMS molding of the 'column structure' show that the PDMS can flow between the particles. This could be facilitated by the oxygen etching step (20 W, 10 min) which increases the gap between the particles. The PDMS reacted on the sample for 24 h before it was cured. This should ensure that the PDMS (high viscosity) has enough time to enclose the whole structures of the sample. Because the particles are on a PS column, the PDMS flow under the particles is fascilitated and enables flowing around the column. This explains the hole

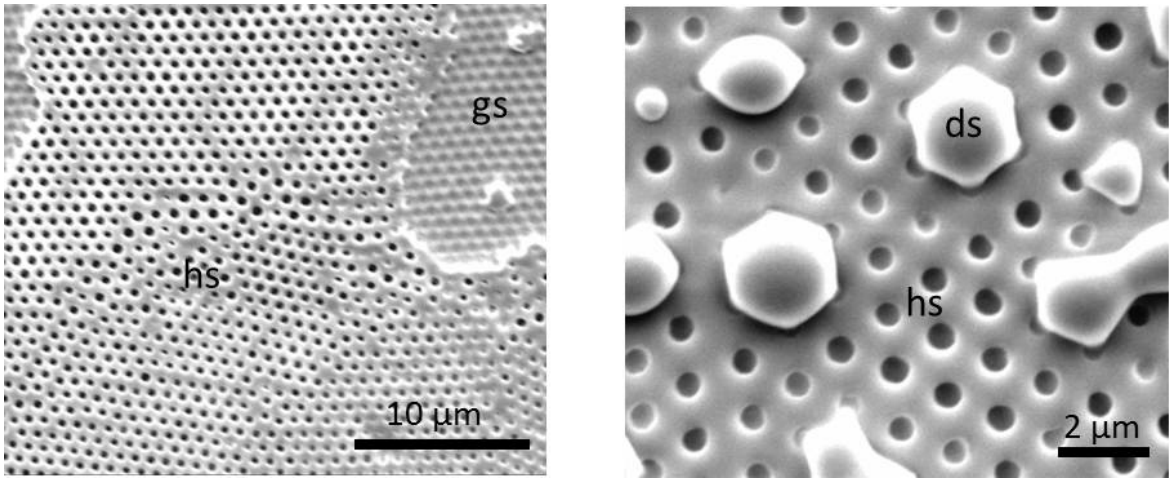

Figure 5.14: *SEM pictures from PDMS molding of PS particles on a silicon wafer with a 178 nm thick PS layer, annealed in the oven by 110 °C for 2 min, oxygen plasma etched 20 W 10 min, the molding was treated with acetone for 24 h and 15 min in ultrasonic bath. The PDMS reacted on the sample for 24 h before it was cured. Drop-like structures (ds), golfball structures (gs) and hole structures (hs) are visible.*

structure (hs). In a tilted SEM structure it was shown that the particles were under the hole structure. Acetone was used to dissolve the PS. Sometimes golfball structures (gs) were also observed. This could be the result of breaking of the thin bars of tunnel structures during the peeling off process and rupture of a part of the structure. The drops found on a hole structure are PS. PS swells when it comes in contact with the solvent acetone and is swelling out of the hole structure (hs). But it was also shown that the combination of acetone (24 h) and ultrasonic treatment (15 min) were not enough to remove completely the PS. Furthermore, the vibration of the ultrasonic treatment can also damage thin PDMS structures and destroy hole-structures.

5.6.3 Adhesion experiments using particle softmolded PDMS structures

In Figure 5.6.3 the adhesion experiments on different PDMS moldings of particle monolayers are presented. The measurements were taken with a glass sphere with a diameter of 4 mm. Spherical substrates were independent of misalignment angle [133] and facilitate the measurements with the presented small sample structures. The preload curves were measured and the saturation value of the pull-off forces was determined. This was necessary because in general the contact area of a spherical probe varies with preload and the adhesion values depend on the contact

area. Measurements on three different spots were conducted with the prior determined preload force. For the calculations of the 'apparent' adhesive strength, the apparent contact area was chosen as 3.70 mm^2, a roughly average value of all measurements. On each spot a total number of 15 measurements were carriet out. It was measured on a flat PDMS sample, designated as reference, and on PDMS moldings of particle monolayers of particles with an original diameter of 0.25 µm, 0.5 µm, 1 µm and 3 µm. The '1 µm*' PDMS sample describes the PDMS molding of particles on a thin PS layer and is treated 24 h with acetone and 15 min with ultrasonic.

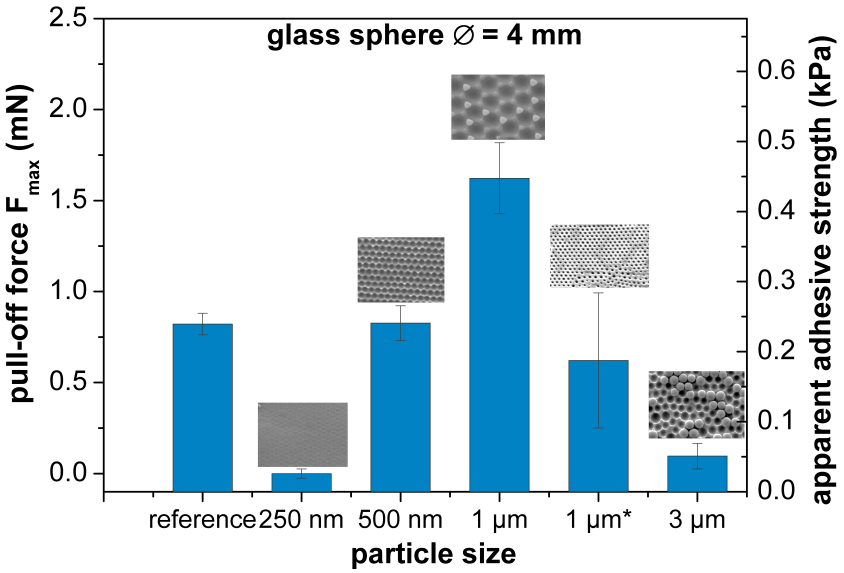

Figure 5.15: *Pull-off forces* F_{max} *and the corresponding 'apparent' strength values, measured on PDMS moldings of particle monolayers of 0.25 µm, 0.5 µm, 1 µm, 3 µm particles deposited on silicon and measured on PDMS molding of particle monolayer of 1 µm* particles deposited on a thin PS layer, treated 24 h with acetone and 15 min with ultrasonic. The reference is a flat PDMS layer. The characteristic appearance of the structure is inserted as a SEM picture for each sample.*

The adhesion of the 1 µm sample showed the highest pull-off force with 1.6 mN, that is twice than the reference. The 0.5 µm sample showed pull-off forces in the range of the reference sample. The 0.25 µm and 3 µm sample showed anti-adhesive properties with pull-off forces of nearly 0 mN. The 1 µm* PDMS sample showed a quarter less pull-off force than the 1 µm sample but also a high standard deviation which indicates a variation in the measured spots caused by non-uniform structure.

The 1 µm PDMS sample showed the best adhesion. One reason is probably the high presence of mushroom shaped structures (ms). The 0.5 µm PDMS sample showed half of the pull-off forces of the 1 µm PDMS sample in the range of the reference. Although the sample shows also presence of mushroom shaped structures (ms) the contact area with the spherical indenter is probably smaller and thus the adhesion is lower. The 0.25 µm and 3 µm sample showed the lowest pull-off forces. One reason could be the big areas of particle-like structures which consists of PS particles coated with PDMS or uncoated PS particles. Because PS particles are stiff in comparison to PDMS the adhesion ability decreases. The 1 µm* PDMS sample showed lower pull-off forces than the 1 µm PDMS sample. The hole structures (hs) and the drops which swell out of the holes could have a negative impact on adhesion which explains the difference to the 1 µm PDMS sample.

The results confirm the expections that material structuring by molding of particles can increase the adhesion in comparison to the reference sample (flat PDMS) [129] but only under certain conditions. For the softmolding of 1 µm particles the fabrication conditions were ideal and a high presence of mushroom shaped structures could be obtained. Only this sample showed increased adhesion in comparison to the reference. Particles and drops on the surface leads to reduced adhesion.

5.7 Summary and Conclusion

In the first part of this article, the particle size evolution in dense and sparse layers of PS spheres during oxygen plasma etching was reported. Initial particle sizes and plasma power were systematically varied. Particles in both dense and sparse layers exhibited size evolutions that do not agree with relations previously used to describe the etching. It was shown that a fit of the time-dependant particle size with a simple linear relation is sufficient for technical applications and fits the data at least as well as other, more complicated relations. It is concluded that the exact etch mechanism is more complex than assumed in deriving the simple models that have been used so far.

In the second part of this article, we discuss the shape changes during etching that occur both on a single-particle level and on the level of the ordered particle monolayer. Particles

increasingly deviate from their original spherical shape. In dense layers, bridges develop between the particles at their original contact points with each other. These bridges retain the relative position of particles. Their eventual breakage after further etching leads to a loss of order. In sparse layers, particles do not form bridges but deviate from their spherical shape in a more symmetrical fashion.

Rational tuning of etching power and times, possibly combined with an optimized shape of the plasma, can be used to create polymer structures beyond smaller spheres when starting from self-assembled monolayers of polymer particles. Such processing can open up new fields of application with low-cost, high-precision templates.

The particle based softmolding of PS particles on a silicon surface was partially effective. The problem is that the PDMS samples were not homogeneous so that there are different structured areas. The adhesion measurements showed that most of the structured samples are more anti-adhesive than adhesive. The expection was that the molded structures are more uniform and perform higher adhesion than the reference sample due to their structured surface [129].[5]

[5]This paragraph is not content of C. T. Bauer, A. Wonn, D. Brodoceanu, P. Born, E. Kroner, and T. Kraus, Size and shape evolution of PS particle layers during etching, *Bioinspired, Biomimetic and Nanomaterials*, 2:130–140, 2013 [3].

Supporting Information

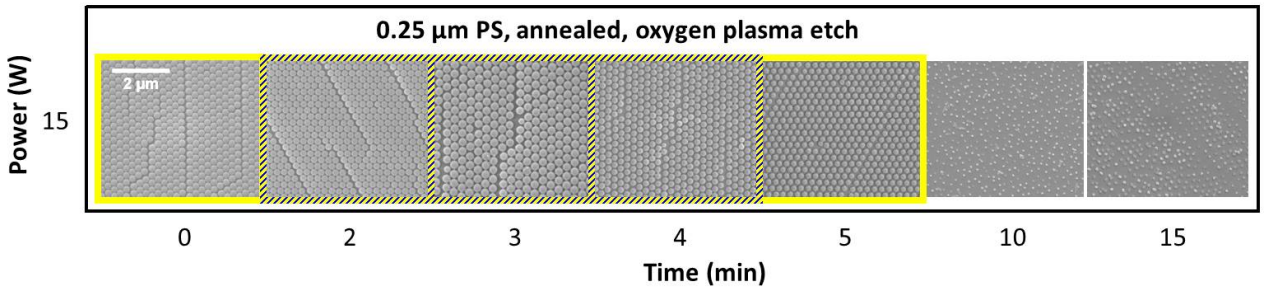

Figure B1: *Electron micrographs of PS particle monolayers etched for different times (original particle diameter: 0.25 µm). Samples, where ordered was retained, are marked with a yellow border; samples that retained order and developed bridges between particles are marked wit a yellow-blue border. The scale bar is 2 µm and applies to all pictures.*

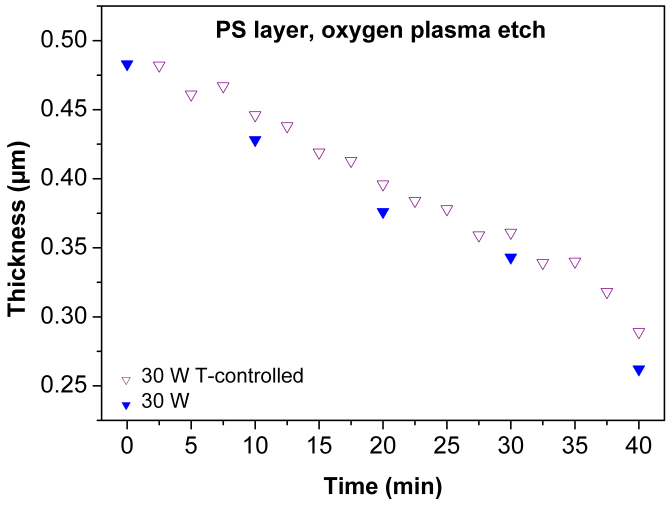

Figure B2: *Time-dependent thickness of a PS layer etched at 30 W plasma power in continous and intermittent operation.*

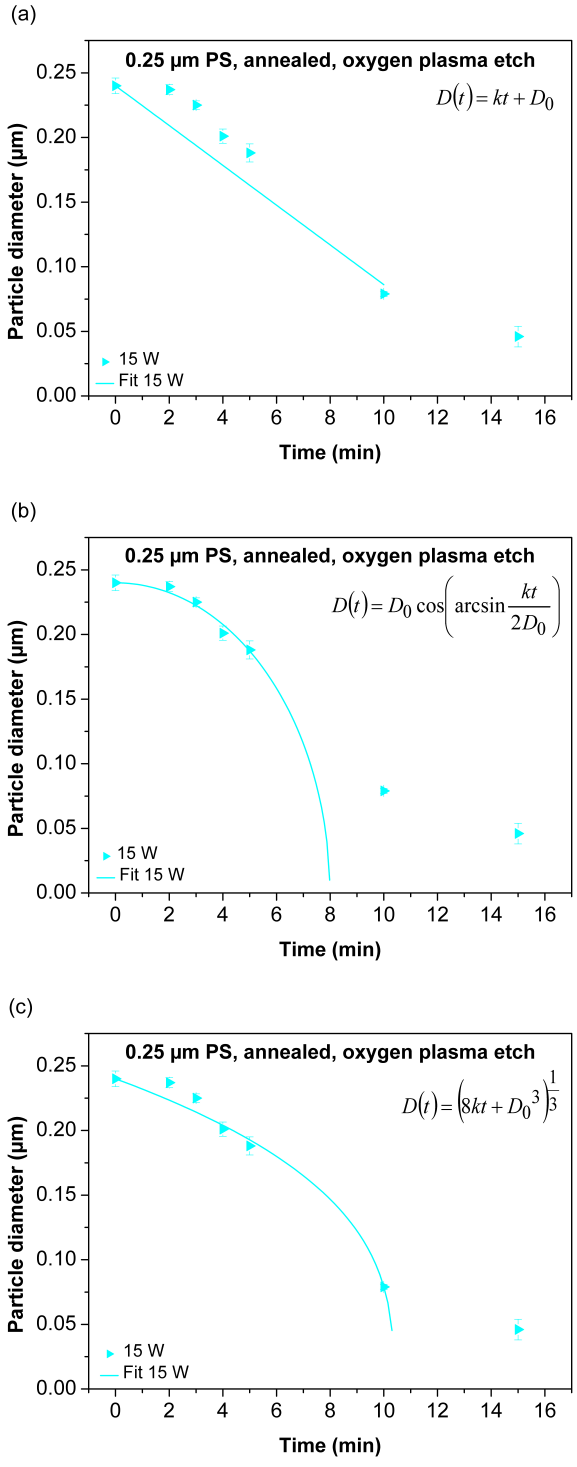

Figure B3: *Time dependence of size reduction for dense PS particle layers with an original diameter of 0.25 µm by different powers of oxygen plasma etching, fitted by the (a) Linear, (b) Spherical cap and (c) Constant volume loss relations.*

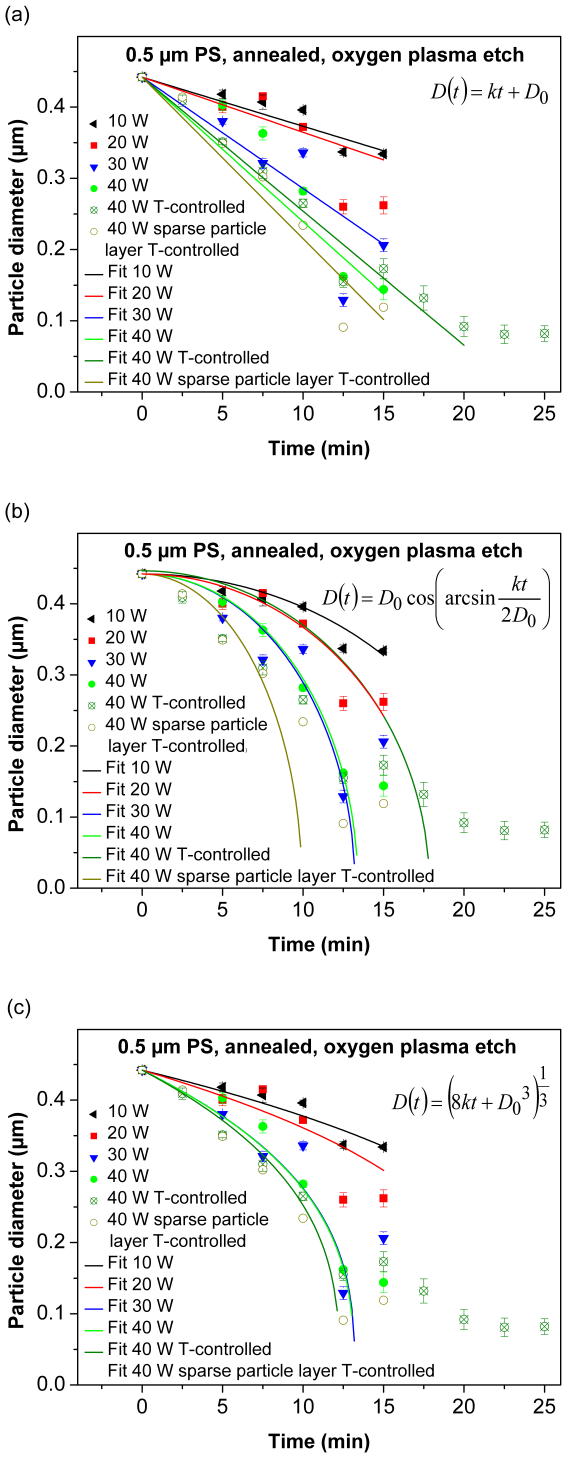

Figure B4: *Time dependence of size reduction for dense and sparse PS particle layers with an original diameter of 0.5 µm by different powers of oxygen plasma etching partially with T-controlled, fitted by the (a) Linear, (b) Spherical cap and (c) Constant volume loss relations.*

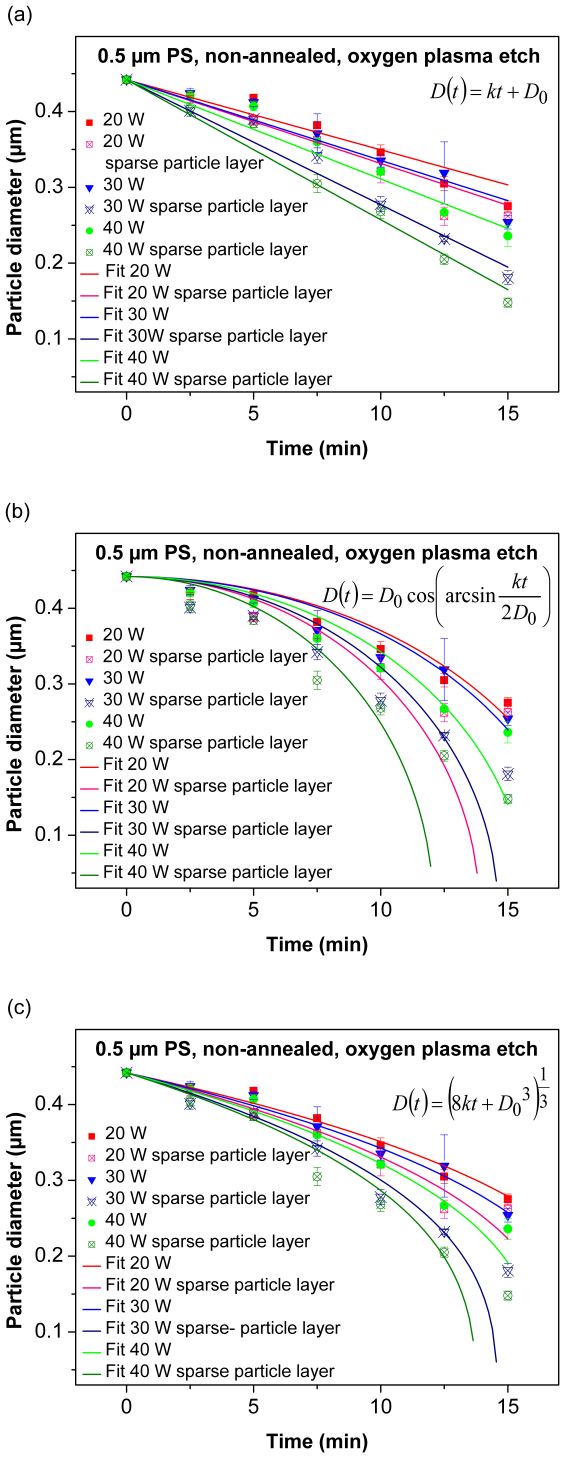

Figure B5: *Time dependence of size reduction for dense and sparse PS particle layers with an original diameter of 0.5 µm non-annealed by different powers of oxygen plasma etching, fitted by the (a) Linear, (b) Spherical cap and (c) Constant volume loss relations.*

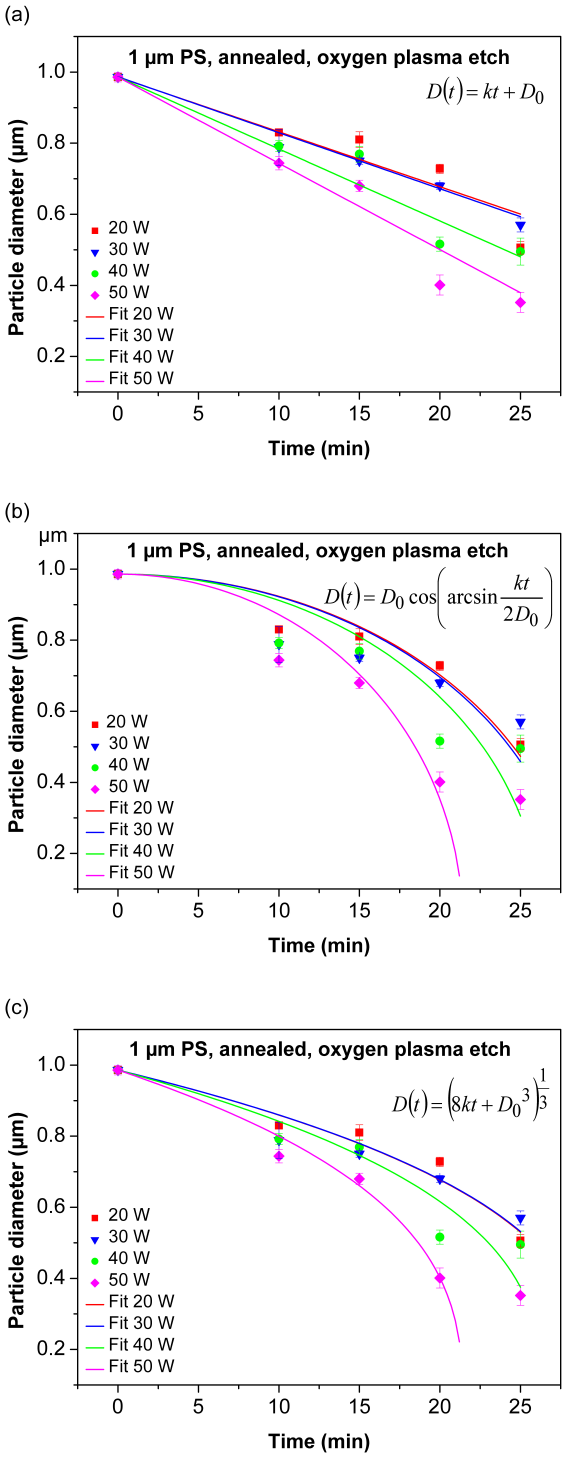

Figure B6: *Time dependence of size reduction for dense PS particle layer with an original diameter of 1 µm by different powers of oxygen plasma etching, fitted by the (a) Linear, (b) Spherical cap and (c) Constant volume loss relations.*

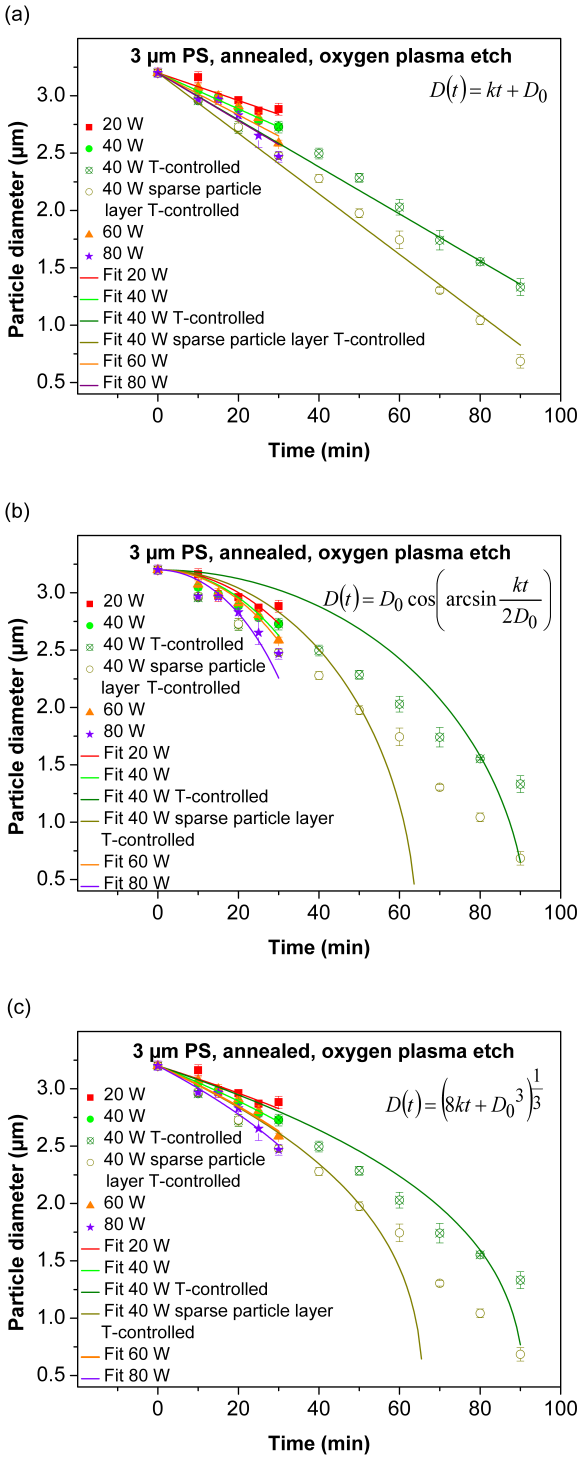

Figure B7: *Time dependence of size reduction for dense PS particle layer with an original diameter of 3 µm by different powers of oxygen plasma etching, fitted by the (a) Linear, (b) Spherical cap and (c) Constant volume loss relations.*

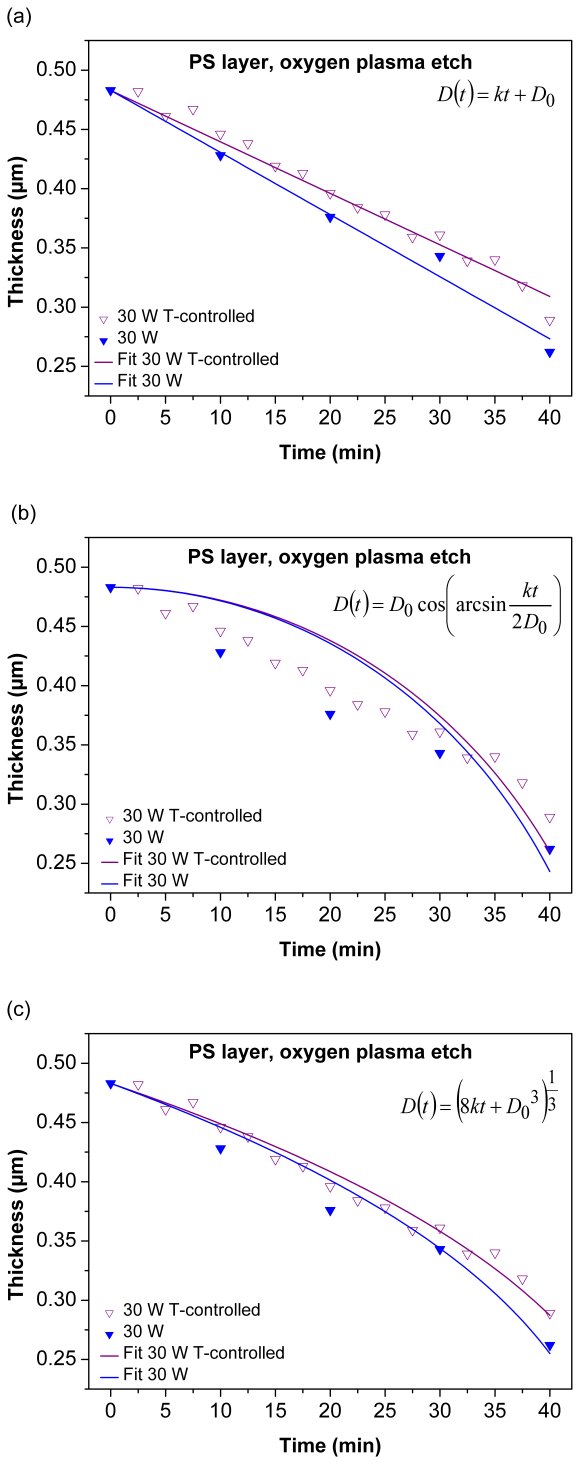

Figure B8: *Time dependence of the thickness of the PS layer with and without T-control, fitted by the (a) Linear, (b) Spherical cap and (c) Constant volume loss relations.*

Table B1: *Overview on the appearance of dense-packed PS particles with an original diameter of 0.25 µm after oxygen plasma treatment; abbreviations: H (hexagonal order), B (bridges), HB (hexagonal order and bridges) XX (neither hexagonal order nor bridges).*

0.25 µm PS particles

(min)	0	2	3	4	5	10	15
15 W	H	HB	HB	HB	H	XX	XX

Table B2: *Overview of the appearance of dense-packed, T-controlled (T) and sparse packed and T-controlled (ST) PS particles with a starting diameter of 0.5 µm after oxygen plasma treatment; abbreviations: H (hexagonal order), B (bridges), HB (hexagonal order and bridges), XX (neither hexagonal order nor bridges), – (not measured).*

0.5 µm PS particles

(min)	0	2.5	5	7.5	10	12.5	15	17.5	20	22.5	25
40 W (T)	H	HB	HB	XX	XX	XX	XX	XX	XX	XX	XX
40 W (ST)	XX	XX	XX	XX	XX	XX	XX	–	–	–	–
40 W	H	–	H	H	H	XX	XX	–	–	–	–
30 W	H	–	HB	H	H	XX	XX	–	–	–	–
20W	H	–	HB	HB	H	H	H	–	–	–	–
10 W	H	–	HB	HB	HB	HB	HB	–	–	–	–

Table B3: *Overview of the appearance of dense-packed PS particles with a starting diameter of 1 µm after oxygen plasma treatment; abbreviations: H (hexagonal order), B (bridges), HB (hexagonal order and bridges), XX (neither hexagonal order nor bridges), – (not measured).*

1 µm PS particles

(min)	0	10	15	20	25
50 W	H	HB	H	XX	XX
40 W	H	HB	H	XX	XX
30 W	H	HB	HB	XX	XX
20 W	H	HB	HB	H	H

Table B4: *Overview of the appearance of dense-packed, T-controlled (T) and sparse packed and T-controlled (ST) PS particles with a starting diameter of 3 µm after oxygen plasma treatment; abbreviations: H (hexagonal order), B (bridges), HB (hexagonal order and bridges), XX (neither hexagonal order nor bridges), – (not measured).*

3 µm PS particles

(min)	0	10	15	20	25	30	40	50	60	70	80	90
80 W	H	HB	HB	XX	XX	XX	–	–	–	–	–	–
60 W	H	HB	HB	HB	XX	XX	–	–	–	–	–	–
40 W (T)	H	HB	–	HB	–	HB	XX	XX	XX	XX	XX	XX
40 W (ST)	XX	XX	–	XX	–	XX	XX	XX	XX	XX	XX	XX
40 W	H	HB	HB	H	XX	XX	–	–	–	–	–	–
20 W	H	HB	HB	H	XX	XX	–	–	–	–	–	–

6 Summary and Outlook

Over the last years scientists have concentrated on the fabrication of single-level gecko-inspired dry adhesives with great success. They also developed theoretical models to predict and describe the adhesion ability of such structures. Although there have been some attempts in fabrication of bioinspired hierarchical adhesives, they mostly have been tested on smooth surfaces. Consequently, conclusions about the role of hierarchy on the adhesion to surfaces could not be drawn from these experimental studies. Yet, the fundamental understanding of hierarchy is crucial to develop bioinspired adhesives with hierarchical structures.

Within a project funded by the German Science Foundation (DFG) within the framework of SPP 1420 ('Biomimetic Materials Research: Functionality by Hierarchical Structuring of Materials'), two topics were adressed, which are presented in this thesis. The first topic focusses on hierarchical macroscopic adhesives and their adhesive performances on smooth and rough surfaces. The second topic focusses on new fabrication methods which allow fabrication of micropatterned hierarchical surfaces and at the same time can be combined with current state of the art patterning methods.

As defined in Section 2.9, several questions resulted from the analysis of literature and will be summarized in the following:

- Is it possible to fabricate a hierarchical fibrillar model with different hierarchy levels ranging several orders of magnitude in size?

In Chapter 4 hierarchical structures were fabricated with three different hierarchy levels in the millimeter range with and without mushroom tips. To reduce the parameter space, the different hierarchy levels were fixed to one aspect ratio, i. e. aspect ratio 4. The advantage of

the macroscopic model was that it facilitated fabrication and observation of model-substrate interaction.

- Is it possible to better understand the contact formation and deformation phenomena-like, buckling, and adhesion behavior of a hierarchical structure?

- Which influence has micro- and macroroughness on buckling and adhesion of hierarchical structures?

With the macroscopic model adhesion and buckling measurements were performed with all level combinations (HL1, HL2 and HL3) with and without mushroom shaped tips on flat smooth glass, flat rough aluminum and wavy rough aluminum. Buckling occurred when the preload was sufficiently high. The buckling preload of a single hierarchy level HL1 on a flat smooth substrate was about 4 times higher than for hierachy levels HL2 and HL3 and could be explained by the change in the buckling mode with structural hierarchy. The mushroom shaped structures show buckling load values similar to flat tip structures. Presence of microroughness had negligible effects on the buckling performance, in contrast to macroroughness. The results confirmed that the buckling behavior depends on the substrate topography. In addition it was shown that the presence of micro- and macroroughness of the substrate decreased adhesion. The effect of microroughness could be reasonably well explained by the model of Fuller and Tabor [33].

- Does the introduction of a hierarchy to a structure lead to a benefit in its adhesive performance?

The adhesion measurements showed that hierarchical structures tend to show lower adhesion performance compared to single level structures if tested against a flat substrate. One explanation could be that the hierarchical samples need higher preloads to adapt to the substrate (adaptation to micro- and nanoroughness). But a high preload cannot be achieved due to buckling which would lead to a loss in tip contact.

The second topic, focussed on new fabrication methods (see Chapter 5), raised following questions:

- Is it possible to find a new route to fabricate small structures (down to nanometer range) which allow large scale patterning at the same time?

Crystalline particle monolayers are promising for colloidal lithography and particle based softmolding to fabricate (hierarchical) biomimetic materials which can also be combined with bigger structures. It was investigated how the particle size and interparticle distance can be tuned. PS particle monolayers were etched with different initial particle diameters (250 nm, 500 nm, 1 µm and 3 µm) by oxygen plasma. The particle diameter decreased with increasing etching power and time. The structures obtained were molded with a polymer (PDMS) or could serve as etching masks.

- Is it possible to influence micropatterned molds for fabrication of bioinspired adhesives by systematically evaluate the etching process of particles depending on particle size, plasma power, etching time, particle density?

Initial particle sizes and plasma power were systematically varied. The size evolution of individual particles was analyzed using scanning electron microscopy. Also the influence of particle density was investigated. The results were compared with different etch models. The literature reported from a linear and a cos (arc sin) relation for the etching behavior dependent on time and etch power. Based on the experimental results, a new model for the etching behavior was developed. It was shown that the etch mechanism is more complex than assumed so far, so it is unclear which specific physical processes occur. However, it was possible to show that all three fits can be used for a reasonably good prediction of the PS particle diameter. An exact prediction of the particle diameter was not possible, due to the inhomogeneity of the plasma etching process. Furthermore the shape changes of the PS particles during the etch process in oxygen plasma were investigated. In dense particle monolayers, bridges developed between particles at their original contact points. The bridges retained the relative position of the ordered particle array. Breakage of the bridges after extensive etching led to a loss of order. With increasing etching time and power, particles increasingly deviated from their original spherical shape. In sparse arrays, the particles could not form bridges. After etching, they deviated from their spherical shape in a more symmetrical way.

- Is it possible to mold particle based templates to obtain adhesive structures?

Particle based softmolding of PS particle (250 nm, 500 nm, 1 µm and 3 µm) monolayers on a silicon substrate with PDMS was performed. Molding from the self-assembled PS particle arrays on PS coated silicon substrates was also done. It was shown that under certain conditions, arrays of circular dimpled structures (golfball structures) were fabricated. But the desired mushroom shaped structures could not be produced on very large areas. The adhesion measurements showed that the structuring by molding of particles can increase the adhesion in comparison to the reference sample (flat PDMS) under certain conditions. For the softmolding of 1 µm particles the fabrication conditions were ideal and a high presence of mushroom shape structures could be obtained. This sample showed increased adhesion in comparison to the reference sample without sructures. The other molding samples showed more anti-adhesive than adhesive properties. It is assumed that the fabrication conditions were not ideal and the moldings were not homogenous over large areas.

-Outlook- To develop an optimum design of hierarchical fibrillar adhesive surfaces, the compressive and adhesive behavior should be considered. For different degrees of roughness different design strategies have to be applied. It is proposed that experiments with different aspect ratios of each level of hierarchy and different substrates with variance in wavelength and heights should be performed. Experiments with stiffness gradients in pillars would be also interesting. Pillars fabricated from materials stiffer than PDMS are expected to have lower propensity of buckling. In addition it would be useful to measure the shear forces of the hierarchical structures. Further it should be tried to improve the softmolding fabrication process to produce larger areas with defined adhesive structures. In addition to softmolding of particle monolayers, the particle sizes could be reduced and the gaps between them could serve as an etching mask. A combination of macroscopic, microscopic and nanoscopic structures would be also conceivable. The results from Chapter 4 and Chapter 5 could be combined to fabricate hierarchical structures to adapt to several scales of substrate roughness.

List of Figures

List of Tables

Bibliography

[1] E. Arzt, S. Enders, and S.Gorb. Towards a micromechanical understanding of biological surface devices. *Z. Metallkd.*, 93:345–351, 2002.

[2] C. T. Bauer, E. Kroner, N. A. Fleck, and E. Arzt. Hierarchical macroscopic fibrillar adhesives: in-situ study of buckling and adhesion mechanisms on wavy substrates. *accepted for publication in Bioinspiration Biomimetics*, 2015.

[3] C. T. Bauer, A. Wonn, D. Brodoceanu, P. Born, E. Kroner, and T. Kraus. Size and shape evolution of PS particle layers during etching. *Bioinspired, Biomimetic and Nanomaterials*, 2:130–140, 2013.

[4] H. Hertz. Über die Berührung fester elastischer Körper. *J. reine angew. Math.*, 92:156–171, 1882.

[5] D. Maugis. *Contact, adhesion and rupture of elastic solids.* Springer, Berlin, Heidelberg, New York, p. 203–343, 2000.

[6] K. L. Johnson, K. Kendall, and A. D. Roberts. Surface energy and the contact of elastic solids. *Proc. R. Soc. Lond. A.*, 324:301–313, 1971.

[7] K. Kendall. PhD thesis, Cambridge University (UK), 1969.

[8] A. D. Roberts. PhD thesis, Campridge University (UK), 1968.

[9] B. V. Derjaguin, V. M. Muller, and Y. P. Toporov. Effect of contact deformations on the adhesion of particles. *J. Colloid Interface Sci.*, 53:314–326, 1975.

[10] D. Tabor. Surface forces and surface interactions. *J. Colloid Interface Sci.*, 58:2–13, 1977.

[11] E. Gnecco and E. Meyer, editors. *Fundamentals of friction and wear on the nanoscale.* Springer, Cham, Heidelberg, New York, Dordrecht, London, p. 91, 2007.

[12] Elmar K. Kroner. *Adhesion measurements on patterned elastomeric surfaces.* PhD thesis, Saarland University, Leibniz Institute for New Materials, 2011.

[13] E. Arzt, S. Gorb, and R. Spolenak. From micro to nano contacts in biological attachment devices. *PNAS*, 100:10603–10606, 2003.

[14] E. Arzt. Biological and artificial attachment devices: Lessons for material scientists from flies and geckos. *Mater. Sci. Eng. C*, 26:1245–1250, 2006.

[15] J.-H. Dirks and W. Federle. Fluid-based adhesion in insects - principles and challenges. *Soft Matter*, 7:11047–11053, 2011.

[16] B. N. J. Persson. Biological adhesion for locomotion on rough surfaces: Basic priciples and a theorist's view. *MRS Bull.*, 32, 2007.

[17] W. R. Hansen and K. Autumn. Evidence for self-cleaning in gecko setae. *PNAS*, 102:385–389, 2005.

[18] T. W. Kim and B. Bhushan. Effect of stiffness of multi-level hierarchical attachment system on adhesion. *Ultramicroscopy*, 107:902–912, 2007.

[19] B. Zhao, N. Pesika, H. Zeng, Z. Wei, Y. Chen, K. Autumn, K. Turner, and J. Israelachvili. Role of tilted adhesion fibrils (setae) in the adhesion and locomotion of gecko-like systems. *J. Phys. Chem. B*, 113:3615–3621, 2009.

[20] T. S. Kustandi, V. D. Samper, W. S. Ng, A. S. Chong, and H. Gao. Fabrication of a gecko-like hierarchical fibril array using a bonded porous alumina template. *J. Micromech. Microeng.*, 17:N75–N81, 2007.

[21] C. J. van Oss. *Interfacial forces in aqueous media.* Taylor & Francis Group, Boca Raton, p. 1-2, 2006.

[22] J. N. Israelachvilli. *Intermolecular and surface forces.* Academic, San Diego, 2nd edition, p. 276, 1992.

[23] H. C. Hamaker. The London-Van der Waals attraction between spherical particles. *Physica IV*, 10:1058–1072, 1937.

[24] R. A. Sauer. Multiscale modelling and simulation of the deformation and adhesion of a single gecko seta. *Computer Methods in Biomechanics and Biomedical Engineering*, 12:627–640, 2009.

[25] T. W. Kim and B. Bhushan. The adhesion model considering capillarity for gecko attachment system. *J. R. Soc. Interface*, 5:319–327, 2007.

[26] L.-F. Wang, W.-B. Rong, L.-N. Sun, L.-G. Chen, and B. Shao. Capillary forces between submillimeter spheres and flat surfaces at constant liquid volumes. *Chin. Phys. Lett.*, 26:126801, 2009.

[27] F. M. Orr, L. E. Scriven, and A. P. Rivas. Pendular rings between solids-meniscus properties and capillary force. *J. Fluid Mech.*, 67:723–742, 1975.

[28] K. Autumn and A. M. Paettie. Mechanisms of adhesion in geckos. *Integr. Comp. Biol.*, 42:1081–1090, 2002.

[29] K. Autumn, M. Sitti, Y. A. Liang, A. M. Paettie, W. R. Hansen, S. Sponberg, T. W. Kenny, R. Fearing, J. N. Israelachvili, and R. J. Full. Evidence for van der Waals adhesion in gecko setae. *PNAS*, 99:12252–12256, 2002.

[30] K. Autumn. How gecko toes stick. *American Scientist*, 94:124–132, 2006.

[31] G. Huber, H. Mantz, R. Spolenak, K. Mecke, K. Jacobs, S. N. Gorb, and E. Arzt. Evidence for capillarity contributions to gecko adhesion from single spatula nanomechanical measurements. *PNAS*, 102:16293–16296, 2005.

[32] W. Sun, P. Neuzil, T. S. Kustandi, S. Oh, and V. D. Samper. The nature of the gecko lizard adhesive forces. *Biophys. J.: Biophys. Lett.*, 89:L14–L17, 2005.

[33] K. N. G. Fuller and D. Tabor. The effect of surface roughness on the adhesion of elastic solids. *Proc. R. Soc. Lond. A*, 345:327–342, 1975.

[34] J. A. Greenwood. Constriction resistance and the real area of contact. *Brit. J. Appl. Phys.*, 17:1621–1632, 1966.

[35] B. N. J. Persson and E. Tosatti. The effect of surface roughness on the adhesion of elastic solids. *J. Chem. Phys.*, 115:5597–5610, 2001.

[36] N. E. Stork. Experimental analysis of adhesion of chrysolina polita (chrysomelidae: choleoptera) on a variety of surfaces. *J. Exp. Biol.*, 88:91–107, 1980.

[37] O. Betz. Performance and adaptive value of tarsal morphology in rove beetles of the genus stenus (coloptera, staphylinidae). *J. Exp. Biol.*, 205:1097–1113, 2002.

[38] E. V. Gorb and S. N. Gorb. Attachment ability of the beetle chrysolina fastuosa on various plant surfaces. *Entomol. Exp. Appl.*, 105:13–28, 2002.

[39] E. Gorb, K. Haas, A. Henrich S. Enders, N. Barbakadze, and S. Gorb. Composite structure of the crystalline epicuticular wax layer of the slippery zone in the pitchers of the carnivorous plant nepenthes alata and its effect on insect attachment. *J. Exp. Biol.*, 208:4651–4662, 2005.

[40] B. N. J. Persson and S. Gorb. The effect of surface roughness on the adhesion of elastic plates with application to biological systems. *J. Chem. Phys.*, 119:11437, 2003.

[41] G. Huber, S. Gorb, N. Hosoda, R. Spolenak, and E. Arzt. Influence of surface roughness on gecko adhesion. *Acta Biomater.*, 3:607–610, 2007.

[42] J. Davies, S. Haq, T. Hawke, and J. P. Sargent. A practical approach to the development of a synthetic gecko tape. *Int. J. Adhes. Adhes.*, 29:380–390, 2009.

[43] S. Vajpayee, A. Jagota, and C. Y. Hui. Adhesion of a fibrillar interface on wet and rough surfaces. *J. Adhesion*, 86:39–61, 2010.

[44] H. E. Jeong, J.-K. Lee, H. N. Kim, S. H. Moon, and K. Y. Suh. A nontransferring dry adhesive with hierarchical polymer nanohairs. *PNAS*, 106:5639–5644, 2009.

[45] N. Cañas, M. Kampermann, B. Völker, E. Kroner, R. M. McMeeking, and E. Arzt. Effect of nano- and micro-roughness on adhesion of bioinspired micropatterned surfaces. *Acta Biomater.*, 8:282–288, 2012.

[46] E. Kroner, J. Blau, and E. Arzt. Note: An adhesion measurement setup for bioinspired fibrillar surfaces using flat probes. *Rev. Sci. Instrum.*, 83:016101, 2012.

[47] Y. Zhao, T. Tong, L. Delzeit, A. Kashani, M. Meyyappan, and A. Majumdar. Interfacial energy and strength of multiwalled-carbon-nanotube-based dry adhesive. *J. Vac. Sci. Technol. B*, 24:331–335, 2006.

[48] B. Yurdumakan, N. R. Raravikar, P. M. Ajayan, and A. Dhinojwala. Synthetic gecko foot-hairs from multiwalled carbon nanotubes. *Chem. Commun.*, 30:3799–3801, 2005.

[49] N. J. Glassmaker, A. Jagota, and C.-Y. Hui. Adhesion enhancement in a biomimetic fibrillar interface. *Acta Biomater.*, 1:367–375, 2005.

[50] A. K. Geim, S. V. Dubonos, I. V. Grigorieva, K. S. Novoselov, A. A. Zhukov, and S. YU. Shapoval. Microfabricated adhesive mimicking gecko foot-hair. *Nat. Mater.*, 2:461–463, 2003.

[51] B. Aksak, M. P. Murphy, and Metin Sitti. Adhesion of biologically inspired vertical and angled polymer microfiber arrays. *Langmuir*, 23:3322–3332, 2007.

[52] E. Cheung and M. Sitti. Adhesion of biologically inspired oil-coated polymer micropillars. *J. Adhes. Sci. Technol.*, 22:569–589, 2008.

[53] A. J. Crosby, M. Hageman, and Andrew Duncan. Controlling polymer adhesion with 'pancakes'. *Langmuir*, 21:11738–11743, 2005.

[54] A. del Campo, C. Greiner, I. Álvarez, and E. Arzt. Patterned surfaces with pillars with controlled 3d tip geometry mimicking bioattachment devices. *Adv. Mater.*, 19:1973–1977, 2007.

[55] N. J. Glassmaker, A. Jagota, C. Y. Hui, and J. Kim. Design of biomimetic fibrillar interfaces: 1. making contact. *J. R. Soc. Interface*, 1:23–33, 2004.

[56] N. J. Glassmaker, A. Jagota, C.-Y. Hui, W. L. Norderer, and M. K. Chaudhury. Biologically inspired crack trapping for enhanced adhesion. *PNAS*, 104:10786–10791, 2007.

[57] C. Greiner, A. del Campo, and E. Arzt. Adhesion of bioinspired micropatterned surfaces: Effects of pillar radius, aspect ratio, and preload. *Langmuir*, 23:3495–3502, 2007.

[58] D. S. Kim, H. S. Lee, J. Lee, S. Kim, K.-H. Lee, W. Moon, and T. H. Kwon. Replication of high-aspect-ratio nanopillar array for biomimetic gecko foot-hair prototype by UV nano embossing with anodic aluminum oxide mold. *Microsyst. Technol.*, 13:601–606, 2007.

[59] S. Kim, M. Sitti, C. Y. Hui, R. Long, and A. Jagota. Effect of backing layer thickness on adhesion of single-level elastomer fiber arrays. *Appl. Phys. Lett.*, 91:161905, 2007.

[60] M. P. Murphy, B. Aksak, and M. Sitti. Adhesion and anisotropic friction enhancements of angled heterogeneous micro-fiber arrays with spherical and spatula tips. *J. Adhesion Sci. Technol.*, 21:1281–1296, 2007.

[61] A. Peressadko and S. N. Gorb. When less is more: Experimental evidence for tenacity enhancement by division of contact area. *J. Adhesion*, 80:1–15, 2004.

[62] T. Thomas and A. J. Crosby. Controlling adhesion with surface hole patterns. *J. Adhesion*, 82:311–329, 2006.

[63] M. Jin, X. Feng, L. Feng, T. Sun, J. Zhai, T. Li, and L. Jiang. Superhydrophobic aligned polystyrene nanotube films with high adhesive force. *Adv. Mater.*, 17:1977–1981, 2005.

[64] M. Sitti and R. S. Fearing. Synthetic gecko foot-hair micro/nano-structures as dry adhesives. *J. Adhes. Sci. Technol.*, 17:1055–1073, 2003.

[65] M. T. Northen and K. L. Turner. A batch fabricated biomimetic dry adhesive. *Nanotechnology*, 16:1159–1166, 2005.

[66] M. T. Northen and K. L. Turner. Meso-scale adhesion testing of integrated micro- and nano-scale structures. *Sens. Actuators, A*, 130-131:583–587, 2006.

[67] C.-Y. Hui, N. J. Glassmaker, T. Tang, and A. Jagota2. Design of biomimetic fibrillar interfaces: 2. Mechanics of enhanced adhesion. *J. R. Soc. Interface*, 1:35–48, 2004.

[68] T. S. Kustandi, V. D. Samper, D. K. Yi, W. S. Ng, P. Neuzil, and W. Sun. Self-assembled nanoparticles based fabrication of gecko foot-hair-inspired polymer nanofibers. *Adv. Funct. Mater.*, 17:2211–2218, 2007.

[69] A. G. Peressadko, N. Hosoda, and B. N. J. Persson. Influence of surface roughness on adhesion between elastic bodies. *Phys. Rev. Lett.*, 95:124301, 2005.

[70] E.-S. Yoon, R.A. Singh, H. Kong, B. Kim, D.-H. Kim, H.E. Jeong, and K.Y. Suh. Tribological properties of bio-mimetic nano-patterned polymeric surfaces on silicon wafer. *Tribol. Lett.*, 21:31–37, 2006.

[71] L. Qu, L. Dai, M. Stone, Z. Xia, and Z. L. Wang. Carbon nanotube arrays with strong shear binding-on and easy normal lifting-off. *Science*, 322:238–242, 2008.

[72] Y. Maeno and Y. Nakayama. Geckolike high shear strength by carbon nanotube fiber adhesives. *Appl. Phys. Lett.*, 94:012103, 2009.

[73] C. Majidi, R. E. Groff, Y. Maeno, B. Schubert, S. Baek, B. Bush, R. Maboudian, N. Gravish, M. Wilkinson, K. Autumn, and R. S. Fearing. High friction from a stiff polymer using microfiber arrays. *Phys. Rev. Lett.*, 97:076103, 2006.

[74] L. Ge, S. Sethi, L. Ci, P. M. Ajayan, and A. Dhinojwala. Carbon nanotube-based synthetic gecko tapes. *PNAS*, 104:10792–10795, 2007.

[75] J. Lee, R. S. Fearing, and K. Komvopoulos. Directional adhesion of gecko-inspired angled microfiber arrays. *Appl. Phys. Lett.*, 93:191910, 2008.

[76] J. Lee, C. Majidi, B. Schubert, and R. S. Fearing. Sliding-induced adhesion of stiff polymer microfibre arrays. I. Macroscale behaviour. *J. R. Soc. Interface*, 5:835–844, 2008.

[77] Y. Tian, N. Pesika, H. Zeng, K. Rosenberg, B. Zhao, P. McGuiggan, K. Autumn, and J. Israelachvili. Adhesion and friction in gecko toe attachment and detachment. *PNAS*, 103:19320–19325, 2006.

[78] H. Yao, G. Della Rocca, P. R. Guduru, and H. Gao. Adhesion and sliding response of a biologically inspired fibrillar surface: experimental observations. *J. R. Soc., Interface*, 5:723–733, 2008.

[79] H. Zeng, N. Pesika, Y. Tian, B. Zhao, Y. Chen, M. Tirrell, K. Autumn, K. L. Turner, and J. N. Israelachvili. Frictional adhesion of patterned surfaces and implications for gecko and biomimetic systems. *Langmuir*, 25:7486–7495, 2009.

[80] B. Zhao, N. Pesika, K. Rosenberg, Y. Tian, H. Zeng, P. McGuiggan, K. Autumn, and J. Israelachvili. Adhesion and friction force coupling of gecko setal arrays: implications for structured adhesive surfaces. *Langmuir*, 24:1517–1524, 2008.

[81] A. Ghatak, L. Mahadevan, J. Y. Chung, M. K. Chaudhury, and V. Shenoy. Peeling from a biomimetically patterned thin elastic film. *Proc. R. Soc. Lond. A*, 460:2725–2735, 2004.

[82] A. Majumder, A. Ghatak, and A. Sharma. Microfluidic adhesion induced by subsurface microstructures. *Science*, 318:258–261, 2007.

[83] B. Bhushan, A. G. Peressadko, and T. W. Kim. Adhesion analysis of two-level hierarchical morphology in natural attachment systems for 'smart adhesion'. *J. Exp. Biol.*, 20:1475–1491, 2006.

[84] T. W. Kim and B. Bhushan. Adhesion analysis of multi-level hierarchical attachment system contacting with a rough surface. *J. Adhes. Sci. Technol.*, 21:1–20, 2007.

[85] T. W. Kim and B. Bhushan. Optimization of biomimetic attachment system contacting with a rough surface. *J. Vac. Sci. Technol. A*, 25:1003–1012, 2007.

[86] K. Autumn, Y. A. Liang, and S. T. Hsieh et al. Adhesive force of a single gecko foot-hair. *Nature*, 405:681–685, 2000.

[87] M. Sitti and R. S. Fearing. Nanomolding based fabrication of synthetic gecko foot-hairs. *IEEE-NANO 2002, MP2: Nanotechnology: biological systems and applications*, pages 137–140, 2002.

[88] B. Bhushan. Adhesion of muti-level hierarchical attachment systems in gecko feet. *J. Adhes. Sci. Technol.*, 21:1213–1258, 2007.

[89] C. Greiner, E. Arzt, and A. del Campo. Hierarchical gecko-like adhesives. *Adv. Mater.*, 21:479–482, 2009.

[90] H. Yao and H. Gao. Mechanical principles of robust and releasable adhesion of gecko. *J. Adhes. Sci. Technol.*, 21:1185–1212, 2007.

[91] H. Yao and H. Gao. Mechanics of robust and releasable adhesion in biology: Bottom-up designed hierarchical structures of gecko. *J. Mech. Phys. Solids*, 54:1120–1146, 2006.

[92] H. Yao and H. Gao. Bio-inspired mechanics of bottom-up designed hierarchical materials: robust and releasable adhesion systems of gecko. *Bull. Pol. Ac.: Tech.*, 55:141–150, 2007.

[93] A. Y. Y. Ho, H. Gao, Y. C. Lam, and I. Rodríguez. Controlled fabrication of multitiered three-dimensional nanostructures in porous alumina. *Adv. Funct. Mater.*, 18:2057–2063, 2008.

[94] H. Zhang, L. W. Wu, S. X. Jia, D. J. Guo, and Z. D. Dai. Fabrication and adhesion of hierarchical micro-seta. *Chin. Sci. Bull.*, 57:1343–1349, 2012.

[95] A. Y. Y. Ho, L. P. Yeo, Y. C. Lam, and I. Rodríguez. Fabrication and analysis of gecko-inspired hierarchical polymer nanosetae. *ACS Nano*, 5:1897–1906, 2011.

[96] H. Lee and B. Bhushan. Fabrication and characterization of hierarchical nanostructured smart adhesion surfaces. *J. Colloid Interface Sci.*, 372:231–238, 2012.

[97] D. Y. Lee, D. H. Lee, S. G. Lee, and K. Cho. Hierarchical gecko-inspired nanohairs with a high aspect ratio induced by nanoyielding. *Soft Matter*, 8:4905, 2012.

[98] A. Saedi and M. Ghorbani. Electrodeposistion of Ni-Fe-Co alloy nanowirein modified AAO template. *Mater. Chem. Phys.*, 91:417–423, 2005.

[99] M. P. Murphy, S. Kim, and M. Sitti. Enhanced adhesion by gecko-inspired hierarchical fibrillar adhesives. *ACS Appl. Mater. Interfaces*, 1:849–855, 2009.

[100] Barsbüttel G. U. N. T. Gerätebau GmbH. Demonstration der Eulerschen Knickfälle. *Bestelltext WP 121*, 2010.

[101] D. Paretkar, M. Kampermann, A. S. Schneider, D. Martina, C. Creton, and E. Arzt. Bioinspired pressure actuated adhesive system. *Mater. Sci. Eng. C*, 31:1152–1159, 2011.

[102] M. A. Biot. Exact theory of buckling of a thick slab. *Appl. Sci. Res.*, 12:183–198, 1963.

[103] Y. Li, J. Zhang, T. Wang, S. Zhu, H. Yu, L. Fang, Z. Wang, L. Cui, and B. Yang. Full color plasmonic nanostructured surfaces and their sensor applications. *J. Phys. Chem. C*, 114:19908–19912, 2010.

[104] N. Vogel, S. Goerres, K. Landfester, and C. K. Weiss. A convenient method to produce close- and non-close-packed monolayers using direct assembly at the air-water interface and subsequent plasma-induced size reduction. *Macromol. Chem. Phys.*, 212:1719–1734, 2011.

[105] Y. J. Zhang, W. Li, and K. J. Chen. Application of two-dimensional polystyrene array in the fabrication of ordered silicon pillars. *J. Alloys Compd.*, 459:512–516, 2008.

[106] J. Rybczynski, U. Ebels, and M. Giersing. Large-scale, 2D arrays of magnetic nanoparticles. *Colloids Surf., A*, 219:1–6, 2003.

[107] C. F. Chau and T. Melvin. Design and fabrication of a quasi-ordered nanoporous silicon membrane suitable for thermally induced drug release. *J. Micromech. Microeng.*, 22:1–14, 2012.

[108] A. Plettl, F. Enderle, M. Saitner, A. Manzke, C. Pfahler, S. Wiedemann, and P. Ziemann. Non-close-packed crystals from self-assembled polystyrene spheres by isotropic plasma etching adding flexibility to colloid lithography. *Adv. Funct. Mater.*, 19:3279–3284, 2009.

[109] T. M. Blättler, A. Binkert, M. Zimmermann, M. Textor, J. Vörös, and E. Reimhult. From particle self-assembly to functionalized sub-micron protein patterns. *Nanotechnology*, 19:075301, 2008.

[110] N. D. Denkov, O. D. Velev, P. A. Kralchevsky, I. B. Ivanov, H. Yoshimura, and K. Nagayama. Mechanism of formation of two-dimensional crystals from latex particles on substrates. *Langmuir*, 8:3183–3190, 1992.

[111] Y. H. Pai, Y. C.Lin, J. L. Tsai, and G. R. Lin. Nonlinear dependence between the surface reflectance and the duty-cycle of semiconductor nanorod array. *Opt. Express*, 19:1680–1690, 2011.

[112] C. L. Cheung, R. J. Nikolić, C. E. Reinhardt, and T. F. Wang. Fabrication of nanopillars by nanosphere lithography. *Nanotechnology*, 17:1339–1343, 2006.

[113] C. F. Chau and T. Melvin. The fabrication of macroporous polysilicon by nanosphere lithography. *J. Micromech. Microeng.*, 18:1–9, 2008.

[114] M. E. Abdelsalam, P. N. Bartlett, J. J. Baumberg, and S. Coyle. Preparation of arrays of isolated spherical cavities by self-assembly of polystyrene spheres on self-assembled pre-patterned macroporous films. *Adv. Mater.*, 16:90–93, 2004.

[115] P. Born, S. Blum, A. Munoz, and T. Kraus. Role of the meniscus shape in large-area convective particle assembly. *Langmuir*, 27:8621–8633, 2011.

[116] C.-H. Sun, W.-L. Min, and P. Jiang. Templated fabrication of sub-100 nm periodic nanostructures. *Chem. Commun.*, 27:3163–3165, 2008.

[117] B. J. Y. Tan, C. H. Sow, T. S. Koh, K. C. Chin, A. T. S. Wee, and C. K. Ong. Fabrication of size-tunable gold nanoparticles array with nanosphere lithography, reactive ion etching, and thermal annealing. *J. Phys. Chem. B*, 109:11100–11109, 2005.

[118] A. Sinitskii, S. Neumeier, J. Nelles, M. Fischler, and U. Simon. Ordered arrays of silicon pillars with controlled height and aspect ratio. *Nanotechnology*, 18:305307, 2007.

[119] H. Asoh, A. Oide, and S. Ono. Formation of microstructured silicon surfaces by electrochemical etching using colloidal crystal as mask. *Electrochem. Commun.*, 8:1817–1820, 2006.

[120] C. W. Blackledge, J. M. Szarko, A. Dupont, G. H. Chan, E. L. Read, and S. R. Leone. Zinc oxide nanorod growth on gold islands prepared by microsphere lithography on silicon and quartz. *J. Adhes. Sci. Technol.*, 7:3336–3369, 2007.

[121] Z. Huang, H. Fang, and J. Zhu. Fabrication of silicon nanowire arrays with controlled diameter, length, and density. *Adv. Mater.*, 19:744–748, 2007.

[122] A. Manzke, N. Vogel, C. K. Weiss, U. Ziener, A. Plettl, K. Landfester, and P. Ziemann. Arrays of size and distance controlled platinum nanoparticles fabricated by a colloidal method. *Nanoscale*, 8:2523–2528, 2011.

[123] M. Karg, S. Jaber, T. Hellweg, and P. Mulvaney. Surface plasmon spectroscopy of gold-poly-n-isopropylacrylamide core-shell particles. *Langmuir*, 27:820–827, 2011.

[124] D. Brodoceanu, C. Fang, N. H. Voelcker, C. T. Bauer, A. Wonn, E. Kroner, E. Arzt, and T. Kraus. Fabrication of metal nanoparticle arrays by controlled decomposition of polymer particles. *Nanotechnology*, 24:1–7, 2013.

[125] H. J. Nam, D. Y. Jung, G. R. Yi, and H. Choi. Close-packed hemispherical microlens array from two-dimensional ordered polymeric microspheres. *Langmuir*, 22:7358–7363, 2006.

[126] H. K. Choi, S. H. Im, and O. O. Park. Fabrication of ordered nanostructured arrays using poly(dimethylsiloxane) replica molds based on three-dimensional colloidal crystals. *Adv. Funct. Mater.*, 19:1594–1600, 2009.

[127] H. K. Choi, S. H. Im, and O. O. Park. Shape and feature size control of colloidal crystal-based patterns using stretched polydimethylsiloxane replica molds. *Langmuir*, 25:12011–12014, 2009.

[128] X. H. Zhang, W. Que, and T. X. Gao. Monolayer polystyrene micro-spheres array master derived by spin-coating method for UV nanoimprint. *J. Nanosci. Nanotechnol.*, 12:6538–6542, 2012.

[129] S. Akerboom, J. Appel, David Labonte, W. Federle, J. Sprakel, and M. Kamperman. Enhanced adhesion of bioinspired nanopatterned elastomers via colloidal surface assembly. *J. R. Soc., Interface*, 12:20141061, 2014.

[130] E. Kroner and E. Arzt. Single macropillars as model systems for tilt angle dependent adhesion measurements. *Int. J. Adhes. Adhes.*, 36:32–38, 2012.

[131] M. Micciché, E. Arzt, and E. Kroner. Single macroscopic pillars as model system for bioinspired adhesives: influence of tip dimension, aspect ratio, and tilt angle. *ACS Appl. Mater. Interfaces*, 6:7076–7083, 2014.

[132] Elmar Kroner, Roya Maboudian, and Eduard Arzt. Adhesion characteristics of PDMS surfaces during repeated pull-off force measurements. *Adv. Eng. Mater.*, 12 (5):398–404, 2010.

[133] E. Kroner, D. R. Paretkar, R. M. McMeeking, and E. Arzt. Adhesion of flat and structured PDMS samples to spherical and flat probes: a comparative study. *J. Adhesion*, 87:447–465, 2011.

[134] H. Beermann. *INM Leibniz-Institute for New Materials, metal workshop*, 2014.

[135] P. Fratzl and F. G. Barth. Biomaterial systems for mechanosensing and actuation. *Nature*, 462:442–448, 2009.

[136] H. Gao and H. Yao. Shape insensitive optimal adhesion of nanoscale fibrilar structures. *PNAS*, 101:7851–7856, 2004.

[137] S. N. Gorb, M. Sinha, A. Peressadko, K. A. Daltorio, and R. D. Quinn. Insects did it first: a micropatterned adhesive tape for robotic applications. *Bioinspiration Biomimetics*, 2:117–125, 2007.

[138] M. Varenberg, N. M. Pugno, and S. N. Gorb. Spatulate structures in biological fibrillar adhesion. *Soft Matter*, 6:3269–3272, 2010.

[139] J. Berengueres, S. Saito, and K. Tadakuma. Structural properties of a scaled gecko foot-hair. *Bioinspiration Biomimetics*, 2:1–8, 2007.

[140] H. Gao, X. Wang, H. Yao, S. Gorb, and E. Arzt. Mechanics of hierarchical adhesion structures of geckos. *Mech. Mater.*, 37:275–285, 2005.

[141] H. E. Jeong and K. Y. Suh. Nanohairs and nanotubes: Efficient structural elements for gecko-inspired artificial dry adhesives. *Nano Today*, 4:335–346, 2009.

[142] D. J. Irschick, A. Herrel, and B. Vanhooydonck. Whole-organism studies of adhesion in pad-bearing lizards: creative evolutionary solutions to functional problems. *J. Comp. Physiol.*, 192:1169–1177, 2006.

[143] N. P. Pugno. Spiderman gloves. *Nano Today*, 3:35–41, 2008.

[144] A. P. Russell and M. K. Johnson. Real-world challenges to, and capabilities of, the gekkotan adhesive system: contrasting the rough and the smooth. *Can. J. Zool.*, 85:1228–1238, 2007.

[145] S. Gorb, M. Varenberg, A. Peressadko, and J. Tuma. Biomimetic mushroom-shaped fibrillar adhesive microstructure. *J. R. Soc. Interface*, 4:271–275, 2007.

[146] M. Kampermann, E. Kroner, A. del Campo, R. M. McMeeking, and E. Arzt. Functional adhesive surfaces with 'gecko' effect: the concept of contact splitting. *Adv. Eng. Mater.*, 12:335–348, 2010.

[147] M. P. Murphy, B. Aksak, and M. Sitti. Gecko-inspired directional and controllable adhesion. *Small*, 5:170–175, 2009.

[148] D. Paretkar, A. S. Schneider, E. Kroner, and E. Arzt. In situ observation of contact mechanisms in bioinspired adhesives at high magnification. *MRS Commun.*, 1:1–4, 2011.

[149] D. Sameoto and C. Menon. Recent advantages in the fabrication and adhesion testing of biomimetic dry adhesives. *Smart Mater. Struct.*, 19:1–18, 2010.

[150] H. E. Jeong, S. H. Lee, P. Kim, and K. Y. Suh. Stretched polymer nanohairs by nanodrawing. *Nano Lett.*, 6:1508–1513, 2006.

[151] S. Y. Liu, P. Zhang, H. Lü, C. W. Zhang, and Q. Xia. Fabrication of high aspect ratio microfiber arrays that mimic gecko foot hairs. *Chin. Sci. Bull.*, 57:404–408, 2012.

[152] M. T. Northen, C. Greiner, E. Arzt, and K. L. Turner. A gecko-inspired reversible adhesive. *Adv. Mater.*, 20:3905–3909, 2008.

[153] J. Yu, S. Chary, S. Das, J. Tamelier, N. S. Pesika, K. L. Turner, and J. N. Israelachvili. Gecko-inspired dry adhesive for robotic applications. *Adv. Funct. Mater.*, 21:3010–3018, 2011.

[154] J. Yu, S. Chary, S. Das, J. Tamelier, K. L. Turner, and J. N. Israelachvili. Friction and adhesion of gecko-inspired PDMS flaps on rough surfaces. *Langmuir*, 28:11527–11534, 2012.

[155] S. Das, N. Cadirov, S. Chary, Y. Kaufman, J. Hogan, K. L. Turner, and J. N. Israelachvili. Stick-slip friction of gecko-mimetic flaps on smooth and rough surfaces. *J. R. Soc., Interface*, 104:20141346, 2015.

[156] A. Asbeck, S. Dastoor, A. Parness, L. Fullerton, N. Esparza, D. Soto, B. Heyneman, and M. Cutkosky. Climbing rough vertical surfaces with hierarchical directional adhesion. *IEEE International Conference on Robotics and Automation*, pages 2675–2680, 2009.

[157] J. Lee, B. Bush, R. Maboudian, and R. S. Fearing. Gecko-inspired combined lamellar and nanofibrillar array for adhesion on nonplanar surface. *Langmuir*, 25:12449–12453, 2009.

[158] B. Aksak, M. P. Murphy, and M. Sitti. Gecko inspired micro-fibrillar adhesives for wall climbing robots on micro/nanoscale rough surfaces. *IEEE International Conference on Robotics and Automation*, May 19-23:3058–3063, 2008.

[159] D. Ruffatto, D. Beganovic, A. Parness, and M. Spenko. Experimental evaluation of adhesive technologies for robotic grippers on micro-rough surfaces. *IEEE International Conference on Robotics and Automation*, May 31–June 7:6150–6155, 2014.

[160] D. Ruffatto, D. Beganovic, A. Parness, and M. Spenko. Experimental results of a controllable electrostatic/gecko-like adhesive on space materials. *Aerospace Conference, IEEE International Conference on Robotics and Automation*, March 1–8:1–7, 2014.

[161] Y. Li, D. Sameoto, and C. Menon. Enhanced compliant adhesive design and fabrication with dual-level hierarchical structure. *Journal of Bionic Engineering*, 7:228–234, 2010.

[162] J. Krahn, D. Sameoto, and C. Menon. Controllable biomimetic adhesion using embedded phase change material. *Smart Mater. Struct.*, 20:1–8, 2011.

[163] A. G. Gillies, A. Henry, H. Lin, A. Ren, K. Shiuan, R. S. Fearing, and R. J. Full. Gecko toe and lamellar shear adhesion on macroscopic, engineered rough surfaces. *The Journal of Experimental Biology*, 217:283–289, 2014.

[164] A. G. Gillies and R. S. Fearing. Simulation of synthetic gecko arrays shearing on rough surfaces. *J. R. Soc., Interface*, 11:20140021, 2014.

[165] R. A. Sauer. A three-dimensional multiscale finite element model describing the adhesion of a gecko seta. *Proc. Appl. Math. Mech.*, 9:157–158, 2009.

[166] Elmar Kroner and Eduard Arzt. Mechanistic analysis of force-displacement measurements on macroscopic single adhesive pillars. *J. Mech. Phys. Solids*, 61:1295–1304, 2013.

[167] Nishant Lakhera, Annalena Graucob, Andreas S. Schneider, Elmar Kroner, Eduard Arzt, and Christopher M. Yakacki Carl P. Frick. Effect of viscoelasticity on the spherical and flat adhesion characteristics of photopolymerizable acrylate polymer networks. *Int. J. Adhes. Adhes.*, 44:184–194, 2013.

[168] Nishant Lakhera, Annalena Graucob, Andreas S. Schneider, Elmar Kroner, Maurizio Miccichéa, Eduard Arzt, and Carl P. Frick. Adhesion behavior of polymer networks with

tailored mechanical properties using sperical and flat contacts. *MRS Commun.*, 3:73–77, 2013.

[169] L. Harpe, G. Carbone, E. Pierro, A. E. Kovalev, and S. N. Gorb. Adhesion tilt-tolerance in bio-inspired mushroom-shaped adhesive microstructure. *Appl. Phys. Lett.*, 104:011906 1–5, 2014.

[170] B. Aksak, K. Sahin, and M. Sitti. The optimal shape of elastomer mushroom-like fibers for high and robust adhesion. *Beilstein J. Nanotechnology*, 5:630–638, 2014.

[171] Dadhichi Paretkar, Marleen Kamperman, David Martina, Jiahua Zhao, Costantino Creton, Anke Lindner, Anand Jagota, Robert McMeeking, and Eduard Arzt. Preload-responsive adhesion: effects of aspect ratio, tip shape and alignment. *J. R. Soc., Interface*, 10:73–77, 2013.

[172] A. del Campo and E. Arzt. *Generating micro- and nanopatterns on polymeric materials.* Wiley, Weinheim, 2011.

[173] A. del Campo and E. Arzt. Design parameters and current fabrication approaches for developing bioinspired dry adhesives. *Macromol. Biosci.*, 7:118–127, 2007.

[174] S. Kim and M. Sitti. Biological inspired polymer microfibers with spatulate tips as repeatable fibrillar adhesives. *Appl. Phys. Lett.*, 89:261911, 2006.

[175] J. W. Lussi, C. Tang, P. A. Kuenzi, U. Staufer G. Csucs, J. Vörös, G. Danuser, J. A. Hubbell, and M. Textor. Selective molecular assembly patterning at the nanoscale: a novel platform for producing protein patterns by electron-beam lithography on SiO_2/indium tin oxide-coated glass substrates. *Nanotechnology*, 16:1781–1786, 2005.

[176] P. A. Künzi, J. Lussi, L. Aeschimann, G. Danuser, M. Textor, N. F. de Rooij, and U. Staufer. Nanofabrication of protein-patterned substrates for future cell adhesion experiments. *Microelectron. Eng.*, 78-79:582–586, 2005.

[177] J. C. Wolfe, S. V. Pendharkar, P. Ruchhoeft, S. sen, M. D. Morgan, W. E. Horne, R. C. Tiberio, and J. N. Randall. A proximity ion beam lithography process for high density nanostructures. *J. Vac. Sci. Technol. B*, 14:3896–3899, 1996.

[178] F. Rousseaux, D. Decanini, F. Carcenac, E. Cambril, M. F. Ravet, C. Chappert, N. Bardou, B. Bartenlian, and P. Veillet. Study of large area high density magnetic dot arrays fabricated using synchrotron radiation based x-ray lithography. *J. Vac. Sci. Technol. B*, 13:2787–2791, 1995.

[179] T. A. Savas, M. L. Schattenburg, J. M. Carter, and H. I. Smith. Large-area achromatic interferometric lithography for 100 nm period gratings and grids. *J. Vac. Sci. Technol. B*, 14:4167–4170, 1996.

[180] J. P. Spallas, R. D. Boyd, J. A. Britten, A. Fernandez, A. M. Hawryluk, M. D. Perry, and D. R. Kania. Fabrication of sub-0.5 μm diameter cobalt dots on silicon substrates and photoresist pedestals on 50 cm x 50 cm glass substrates using laser interference lithography. *J. Vac. Sci. Technol. B*, 14:2005–2007, 1996.

[181] W. Chen, R. H. W. Lam, and J. Fu. Photolithographic surface micromachining of polydimethylsiloxane (PDMS). *Lab Chip*, 12:391–395, 2012.

[182] C. L. Tuinea-Bobe, P. Lemoine, M. U. Manzoor, M. Tweedie, R. A. D'Sa, C. Gehin, and E. Wallace. Photolithographic structuring of stretchable conductors and sub-kPa pressure sensors. *J. Micromech. Microeng.*, 21:1–12, 2011.

[183] L. Bogunovic, D. Anselmetti, and J. Regtmeier. Photolithographic fabrication of arbitrarily shaped SU-8 microparticles without sacrificial release layers. *J. Micromech. Microeng.*, 21:1–5, 2011.

[184] Y. Xia and G. M. Whitesides. Soft lithography. *Annu. Rev. Mater. Sci.*, 28:153–184, 1998.

[185] Y. Xia, J. Tien, D. Qin, and G. M. Whitesides. Non-photolithographic methods for fabrication of elastomeric stamps for use in microcontact printing. *Langmuir*, 12:4033–4038, 1996.

[186] J. G. Kim, N. Tamaka, B. J. Kim, and H. Fujita. Optical-softlithographic technology for patterning on curved surfaces. *J. Micromech. Microeng.*, 19:1–8, 2009.

[187] H. J. Nam, J. H. Kim, D. Y. Jung, J. B. Park, and H. S. Lee. Two-dimensional nanopatterning by PDMS relief structures of polymeric colloidal crystals. *Appl. Surf. Sci.*, 254:5134–5140, 2008.

[188] C. Brombacher, M. Saitner, C. Pfahler, A. Plettl, P. Ziemann, D. Makarov, D. Assmann, M. H. Siekman, L. Abelmann, and M. Albrecht. Tailoring particle arrays by isotropic plasma etching: an approch towards percolated perpendicular media. *Nanotechnology*, 20:105304, 2009.

[189] C. Cong, W. C. Junus, Z. Shen, and T. Yu. New colloid lithographic nanopatterns fabricated by combining pre-heating and reactive ion etching. *Nanoscale Res. Lett.*, 4:1324–1328, 2009.

[190] C. Haginoya, M. Ishibashi, and K. Koike. Nanostructure array fabrication with a size-controllable natural lithography. *Appl. Phys. Lett.*, 20:2934–2936, 1997.

[191] L. Yan, K. Wang, J. Wu, and L. Ye. Hydrophobicity of model surfaces with loosely packed polystyrene spheres after plasma etching. *J. Phys. Chem. B*, 110:11241–11246, 2006.

[192] M. Ledvij. Curve fitting made easy. *The Industrial Physicist*, April/May:24–27, 2003.

[193] René Hensel. *Robust omniphobic surfaces by mimicking the springtail skin morphology.* PhD thesis, Leibniz-Institut für Polymerforschung Dresden e.V. und Max-Bergmann-Zentrum für Biomaterialien Dresden, 2014.

[194] René Hensel, Christoph Neinhuis, and Carsten Werner. The springtail cuticle as a blueprint for omniphobic surfaces. *Chem. Soc. Rev.*, 2015.

[195] Prof. Ingo Rechenberg. Nanobionik: Lotus-, Sandfisch- und Mottenaugen-Effekt. *PowerPoint-Folien zur 9. Vorlesung 'Bionik I', TU Berlin*, Online, 3 2015.